

**Impact of scale-aware deep convection on the cloud liquid and ice water paths and precipitation using the Model for Prediction Across Scales (MPAS-v5.2)**

Laura D. Fowler, Mary C. Barth, and Kiran Alapaty

**Replies to Referee 1**

Before replying to Referee 1, the authors wish to thank Referee 1 to read and provide a thorough review of our manuscript, including constructive critics and suggestions.

1. Replace “scale-aware” with “scale-adaptive”: We understand that the Referee would want to replace “scale-aware” with “scale-adaptive”. A few scientists have also argued “scale-insensitive” would be a better term as well. However, a lot of the publications related to GF and MSKF use the term “scale-aware” to describe how parameterizations of deep convection handles transitions between hydrostatic and nonhydrostatic. The authors would rather keep the “scale-aware” term in their manuscript.
2. Point out that for GF, the term  $(1-\sigma)^2$  factor is very small for grid-spacings  $< 6$  km while at 4-6 km we do not expect convection to be resolved: In order to reply to Referees 1 and 2, we rewrote the paragraph that discusses Fig.1. See lines 194-206.
3. Drop Figure 9: We removed Fig.9 showing the monthly-mean grid-scale (THOM) precipitation rate, as suggested by the Referee. We also revised the writing of Section 4, including that related to Tables 2 and 3.
4. In Figure 12, plot instead the difference in RH with the ERA5 reanalyses and rewrite discussion lines 582-598: As suggested by Referee 1, we plotted RH difference against ERA and ERA5 reanalyses (see Figs. 12-ERA and 12-ERA5 below).
  - First, the first author is reluctant to use ERA5 instead of ERA-Interim reanalyses since initialization of the four simulations was done using ERA-Interim data. Readers may wonder why the authors used ERA-Interim to initialize MPAS while they used ERA5 to analyze results. Figs. 12-ERA and 12-ERA5 show that the four simulations display biases of the same magnitude when compared against the “observed” relative humidity.
  - Second, the first author is reluctant to replace Fig 12 (updated to Fig. 11 since we removed Fig. 9) because RH depends on calculating saturation mixing ratios which are different in MPAS and ERA, particularly for the ice phase. This would imply further analyses on differences between simulated and ERA temperature longitude-pressure crosssections which is beyond the scope of this research.
5. Page 25, discussion of the upward moisture flux: In calculating of the upward moisture flux, convective drying/moistening is included in  $q_v$ . As discussed in Section 3.1 (starting lin 290), diabatic tendencies are added to the state moist variables in conjunction with horizontal and vertical advection during each Runge-Kutta timestep. Therefore, all state moist variables include the contribution from deep/shallow convection when grid-scale cloud microphysics is applied. The effect of water vapor and condensates are also included in the vertical momentum equation.
6. Page 27, lines 640ff rewrite and shorten: Done.
7. Figure 14: plot instead differences against you retrieved LWP: Done. The paragraph about Fig. 14 (now Fig. 13) has been rewritten accordingly.
8. Drop Figure 15: Done. The paragraph about Fig. 15 has been corrected accordingly.

9. Put more emphasis on Figure 16: The first author believes that she calculated correctly the precipitable water correctly by using the ERA specific humidity interpolated to fixed pressure levels, multiplied by the pressure thickness and divided by  $g$ . The pressure thickness was computed using the half-pressure levels above and below the fixed pressure levels. Specific humidities were first converted to water vapor mixing ratios. For the same reasons as in 4. above, the authors would prefer to use ERA-Interim instead of ERA5 monthly-mean reanalyses. The paragraph describing Fig. 16 (now Fig. 14) has been rewritten.
10. Is the overestimation of LWP in GF an error in the amount of condensate or only the phase (i.e. it doesn't glaciate correctly?): As I wrote in the manuscript, part of the overestimation in GF may be because of the shallow convection scheme. Additional short-term experiments could also be run varying the partitioning between detrained cloud liquid and water and ice. This could also be handled by improving the microphysics in the GF cloud model itself.
11. As for Fig. 14 (now Fig. 13), plotted differences between the simulated and SSF IWP (new Fig. 15) for consistency with the LWP.
12. Lines 699-702: you say that the partitioning between liquid and ice might be responsible, yes, but you can check this, also it could be the different mass flux profile, i.e. upper level condensate detrainment: See response in 10) above.
13. Lines 730-733: "the strong upscaling effect of the refined grid mesh": I tried to shortly address this issue in Section 4.2, following suggestions made by Referee 2. Further research is needed to understand the response of GF over the transition zone between the refined and coarse areas of the mesh.
14. Lines 738-740: Please note again the MSKF might give the right answer in LWP for wrong reason (too dry) and you need to check out why GF overestimates, at least apparently overestimates LWP. Noted. Thank you.

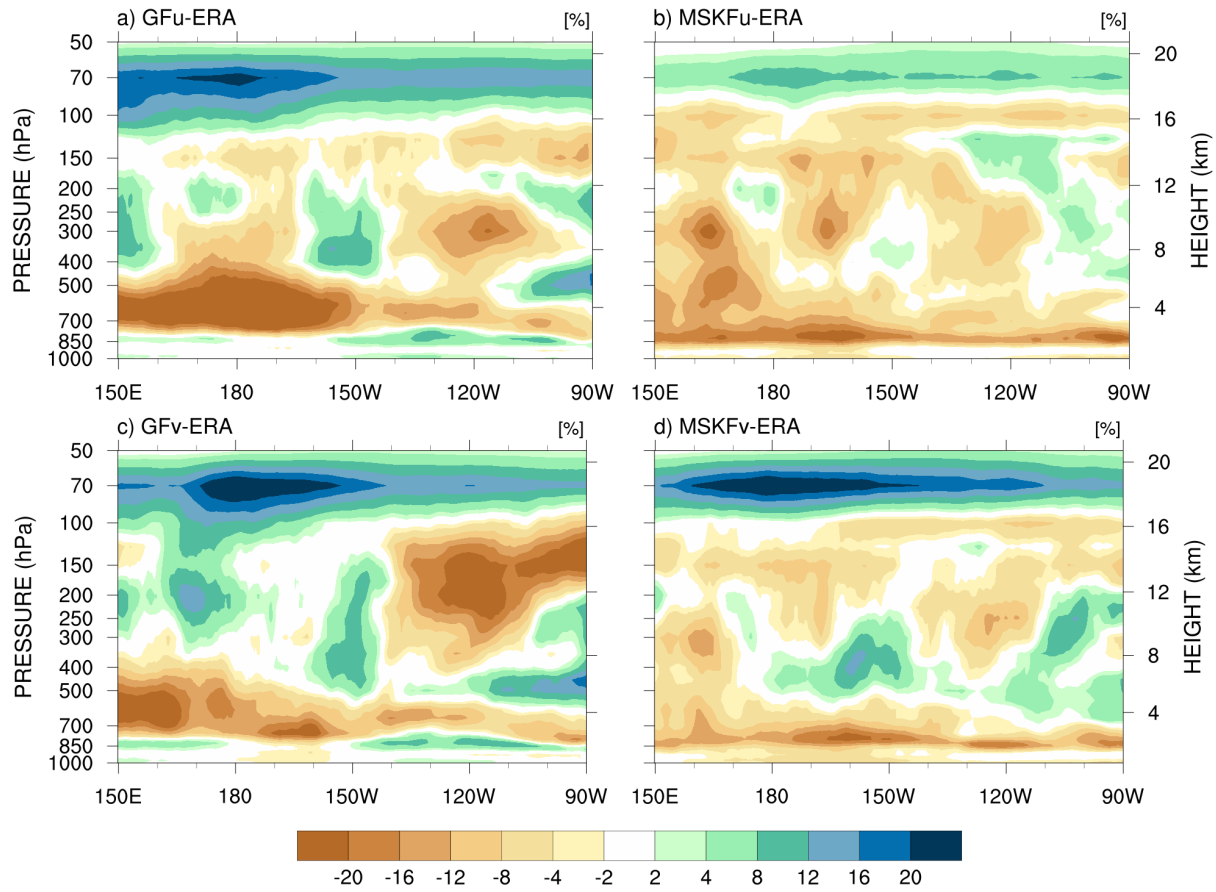


Figure 12-ERA: Longitude versus pressure cross-sections of latitudinally-averaged (between 5°S and 5°N) monthly-mean relative humidity (RH) difference across the Tropical Pacific Ocean for December 2015: a) GFu minus ERA-Interim RH; b) MSKFu minus ERA-Interim RH; c) GFv minus ERA-Interim RH; and d) MSKFv minus ERA-Interim RH.

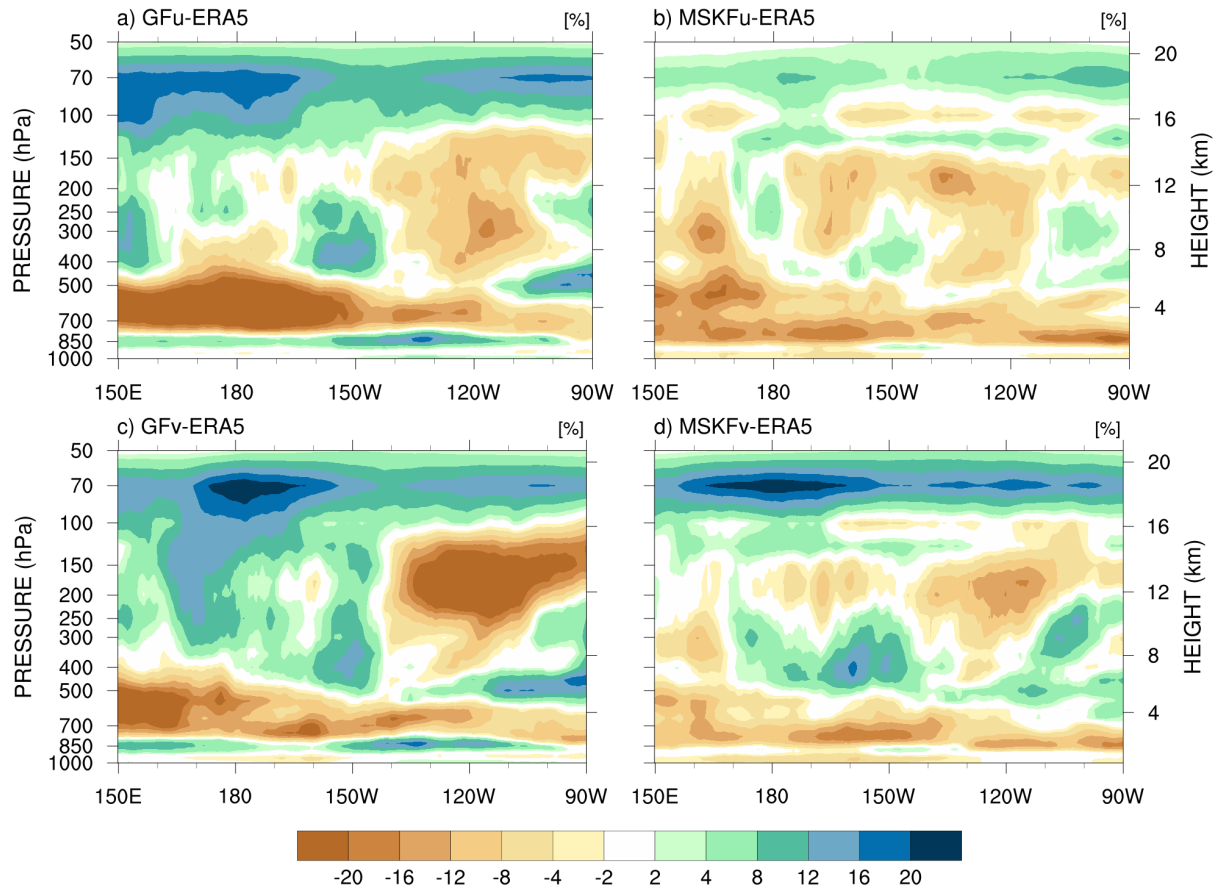


Figure 12-ERA5: Longitude versus pressure cross-sections of latitudinally-averaged (between 5°S and 5°N) monthly-mean relative humidity (RH) difference across the Tropical Pacific Ocean for December 2015: a) GFu minus ERA5 RH; b) MSKFu minus ERA5 RH; c) GFv minus ERA5 RH; and d) MSKFv minus ERA5 RH.

## Replies to Referee 2

Before replying to Referee 2, the authors wish to thank Referee 2 to read and provide a thorough review of our manuscript, including constructive critics and suggestions.

Major concerns:

1) Applicability of 30-day runs for evaluating “average” model state, systematic biases.

In response to the concern that “30 days is a duration that does not fit neatly into one of these bins”, and as suggested by the reviewer, we compare the 10-day mean calculated between 00 UTC 1 Dec. and 00 UTC 11 Dec. 2015 against the full monthly mean for most of the diagnostics discussed in our manuscript. The file “RepliesReferee2.AdditionalFigs.pdf” includes most of the same figures as those shown in our manuscript and displays 10-day mean instead of monthly-mean diagnostics. The figure captions are the same as those in our manuscript, except for adding an “r” after the figure number. In contrast to Fig. 5, the left panels of Fig. 5r show the 10-day mean LWP, IWP, and CLD instead of monthly-mean SSF1deg data.

Comparing the figures from “RepliesReferee2.AdditionalFigs.pdf” compared to their respective figures from our manuscript highlights that GFu, GFv, MSKFu, andMSKFv, display similar errors in days 1-10 when compared to their full monthly means. In particular:

- Figure 11r displays similar biases in the total precipitation rate produced with GFu, GFv, MSKFu, and MSKFv when compared to TMPA data, including the bias in the location of the ITCZ over the Tropical Pacific Ocean, as pointed out by Referee 2.
- Figures 14r and 17r display similar biases in the LWP and IWP produced with the four simulations when compared against the 10-day mean SSF data, leading to similar biases in the TOACLD, TOALW, and TOASW over the Tropical Pacific Ocean.
- Finally, the different figures “from RepliesReferee2.AdditionalFigs.pdf” display patterns in the 10-day mean diagnostics as in the monthly-mean diagnostics over the transition zone between the coarse and refined area of the mesh, as seen in the various GFv-GFu and MSKFv-MSKFu panels.

The authors hope that adding this set of figures will help Referee 2 conclude that the discussed biases are mostly independent of how the averaged model state was computed. The fact that 10-mean diagnostics show similar biases as monthly-mean diagnostics will help further understand the strong upscaling effect of the refined grid mesh on the coarse grid mesh, as proposed in Section 6.

2) Potential sensitivity of moist results to A) physics timestep and B) numerical diffusion.

- A) Physics timestep: In MPAS, the physics timestep used in the Noah land surface scheme, the MYNN Planetary boundary layer and surface layer schemes, the Hong et al. gravity wave-drag scheme, and the deep and shallow convection schemes is the same as the dynamical timestep, i.e. 150s for the U runs and 30s for the V runs. For these physics schemes, we confirm the timestep reduction between the U and V runs is for “both” the dynamics and physics. The RRTMG longwave and shortwave radiation schemes are run every 15mns for the U and V runs. The recommended maximum timestep is 90s for the Thompson cloud microphysics scheme. Whereas the cloud microphysics timestep is the same as the dynamic timestep for the V runs, the microphysics timestep is set to 75s in the U runs w, and cloud microphysics is sub-cycled twice in the U runs.
- B) Numerical diffusion: In MPAS, numerical diffusion follows the horizontal filtering formulation of Smagorinsky (1963), as described in Skamarock et al. (Eq. 17; 2012). In Eq. 17,  $l$  is the horizontal length scale which is defined as the minimum distance between cell centers, and weighted as a function the mesh density, and therefore as a function of the mesh resolution. In Table 1, while  $l$  is equal to 30 km for the uniform-resolution experiments GFu and MSKFu since the mesh density is

equal to 1, the minimum  $l$  value is set to 6 km in GFv and MSKFv, and weighted by a scaling factor which depends in the spatially-varying mesh density. Therefore, numerical diffusion takes into account the grid mesh resolution.

3) Time step:

As suggested, we ran a 10-day experiment using the GFu configuration, but with a 30s time step as in GFv (see Fig. 2S). We did see increased in convective precipitation between the 2 configurations in GFu which we attempted to address this point in Section 4.2. We agree that this result needs to be analyzed in more details. On the top of a better understanding on the partitioning between the LWP and IWP over the refined area of the mesh, this is another item that we are currently working on in greater details by looking at the contribution of the different closures to the observed increase in the convective parameterization.

Minor comments:

15. Line 148: Corrected typo.

Lines 175-176: The reason behind choosing one closure for the shallow convection scheme is the following: While first testing the implementation of the GF deep and shallow convection schemes, Dr. Grell suggested to test a few other closures for the shallow scheme. While the default option for the GF deep convection scheme is to use an ensemble of closures whereas the default option for the GF shallow convection scheme is to use the single *BLQE* closure, first proposed by Dr. Freitas. In the end, we choose to use the default options for the GF deep and shallow scheme, as first proposed and tested by Grell and Freitas (2014). We hope that this explanation will satisfy Referee 2.

Line 194: As suggested, we added an extra sentence related to the 0.7 threshold in  $\sigma$ . This sentence is similar to that in Fowler et al. (2016). As the use of this threshold was described in Fowler et al. (2016), the first author thought that a more detailed explanation was not required. Thank you.

Lines 201-211: Rephrased. The first author meant to say that the minimum thickness of the mixed layer is set to 50 hPa, meaning that for mixed layers to be identified as initial potential source layers for convection, they must be at least 50 hPa thick.

Line 316: Rephrased. In that sentence, the first author was trying to distinguish between the complexity of condensation and precipitation processes in cloud microphysics parameterizations such as WSM6 and THOM, and the simple conversion from condensed water to precipitation in simpler cloud models used in parameterizations of convection.

Line 412: In Fig. 5, the authors were trying to understand the difference in the IWP computed from the SSF data (Fig. 5.c) versus that provided in the SSF1deg data (Fig. 5.d). As stated lines 406-407, our method to compute the IWP is much simpler than that used by the CERES Science Team, and we do not have details on how the Science Team computed the IWP provided in the SSF1deg data.

Lines 513-515:

Line 532: Replaced “evaluated” with “compared”.

Lines 537-538: Replaced Figs 10.b,e and Figs. 11a,d with Figs. 10.b-e and Figs. 11.a-d.

Fig. 12: Done.

Lines 622-624: Not being an expert on satellite retrievals, it is difficult for the first author to define a “true” way for satellites to best observe the liquid and and rain water paths, separately. Section 1 summarizes the large discrepancies in the LWP and IWP between satellite-derived data sets and highlights differences in the LWP (IWP) derived from passive and active sensors. It is my understanding that in satellite retrievals, separating suspended from precipitating condensates is based on using threshold methods, but that methods vary between satellite retrievals. It remains very difficult to compare satellite-retrieved versus simulated

condensates. Another approach would be for MPAS to calculate radiances or radar reflectivities measured by satellites using cloud simulators, as sometimes done with climate models.

GLOBAL INCIDENCE OF SHALLOW CONVECTION (%)

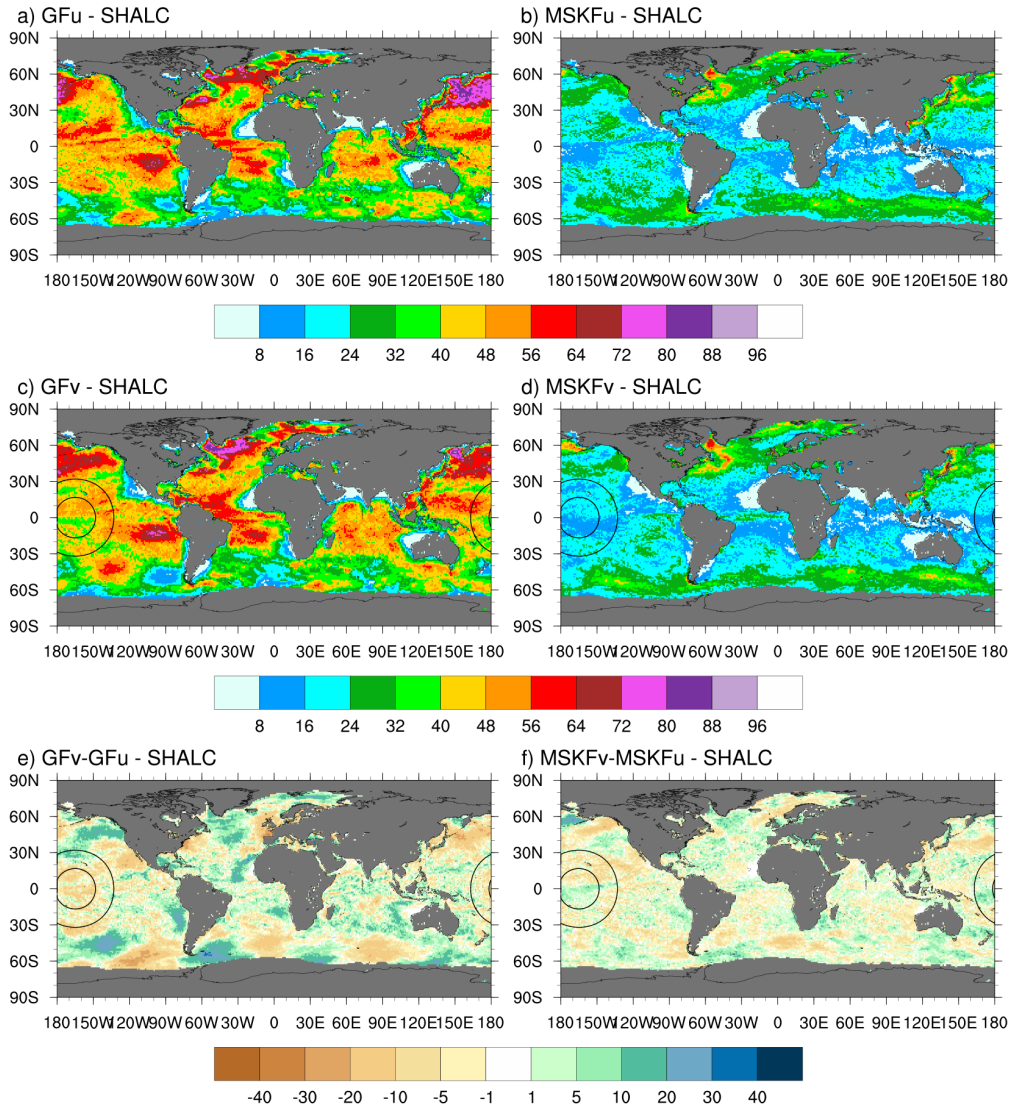


Figure 6: Global monthly-mean incidence of shallow convection (SHALC) simulated in GFu and MSKFu (top panels), and GFv and MSKFv (middle panels), and difference in the incidence of shallow convection between GFv and GFu (bottom left panel) and MSKFv and MSKFu (bottom right panel) for December 2015.



GLOBAL INCIDENCE OF DEEP CONVECTION (%)

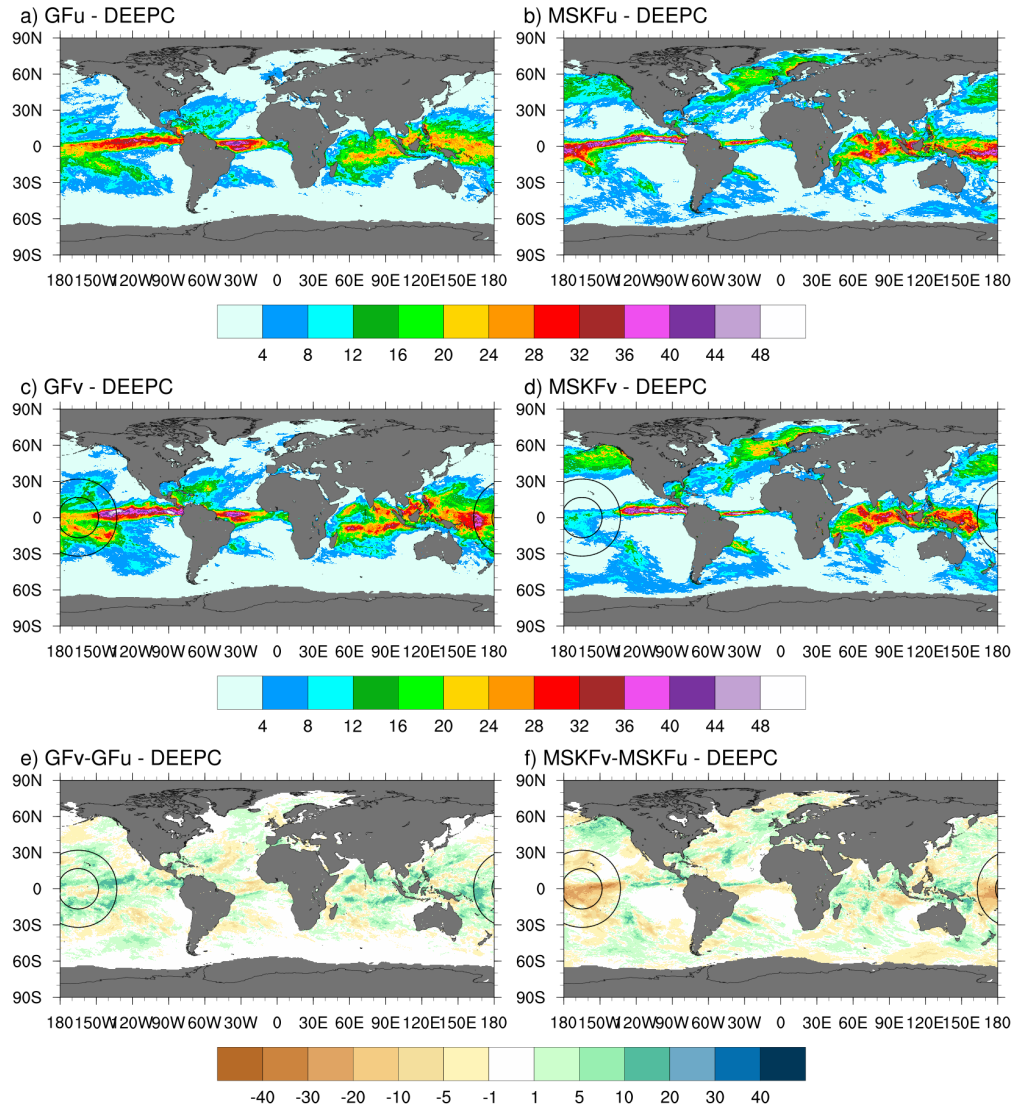


Figure 7: As Fig. 6, but for the global monthly-mean incidence of deep convection (DEEPC).

GLOBAL PRECIPITATION RATE DIFFERENCE (mm day<sup>-1</sup>)

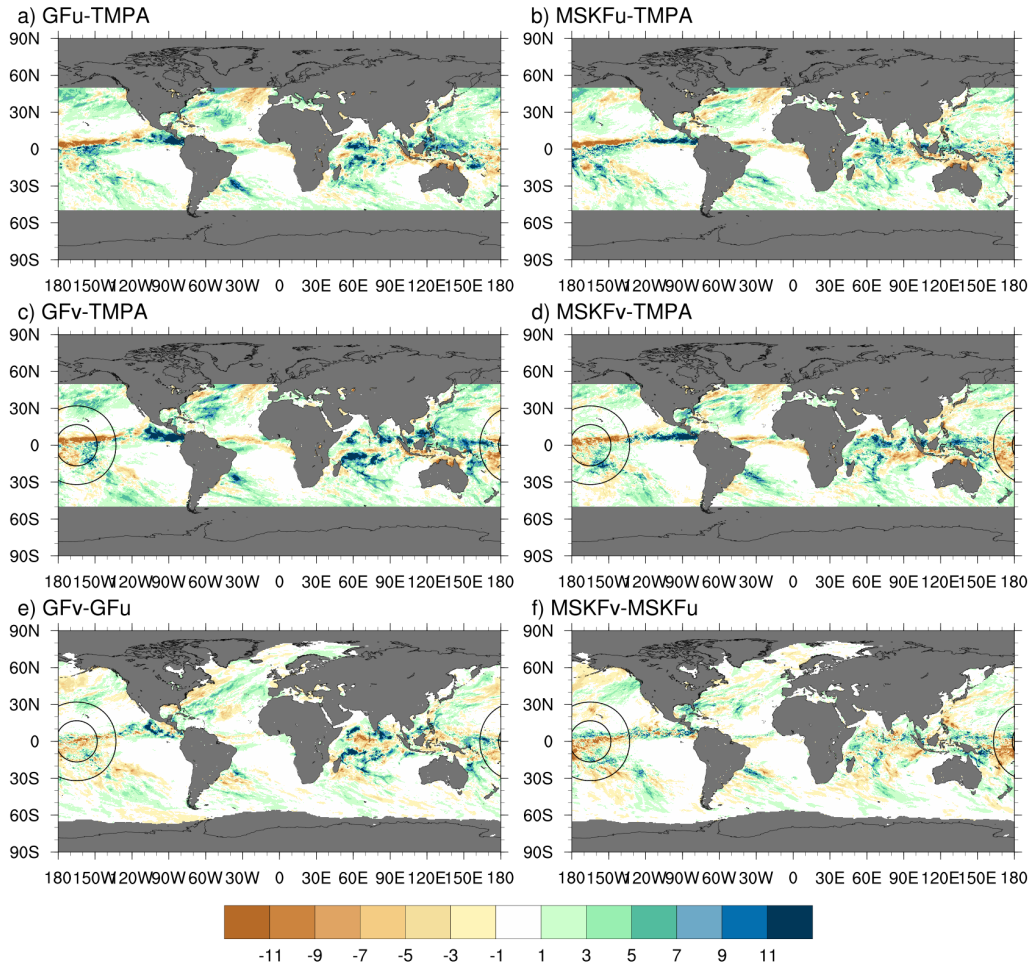


Figure 11: Global monthly-mean precipitation rate difference between GFu (MSKFu) and TMPA data (top panels), GFv (MSKFv) and TMPA data (middle panels), and between GFv (MSKFv) and GFu (MSKFu) (bottom panels) for December 2015.

GLOBAL CLOUD LIQUID WATER PATH ( $\text{g m}^{-2}$ )

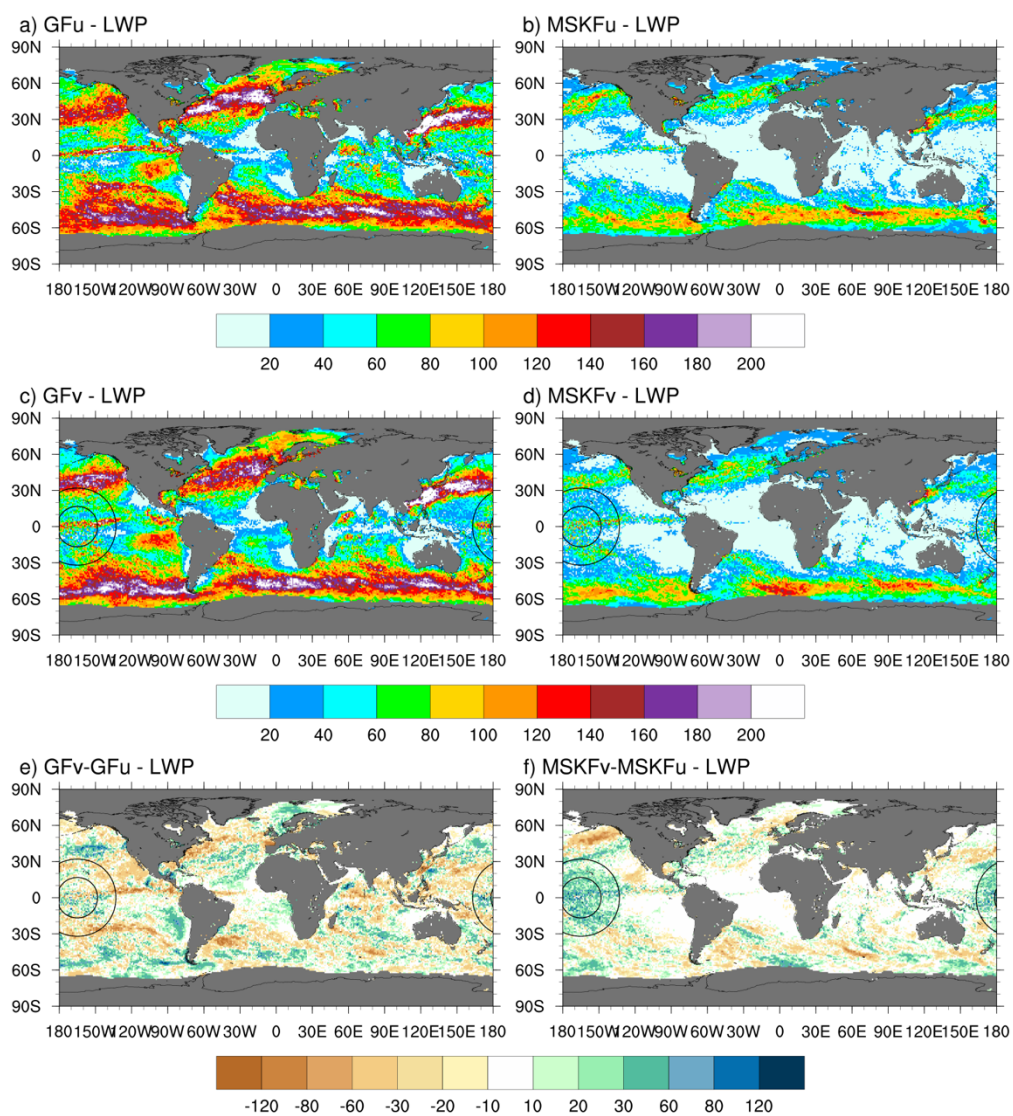


Figure 14: Global monthly-mean cloud liquid water path (LWP) simulated with GFu and MSKFu (top panels) and GFv and MSKFv (middle panels), and global monthly-mean LWP difference between GFv and GFu, and MSKFv and MSKFu (bottom panels) for December 2015.

GLOBAL CLOUD ICE WATER PATH ( $\text{g m}^{-2}$ )

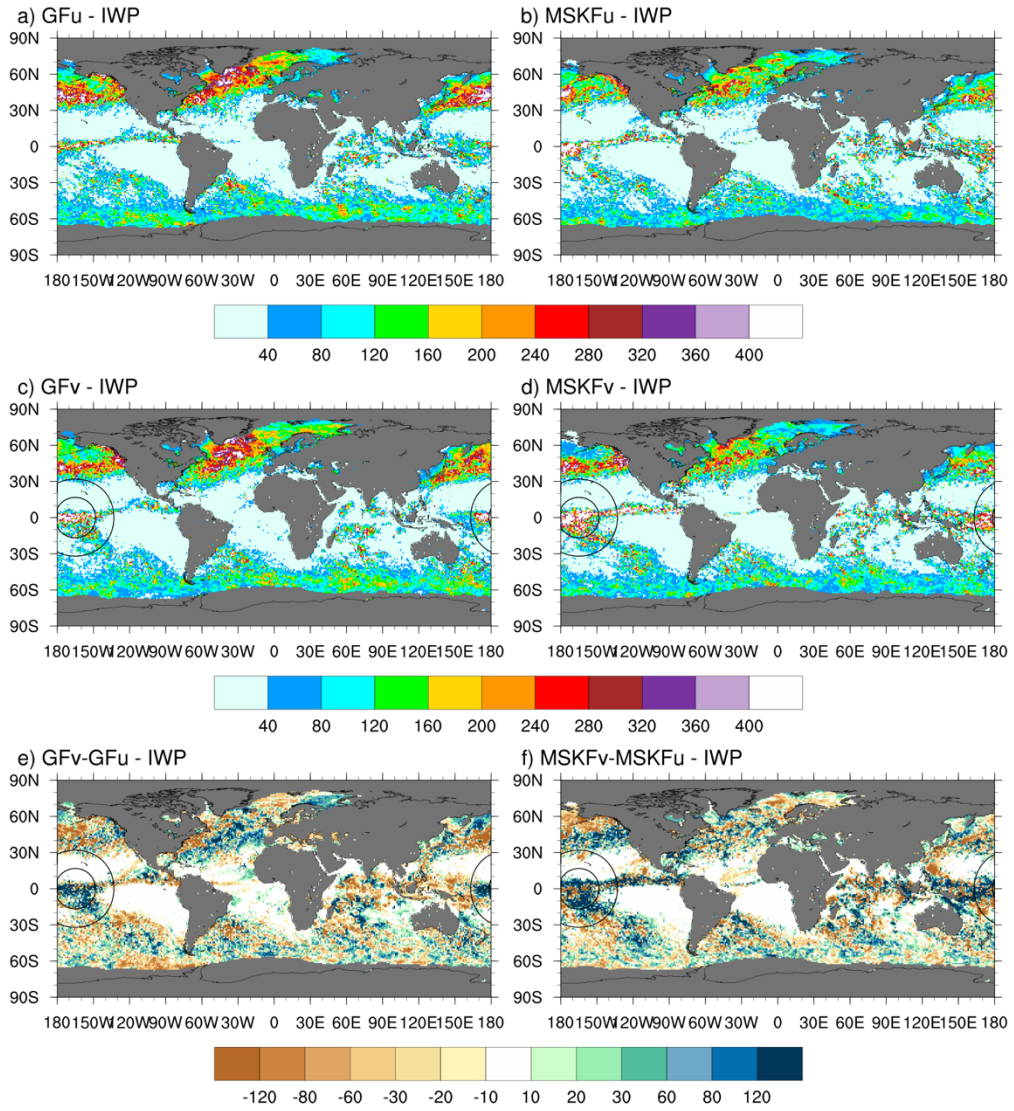


Figure 17: As Fig. 14, but for the cloud ice water path (IWP)

CONVECTIVE PRECIPITATION RATE (mm day<sup>-1</sup>)

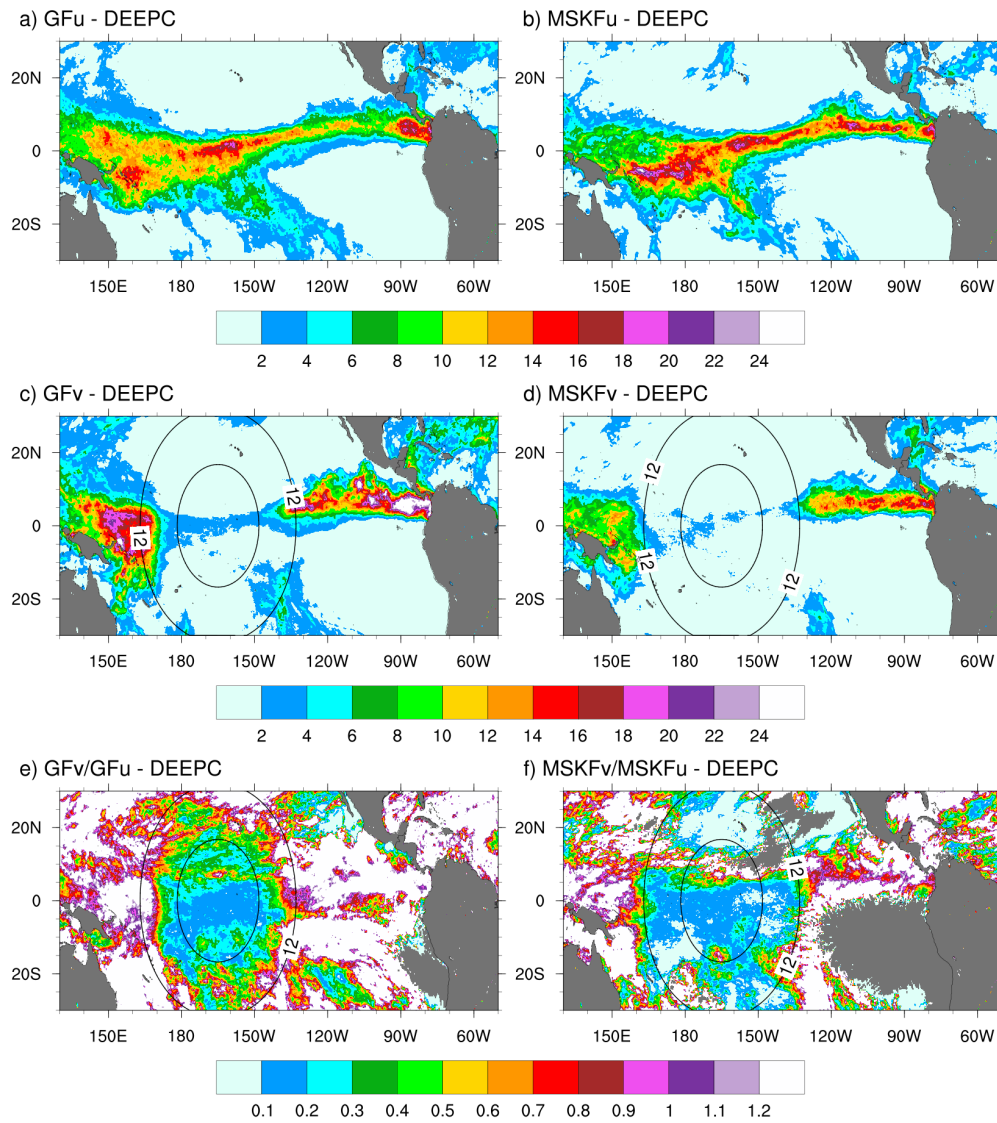


Figure A1: Monthly-mean convective (DEEPC) precipitation rate over the Tropical Pacific Ocean simulated in GFu and MSKFu (top panels) and GFv and MSKFv (bottom panels) for December 2015.

GRID-SCALE PRECIPITATION RATE (mm day<sup>-1</sup>)

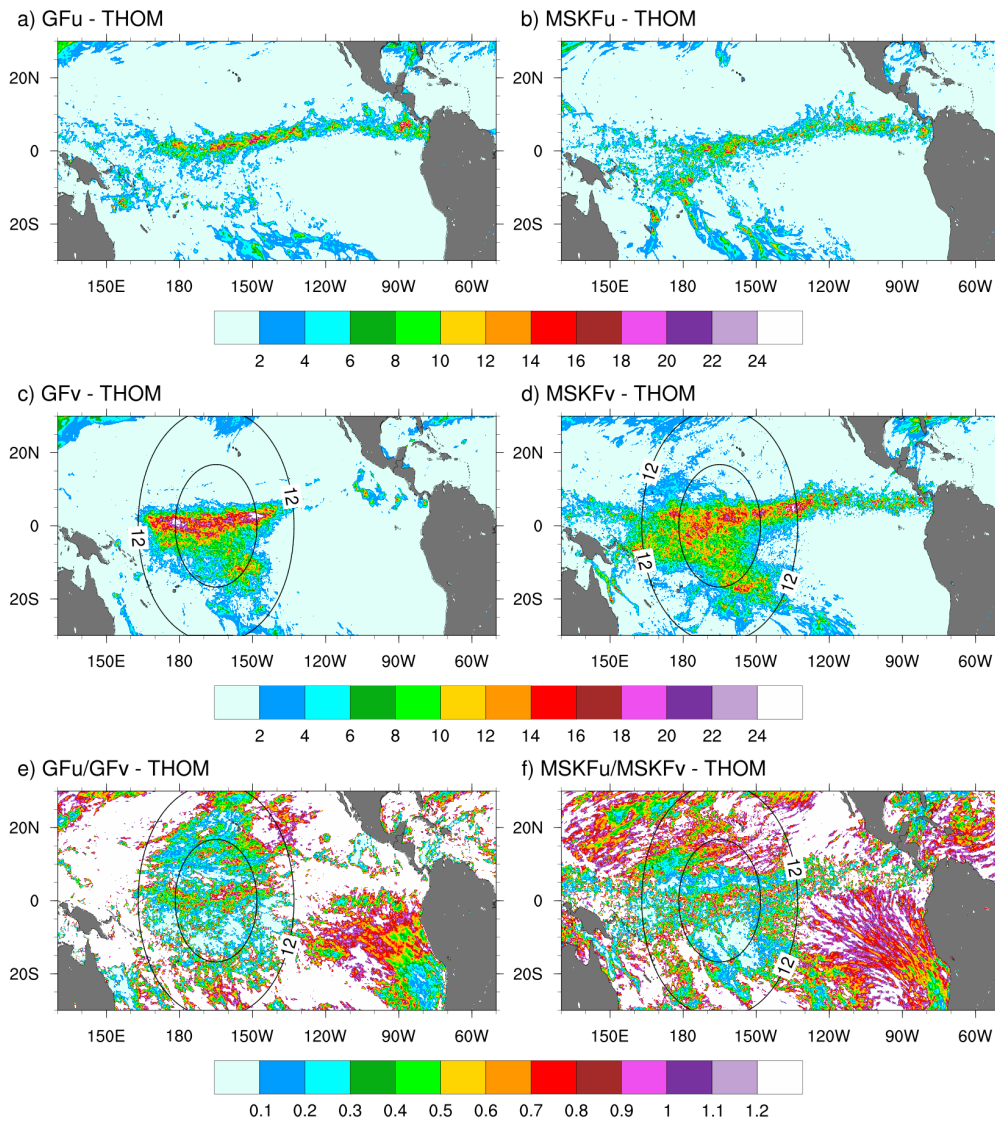


Figure A2: As Fig. A1, but for the monthly-mean grid-scale (THOM) precipitation rate.

**List of Additional Figures in response to “Major concerns 1) Applicability of 30-day runs for evaluating “average” model state, systematic biases” from Referee 2.**

Figure 4r: 10 day-mean cloud liquid water path (LWP, top panels), cloud ice water path (IWP, middle panels), and cloud fraction (CLD, bottom panels) over the Tropical Pacific Ocean for December 2015 from the Aqua satellite. Panels a), c), and e) are for the lower cloud layer; panels b), d), and f) are for the upper cloud layer.

Figure 5r: Cloudy area-weighted cloud liquid water path (LWP, top panels), cloudy area-weighted cloud ice water (IWP, middle panels), and cloud fraction (bottom panels) over the Tropical Pacific Ocean for December 2015. Panels a), c), and e) are monthly-mean SSF data; panels b), d), and f) are 10-day mean SSF data.

Figure 6r: 10-day mean incidence of shallow convection (SHALC) over the Tropical Pacific Ocean simulated in GFu and MSKFu (top panels) and GFv and MSKFv (middle panels), and difference in the incidence of shallow convection between GFv and GFu (bottom left panels) and MSKFv and MSKFu (bottom right panels).

Figure 7r: As Fig. 6r, but for the 10-day mean incidence of deep convection (DEEPC).

Figure 8r: 10-day mean convective (DEEPC) precipitation rate over the Tropical Pacific Ocean simulated in GFu (top panels) and GFv and MSKFv (bottom panels).

Figure 9r: As Fig. 8r, but for the 10-day mean grid-scale (THOM) precipitation rate.

Figure 10r: 10-day mean total precipitation over the Tropical Pacific Ocean from TMPA data (top panel) and simulated with GFu and MSKFu (middle panels) and GFv and MSKFv (bottom panels).

Figure 11r: 10-day mean precipitation rate difference over the Tropical Pacific Ocean between GFu (MSKFu) and TMPA data (top panels), GFv (MSKFv) and TMPA data (middle panels), and between GFv (MSKv) and GFu (MSKFu) (bottom panels).

Figure 14r: 10-day mean cloud liquid water path (LWP) over the Tropical Pacific Ocean simulated with GFu and MSKFu (top panels) and GFv and MSKFv (middle panels), and 10-day mean LWP differences between GFv and GFu, and MSKFv and MSKFu (bottom panels).

Figure 17r: As Fig. 14r, but for the cloud ice water path (IWP).

Figure S4r: 10-day mean vertically-integrated cloud fraction (TOACF) over the Tropical Pacific Ocean from a) CERES-SSF data, and difference in the TOACF between GFu (MSKFu) and CERES-SSF (middle panels) and between GFv (MSKFv) and CERES-SSF (bottom panels) for December 2015.

Figure S5r: 10-day mean TOA upward longwave radiation (TOALW) over the Tropical Pacific Ocean from a) CERES-SSF data, and difference in the TOALW between GFu (MSKFu) and CERES-SSF (middle panels) and between GFv (MSKFv) and CERES-SSF (bottom panels).

Figure S6r: As Fig. S5r, but for the TOA net shortwave radiation (TOASW).



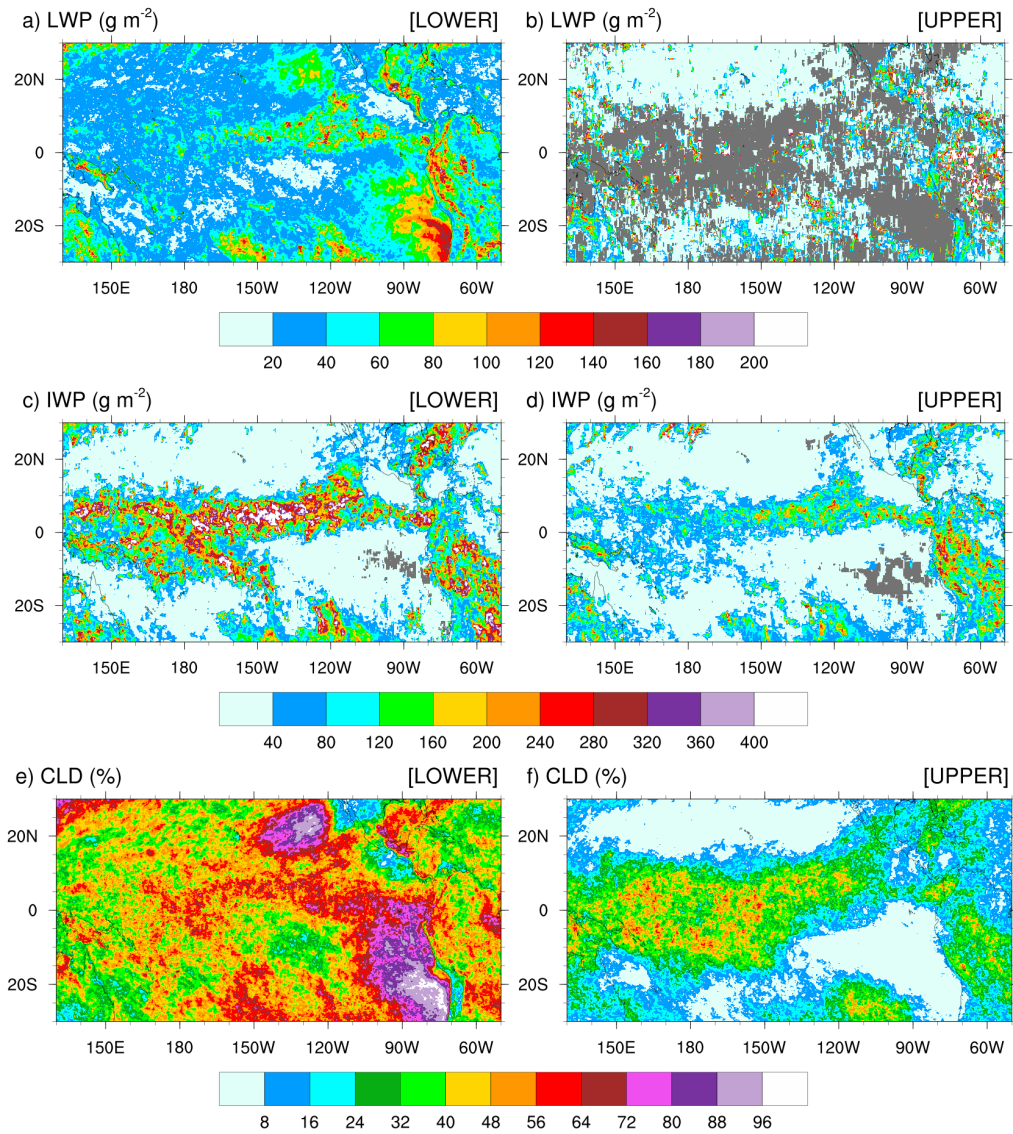


Figure 4r: 10 day-mean cloud liquid water path (LWP, top panels), cloud ice water path (IWP, middle panels), and cloud fraction (CLD, bottom panels) over the Tropical Pacific Ocean for December 2015 from the Aqua satellite. Panels a), c), and e) are for the lower cloud layer; panels b), d), and f) are for the upper cloud layer.

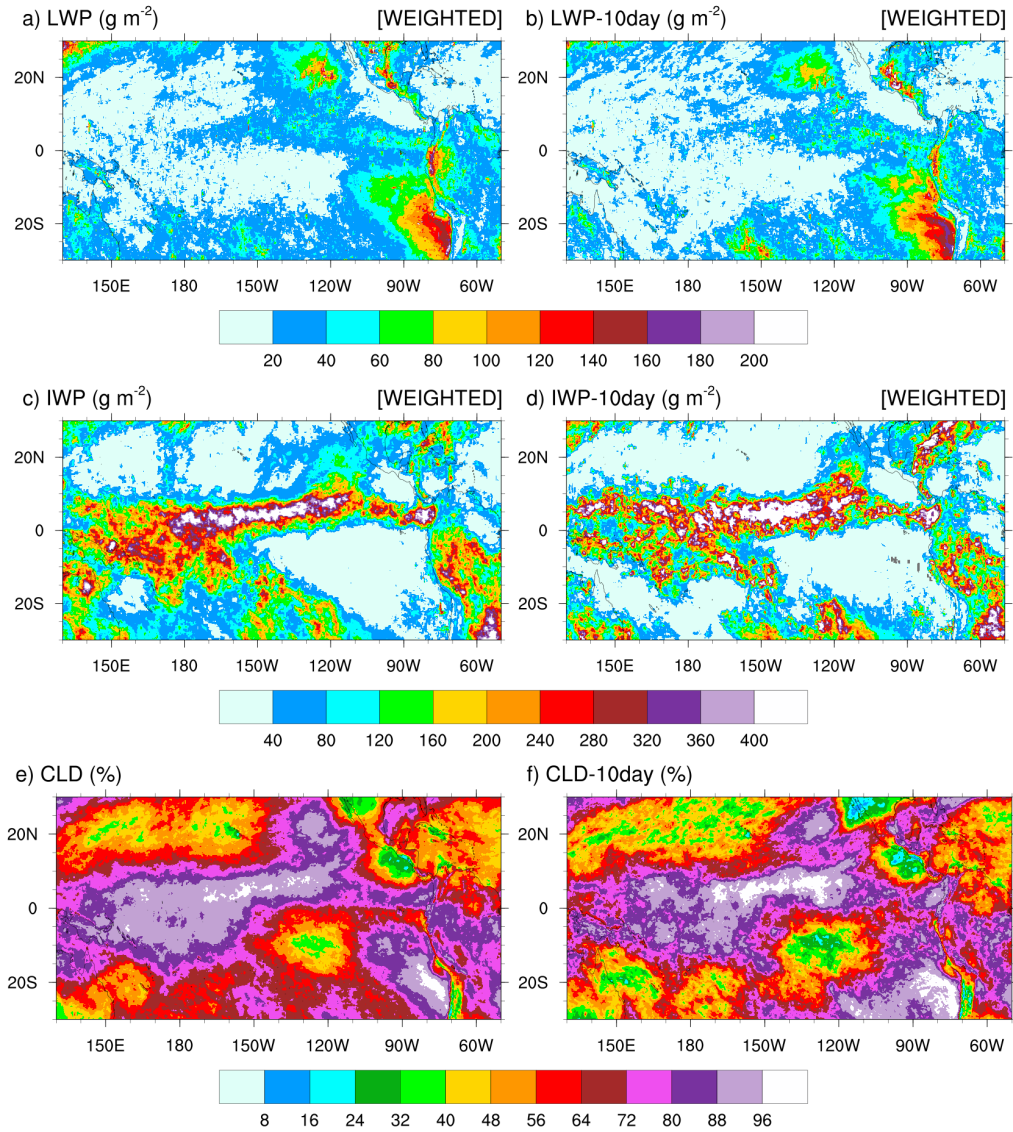


Figure 5r: Cloudy area-weighted cloud liquid water path (LWP, top panels), cloudy area-weighted cloud ice water (IWP, middle panels), and cloud fraction (bottom panels) over the Tropical Pacific Ocean for December 2015. Panels a), c), and e) are monthly-mean SSF data; panels b), d), and f) are 10-day mean SSF data.

10-DAY INCIDENCE OF SHALLOW CONVECTION (%)

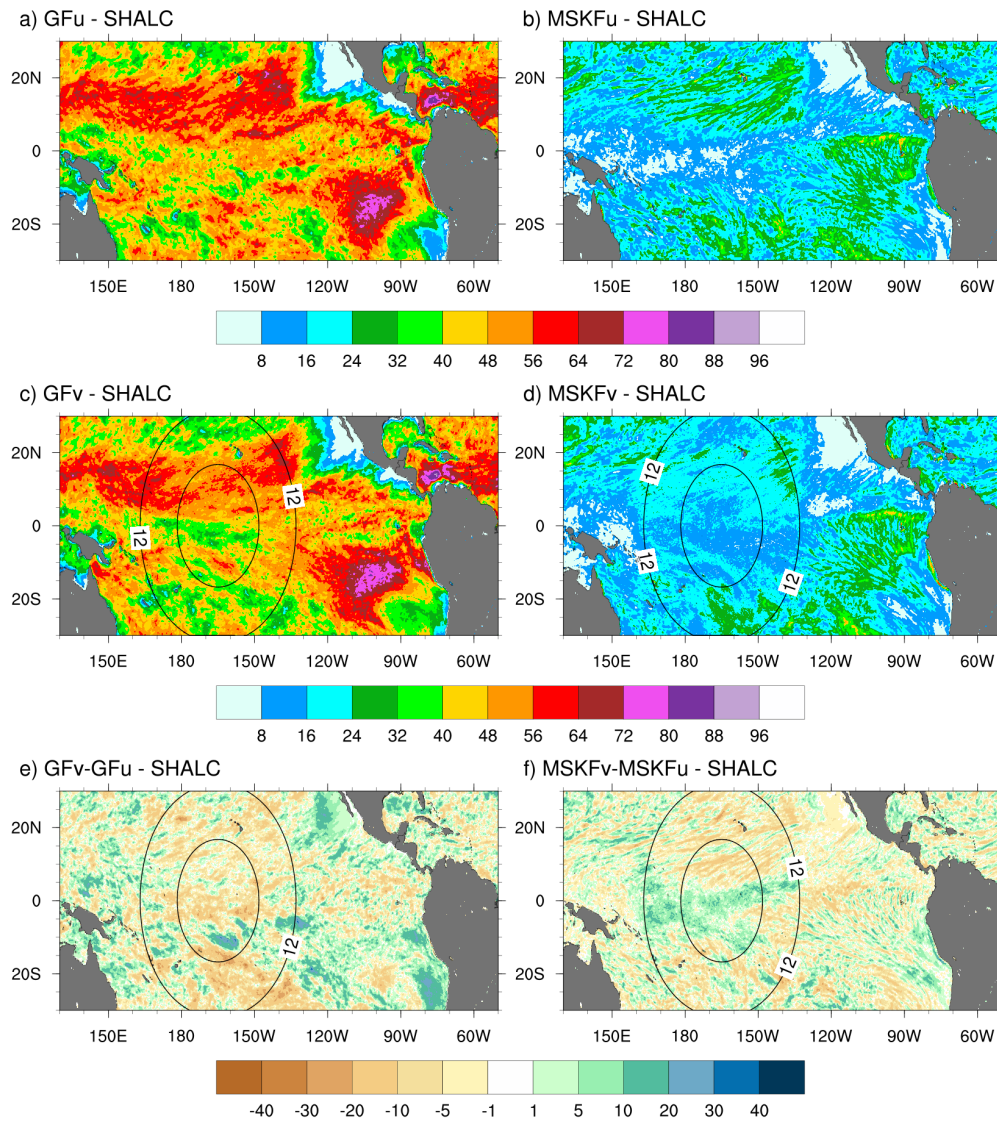


Figure 6r: 10-day mean incidence of shallow convection (SHALC) over the Tropical Pacific Ocean simulated in GFu and MSKFu (top panels) and GFv and MSKFv (middle panels), and difference in the incidence of shallow convection between GFv and GFu (bottom left panels) and MSKFv and MSKFu (bottom right panels).

10-DAY INCIDENCE OF DEEP CONVECTION (%)

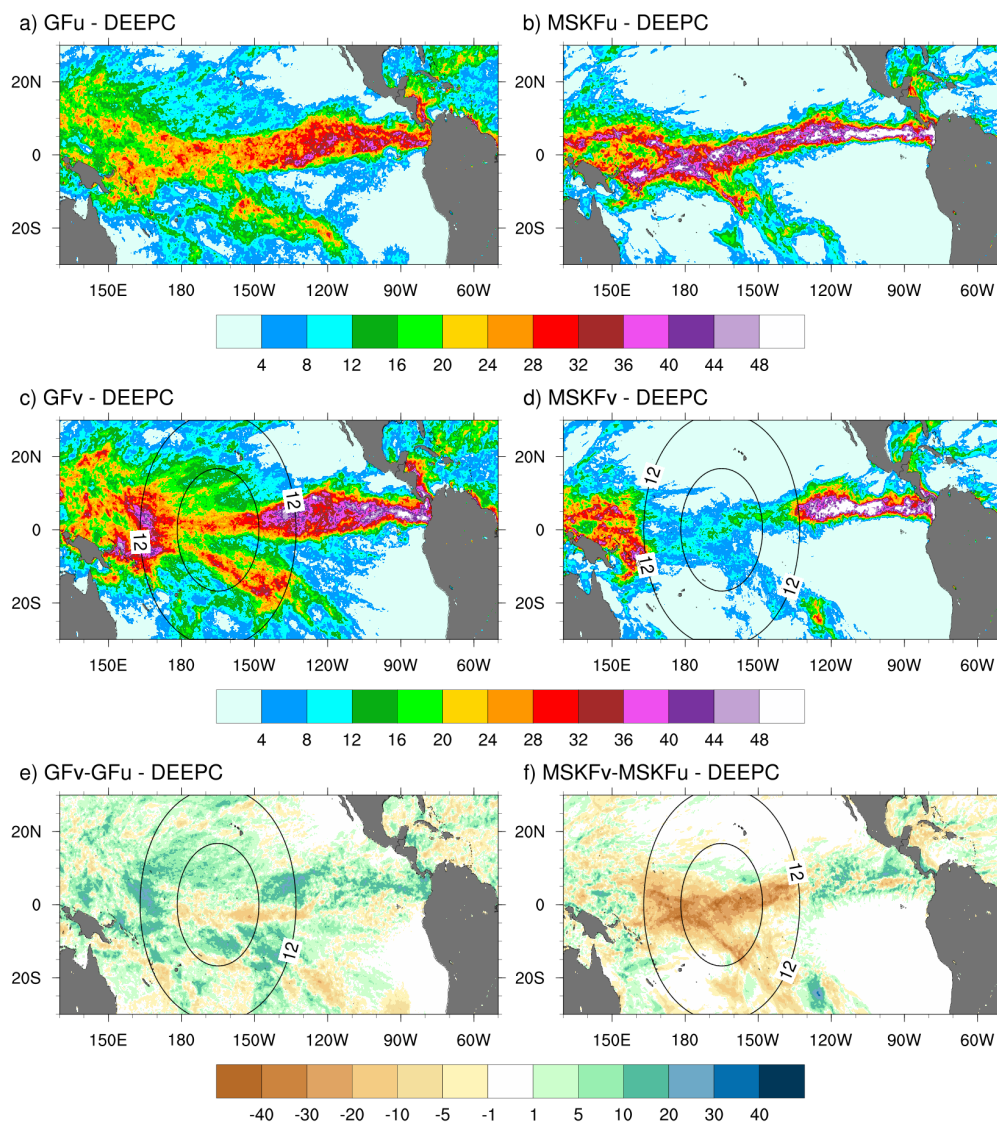


Figure 7r: As Fig. 6r, but for the 10-day mean incidence of deep convection (DEEPC).

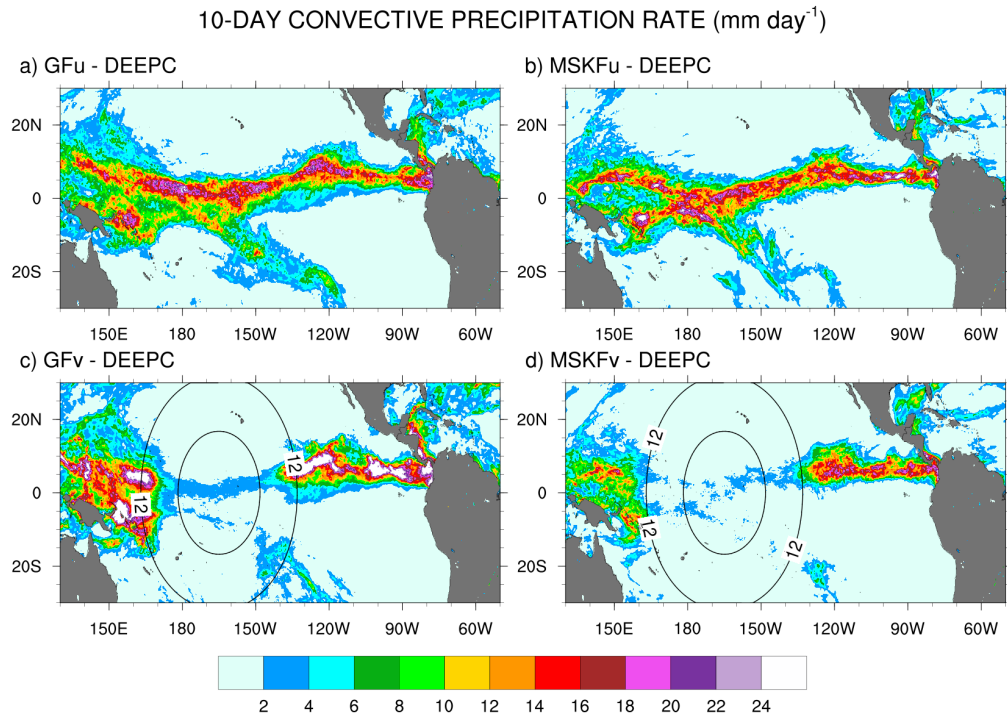


Figure 8r: 10-day mean convective (DEEPC) precipitation rate over the Tropical Pacific Ocean simulated in GFu (top panels) and GFv and MSKFv (bottom panels).

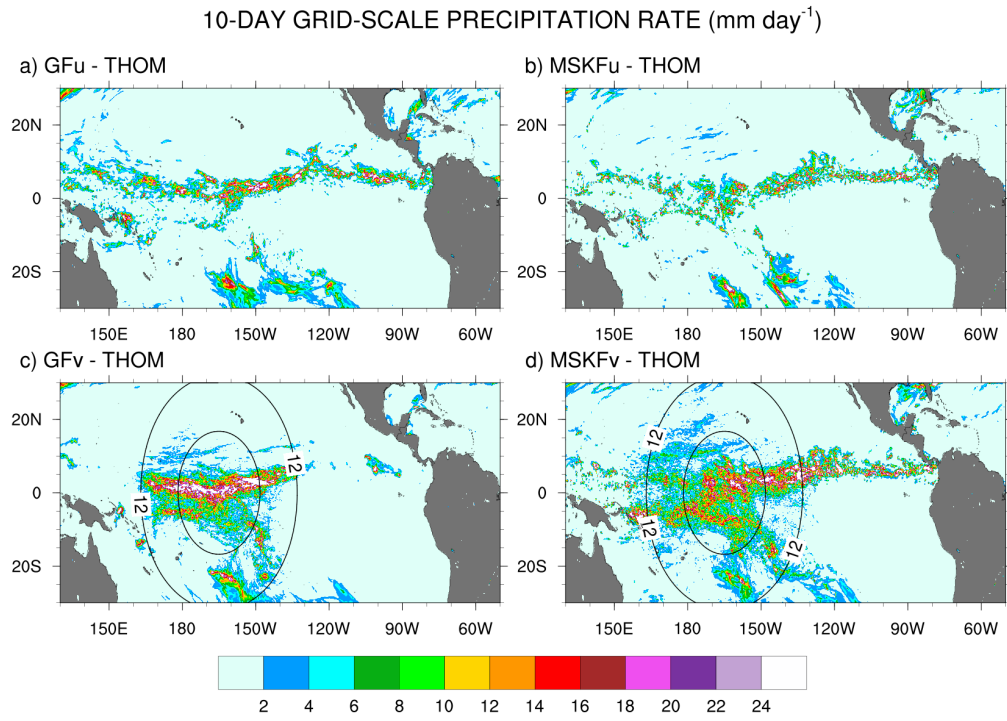


Figure 9r: As Fig. 8r, but for the 10-day mean grid-scale (THOM) precipitation rate.

10-DAY TOTAL PRECIPITATION RATE (mm day<sup>-1</sup>)

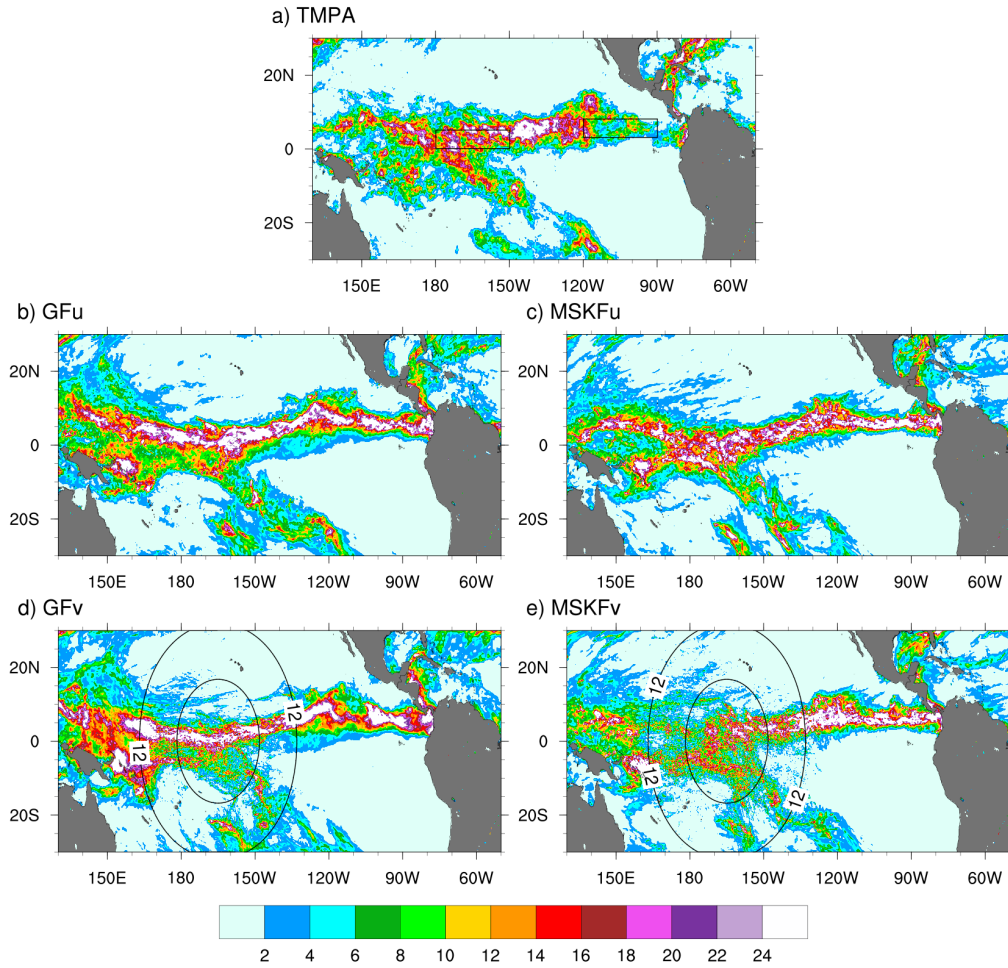


Figure 10r: 10-day mean total precipitation over the Tropical Pacific Ocean from TPA data (top panel) and simulated with GFu and MSKFu (middle panels) and GFv and MSKFv (bottom panels).

10-DAY PRECIPITATION RATE DIFFERENCE (mm day<sup>-1</sup>)

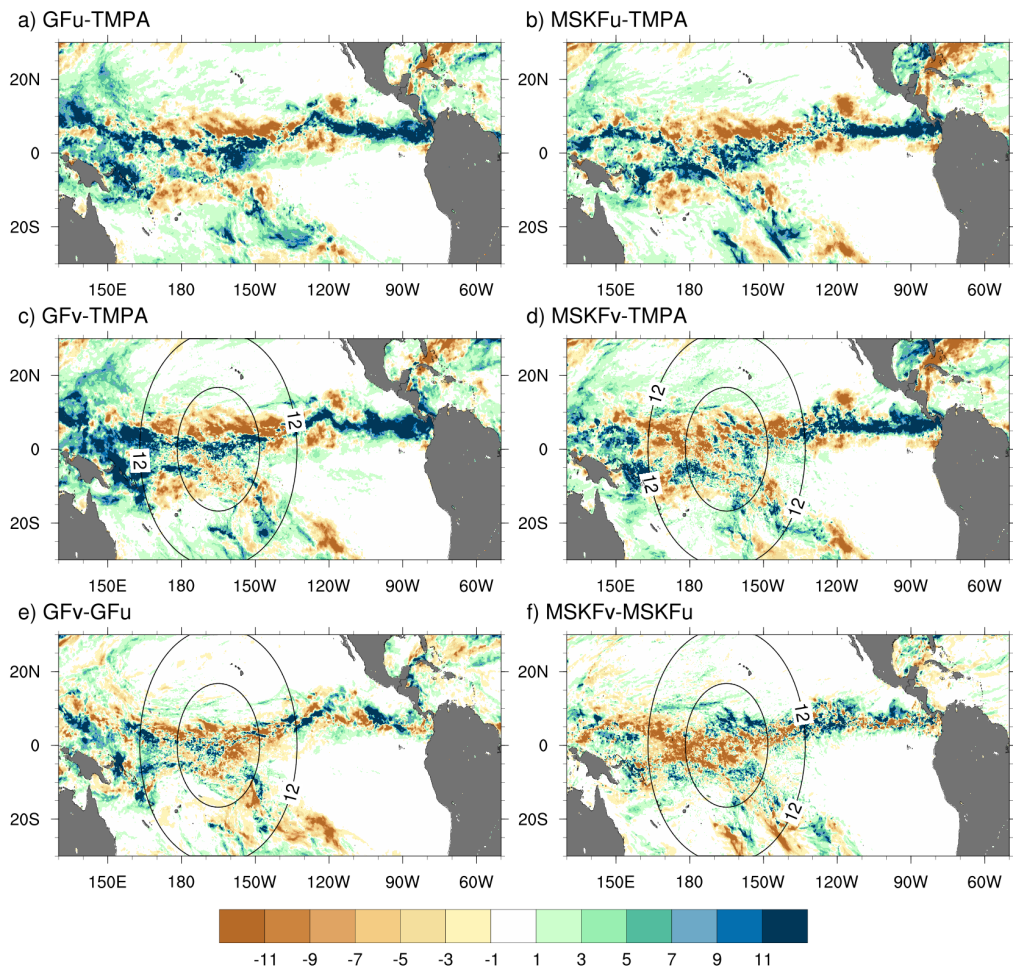


Figure 11r: 10-day mean precipitation rate difference over the Tropical Pacific Ocean between GFu (MSKFu) and TMPA data (top panels), GFv (MSKFv) and TMPA data (middle panels), and between GFv (MSKv) and GFu (MSKFu) (bottom panels).



10-DAY CLOUD LIQUID WATER PATH ( $\text{g m}^{-2}$ )

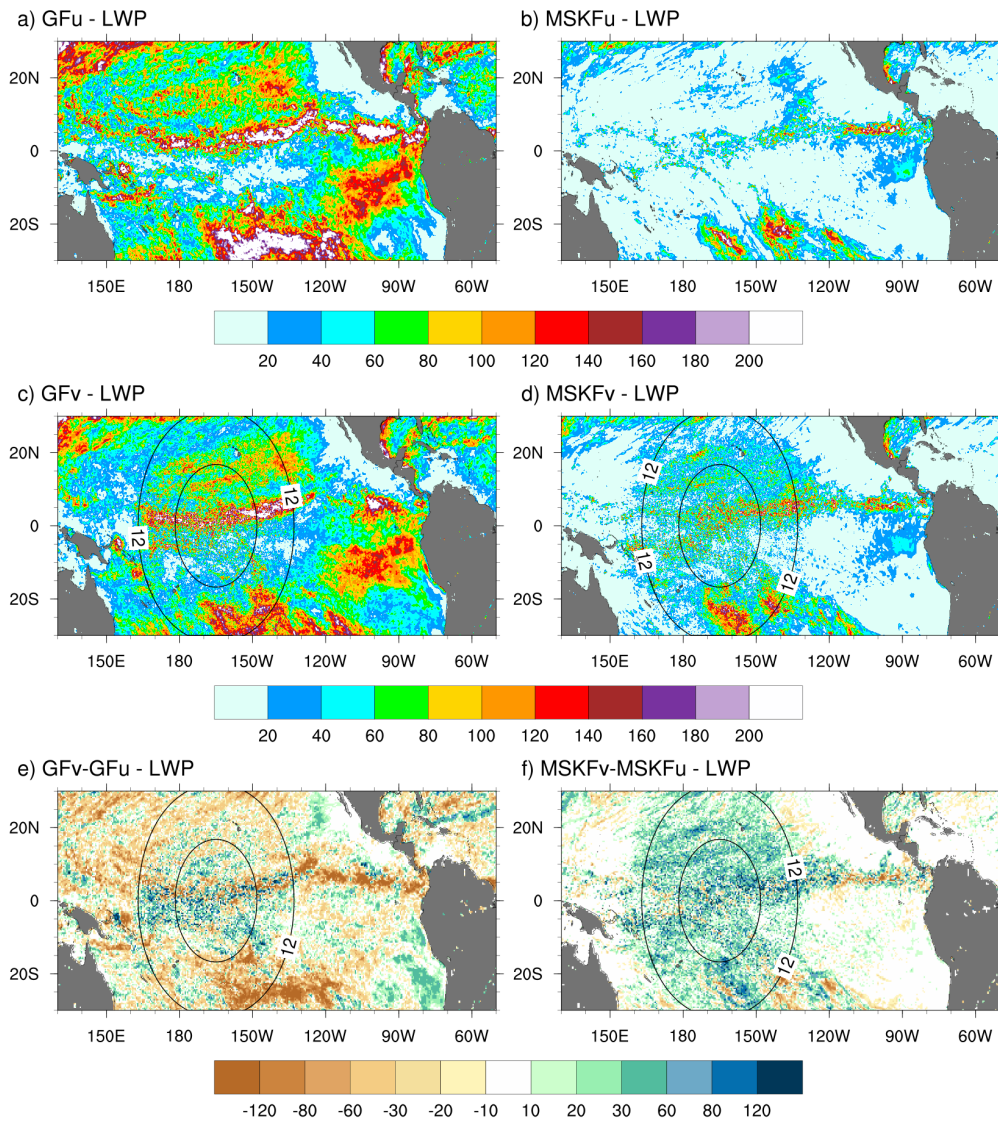


Figure 14r: 10-day mean cloud liquid water path (LWP) over the Tropical Pacific Ocean simulated with GFu and MSKFu (top panels) and GFv and MSKFv (middle panels), and 10-day mean LWP differences between GFv and GFu, and MSKFv and MSKFu (bottom panels).

10-DAY CLOUD ICE WATER PATH ( $\text{g m}^{-2}$ )

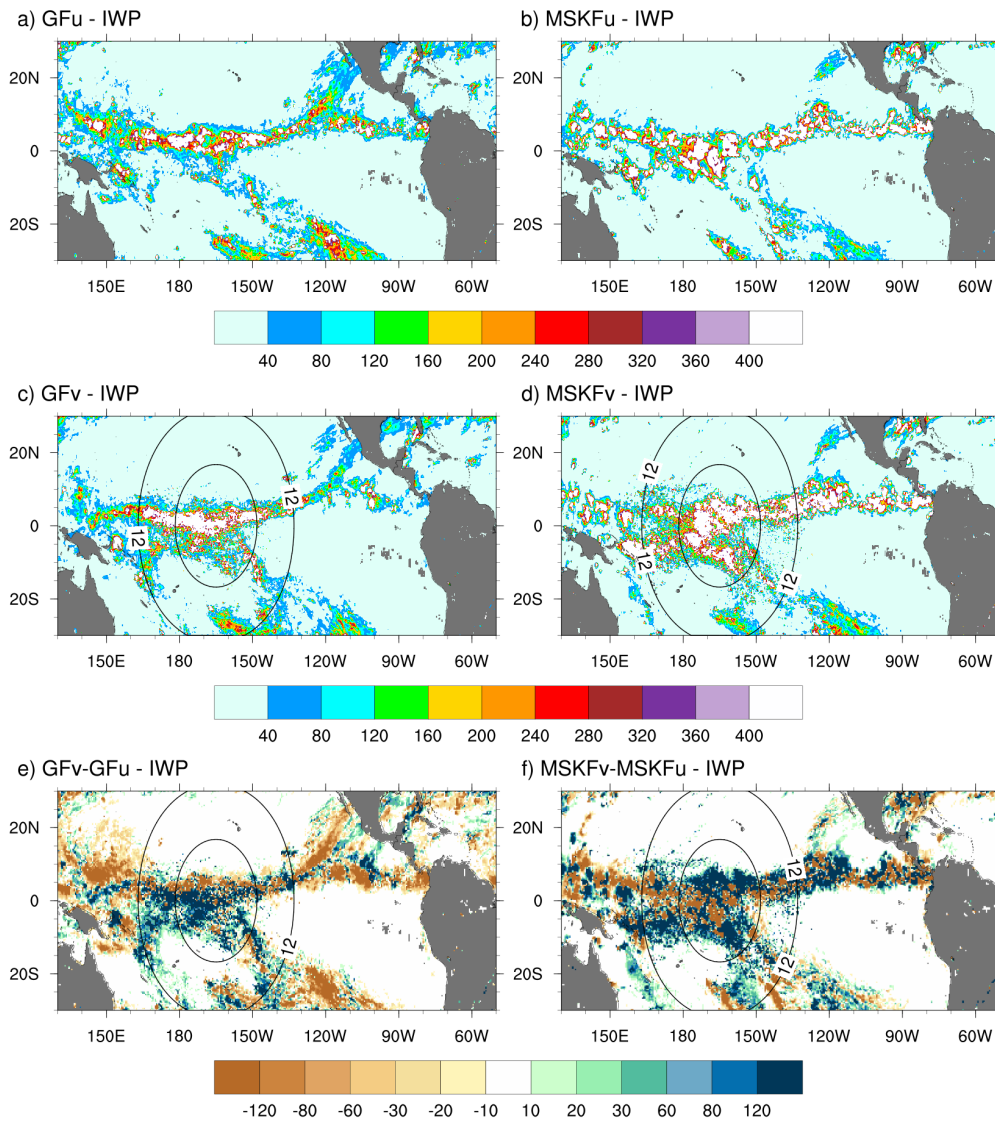


Figure 17r: As Fig. 14r, but for the cloud ice water path (IWP).

10-DAY TOA CLOUDINESS (%)

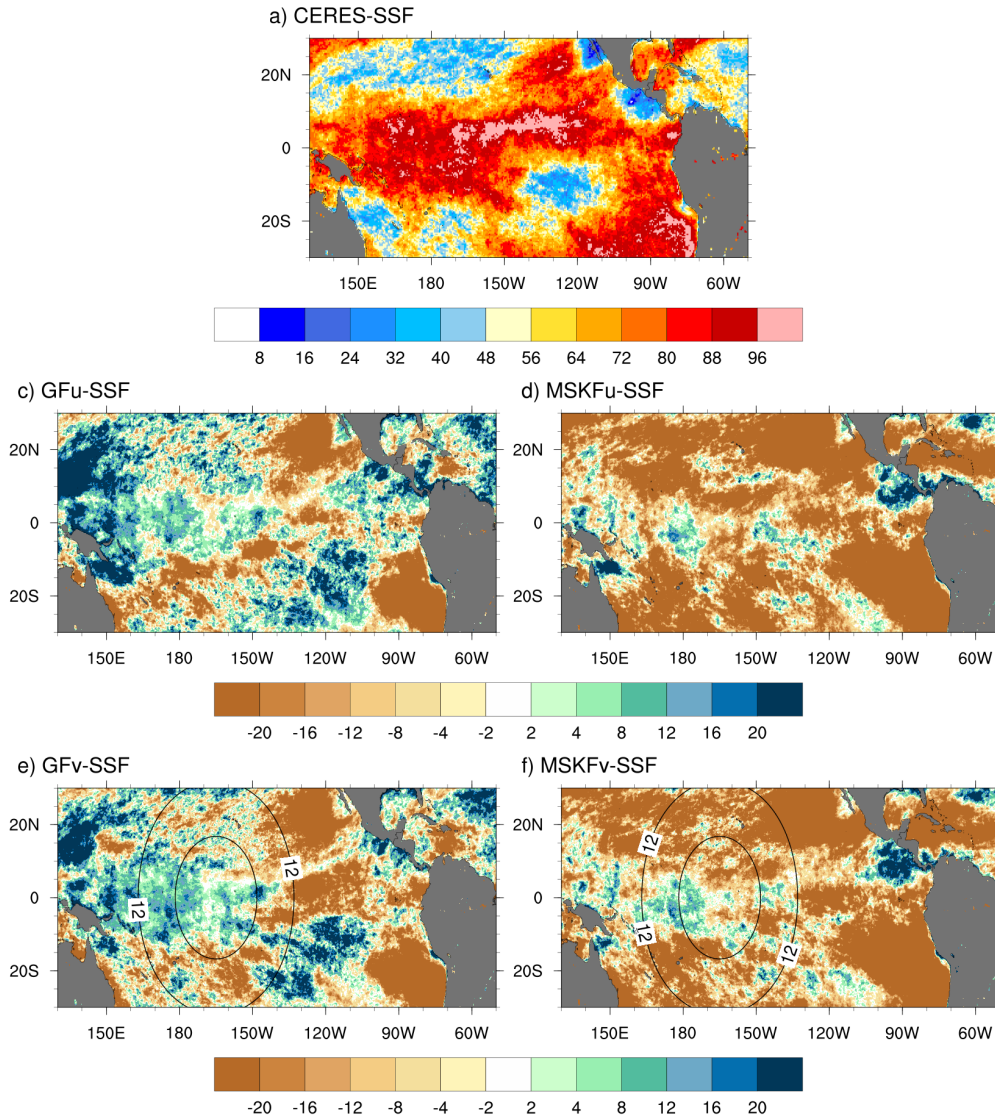


Figure S4r: 10-day mean vertically-integrated cloud fraction (TOACF) over the Tropical Pacific Ocean from a) CERES-SSF data, and difference in the TOACF between GFu (MSKFu) and CERES-SSF (middle panels) and between GFv (MSKFv) and CERES-SSF (bottom panels) for December 2015.

10-DAY TOA UPWARD LONGWAVE RADIATION ( $W m^{-2}$ )

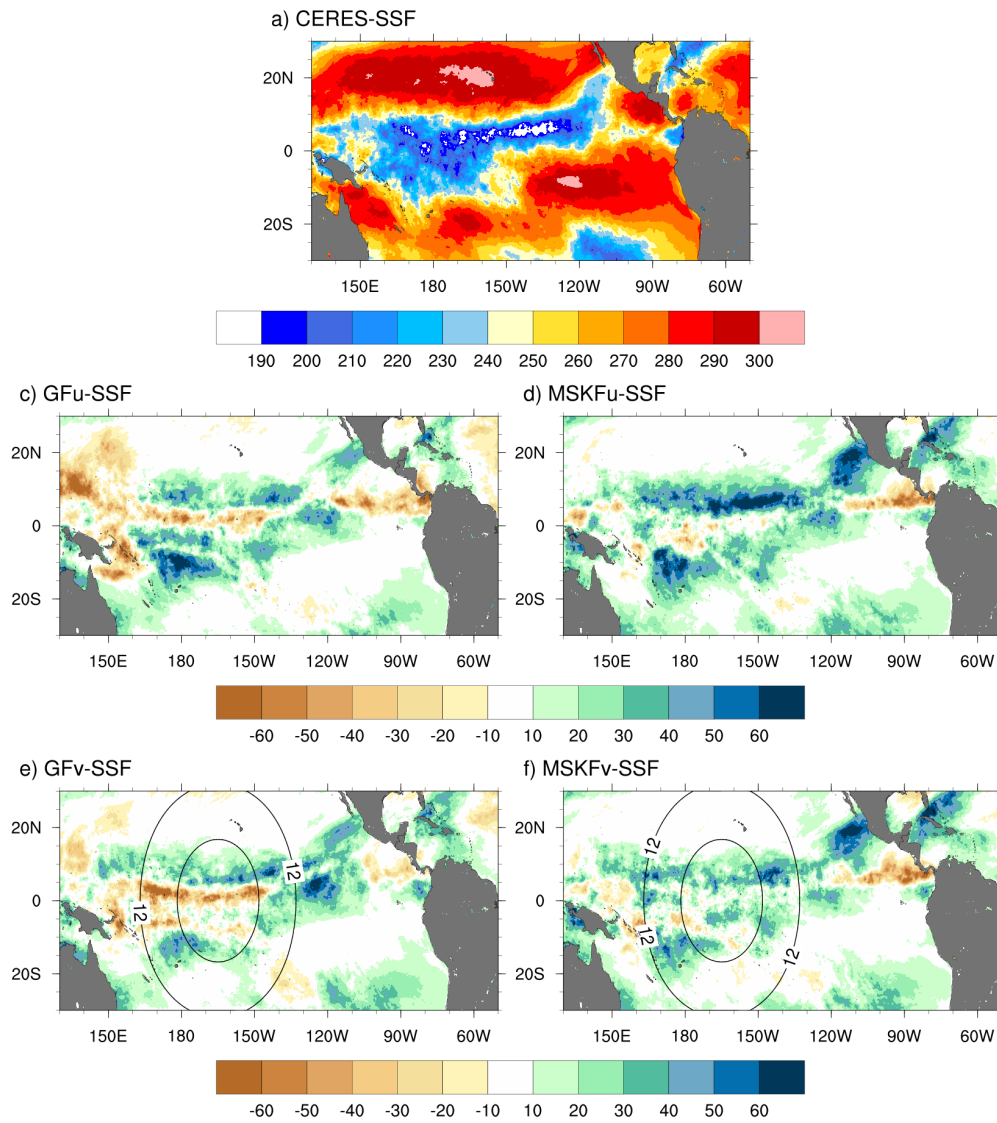


Figure S5r: 10-day mean TOA upward longwave radiation (TOALW) over the Tropical Pacific Ocean from a) CERES-SSF data, and difference in the TOALW between GFu (MSKFu) and CERES-SSF (middle panels) and between GFv (MSKFv) and CERES-SSF (bottom panels).

10-DAY TOA NET SHORTWAVE RADIATION ( $W m^{-2}$ )

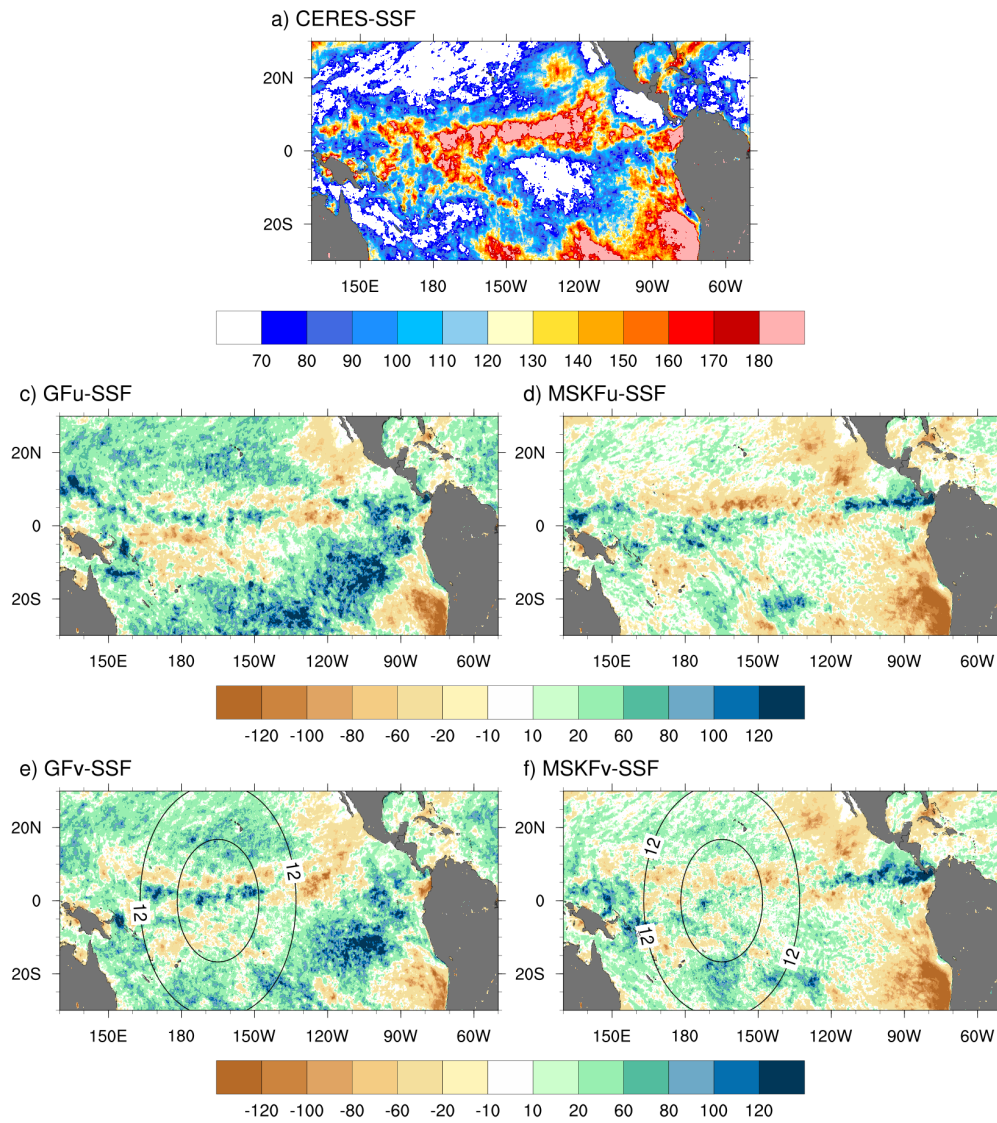


Figure S6r: As Fig. S5r, but for the TOA net shortwave radiation (TOASW).

1 **Impact of scale-aware deep convection on the cloud liquid and ice water paths and precipitation using the**  
2 **Model for Prediction Across Scales (MPAS-v5.2)**

3 **Laura D. Fowler<sup>1</sup>, Mary C. Barth<sup>1</sup>, and Kiran Alapaty<sup>2</sup>**

4 <sup>1</sup>National Center for Atmospheric Research, Boulder, Colorado

5 <sup>2</sup>Center for Environmental Measurements and Modeling, U.S. Environmental Protection Agency  
6 Research Triangle Park, North Carolina

7  
8  
9 Revised for Geoscientific Model Development  
10 February 2020

**Style Definition:** Normal: Indent: First line: 0.25"

**Style Definition:** NoIndent

**Style Definition:** Caption

**Style Definition:** List Paragraph: Indent: First line: 0.25",  
Add space between paragraphs of the same style

**Style Definition:** MS title: Indent: First line: 0.25", Add  
space between paragraphs of the same style

**Style Definition:** Affiliation: Indent: First line: 0.25", Add  
space between paragraphs of the same style

**Style Definition:** Equation: Centered, Indent: First line:  
0.25"

**Style Definition:** Authors: Indent: First line: 0.25", Add  
space between paragraphs of the same style

**Deleted:** September 2019

11  
12  
13  
14  
15  
16  
17  
18  
19  
20  
21  
22  
23  
24  
25  
26  
27  
28  
29  
30  
31  
32  
33  
34  
35  
36  
37  
38  
39  
40  
41  
42  
43  
44  
45  
46  
47  
48  
49 *Corresponding author address:* Dr. Laura D. Fowler, National Center for Atmospheric Research. P.O. Box 3000,  
50 Boulder, CO 80307-3000, USA.  
51 E-mail: [laura@ucar.edu](mailto:laura@ucar.edu)

54 **Abstract.** The cloud Liquid Water Path (LWP), Ice Water Path (IWP), and precipitation simulated with uniform-  
55 and variable-resolution numerical experiments using the Model for Prediction Across Scales (MPAS) are compared  
56 against Clouds and the Earth's Radiant Energy System (CERES) and Tropical Rainfall Measuring Mission data. Our  
57 comparison between monthly mean model diagnostics and satellite data focuses on the convective activity regions of  
58 the Tropical Pacific Ocean, extending from the Eastern Tropical Pacific Basin where trade wind boundary layer clouds  
59 develop to the Western Pacific warm pool defined by deep convective updrafts capped with extended upper-  
60 tropospheric ice clouds. Using the scale-aware Grell-Freitas (GF) and Multi-Scale Kain-Fritsch (MSKF) convection  
61 schemes in conjunction with the Thompson cloud microphysics, uniform-resolution experiments produce large biases  
62 between simulated and satellite-retrieved LWP, IWP, and precipitation. Differences in the treatment of shallow  
63 convection lead the LWP to be strongly overestimated when using GF while being in relatively good agreement when  
64 using MSKF compared to CERES data. Over areas of deep convection, uniform- and variable-resolution experiments  
65 overestimate the IWP with both MSKF and GF, leading to strong biases in the top-of-the-atmosphere long- and short-  
66 wave radiation relative to satellite-retrieved data. Mesh refinement over the Western Pacific warm pool does not lead  
67 to significant improvement in the LWP, IWP, and precipitation due to increased grid-scale condensation, and upward  
68 vertical motions. Results underscore the importance of evaluating clouds, their optical properties, and the top-of-the-  
69 atmosphere radiation budget in addition to precipitation when performing mesh refinement global simulations.

**Deleted:** scheme

**Deleted:** numerical

**Deleted:** using

**Deleted:** lead to increased IWP than those using

**Deleted:** conjunction with increased convective detrainment

**Deleted:** cloud ice and ice nucleation.

**Deleted:** yields increased

**Deleted:** , LWP, IWP, and cloudiness over the refined area of the mesh associated with increased grid-scale

## 70 1 Introduction

71 Comparing simulated against observed global cloud liquid and ice water paths (LWP and IWP) remains challenging  
72 because of uncertainties in parameterizing moist processes and cloudiness in global climate and numerical weather  
73 prediction (NWP) models, and errors in retrieving the LWP and IWP from satellite measurements. Cloud simulations  
74 from general circulation models (GCMs) involved in Phase 3 and 5 of the Coupled Model Intercomparison Project  
75 (CMIP3; CMIP5; Meehl et al., 2007; Taylor et al., 2012) display a strong disparity in the simulated LWP (Jiang et al.,  
76 2012; Li et al., 2018) and IWP (Li et al., 2012), producing annual mean LWP and IWP overestimated by factors of 2  
77 to 10, compared to satellite data. Satellite observations of the LWP and IWP from passive nadir viewing instruments  
78 such as the Moderate-resolution Imaging Spectroradiometer (MODIS; Minnis et al., 2011), and profiling radar such  
79 as the 94-GHz instrument on the CloudSat satellite (Stephens et al., 2002), also display major differences among  
80 themselves, as discussed in Li et al. (2008) and Waliser et al. (2009). While models and satellite retrievals agree that  
81 the LWP and IWP should be defined as the vertically-integrated liquid and ice water content, including all  
82 nonprecipitating and precipitating hydrometeors, this is not always the case in practice, further challenging a clearly-  
83 posed data-data and model-data comparison. Defining the LWP and IWP varies between models, depending on the  
84 complexity of the parameterization of cloud microphysics processes and prognostic versus diagnostic treatment of  
85 falling hydrometeors. Defining the measured LWP and IWP varies between satellite products, depending on the  
86 sensitivity of the observing systems to detect large precipitating particles. While comparing simulated and observed  
87 LWP and IWP may not be as straightforward as comparing the top-of-the-atmosphere (TOA) radiation budget (Dolinar  
88 et al., 2015; Stanfield et al., 2015), it offers a different way to directly diagnose biases in simulated total cloud liquid

**Deleted:** when

99 and ice water mass as a first step to help correct deficiencies in parameterizing global scale moist processes and  
100 precipitation.

101 Before the launch of the CloudSat and Cloud-Aerosol Lidar and Infrared Pathfinder Satellite Observation mission  
102 (Stephens et al., 2002), global estimates of the LWP and IWP were retrieved principally from satellite radiance  
103 measurements over different spectral intervals (e.g., Alishouse et al., 1990; Greenwald et al., 1993; Minnis et al., 1995;  
104 Platnick et al., 2003). In their critical review of most common methods developed to retrieve cloud and precipitation  
105 properties from satellite radiances, Stephens and Kummerow (2007) identify two main sources of errors. The first  
106 source of errors originates from the mandatory classification between cloudy and cloud-free scenes, and between  
107 precipitating and non-precipitating cloudy scenes. The second source of errors stems from using forward radiative  
108 transfer models that lack details of the vertical distribution of cloudiness and precipitation as well as complexity in  
109 specifying the optical properties of liquid water and ice particles. Estimating the LWP and IWP from CloudSat radar  
110 reflectivities alone presents its own set of challenges for scenes that include precipitating cloud systems due to the  
111 high sensitivity of radar reflectivities to the presence of large particles, for scenes that include mixed-phase and deep  
112 convective clouds, and close to the surface due to ground clutter. Li et al. (2018) show that annual mean maps of  
113 MODIS- and CloudSat-based LWP agree relatively well in tropical and subtropical regions if both data sets exclude  
114 LWP observations for deep convective/precipitating clouds since MODIS is quite insensitive to precipitation.  
115 Stephens and Kummerow (2007) advocate combining satellite-retrieved radar and radiance measurements to help  
116 validate simulated cloud properties and precipitation. In addition to considering the impact of precipitating particles,  
117 Waliser et al. (2009) demonstrate that a well-posed model-data comparison must include a consistent sampling  
118 between model outputs and satellite data to reduce diurnal sampling biases and sensitivity of the sensor and retrieval  
119 algorithm to the particle size when computing the simulated LWP and IWP.

120 Contemporary climate and NWP GCMs (Giorgetta et al., 2018; Molod et al., 2012; Kay et al., 2015; Skamarock  
121 et al., 2012) categorize moist processes into three distinct parameterizations, one to simulate turbulent mixing in the  
122 Planetary Boundary Layer (PBL) in response to surface forcing and forcing in the free troposphere, one to simulate  
123 subgrid scale shallow and deep convection, and one to include grid-scale cloud microphysics. While coupling between  
124 parameterizations varies between GCMs, it is an established practice to let detrained condensates from convective  
125 updrafts serve as sources for non-convective grid-scale clouds, as precipitating anvils and cirrus outflow. We suggest  
126 that uncertainties in parameterizing moist convection and impact on grid-scale clouds may explain a major part of the  
127 differences in the LWP and IWP simulated between the CMIP3 and CMIP5 GCMs. In recent years, efforts have been  
128 made to develop unified cloud parameterizations to represent all cloud types and alleviate the need to parameterize  
129 complex interactions between stratiform, shallow convective, and deep convective clouds (Guo et al., 2015; Storer et  
130 al., 2015; Thayer et al., 2015). Using the global Model for Prediction Across Scales (MPAS; Skamarock et al., 2012),  
131 Fowler et al. (2016) discuss the sensitivity of simulated precipitation as spatial resolution increases from hydrostatic  
132 to nonhydrostatic scales, and suggest to further analyze the associated sensitivity of simulated clouds and TOA  
133 radiation. Results show that as subgrid scale convective motions are increasingly resolved, diagnostic precipitation  
134 from the scale-aware Grell-Freitas (GF; Grell and Freitas, 2014) deep convection scheme decreases while prognostic  
135 precipitation from the WSM6 (Hong and Lim, 2006) cloud microphysics scheme increases over the refined area of



136 the variable-resolution mesh. Vertical profiles of the cloud liquid and ice water mixing ratios and cloud fraction  
137 highlight the redistribution of cloud condensates and relative humidity with height in the refined area in response to  
138 decreased contribution of convective detrainment of cloud liquid water and ice. However, Fowler et al. (2016) do not  
139 further address if variations in the vertical profiles of cloud condensates lead to improved LWP, IWP, and cloud optical  
140 properties against satellite-derived data.

141 The objectives of our research are threefold. First, we want to assert that our suite of PBL, deep and shallow  
142 convection, and cloud microphysics parameterizations tested in MPAS at hydrostatic and nonhydrostatic scales for  
143 medium-range spring forecasts over the Continental United States (Schwartz, 2019; Wong and Skamarock, 2016) can  
144 also be used to produce month-long simulations of tropical convection, narrowing our analysis on the Tropical Pacific  
145 Ocean. In order to broaden our research and possibly generalize our results, we also implemented the scale-aware  
146 MultiScale Kain-Fritsch (MSKF; Glotfelty et al., 2019; Zheng et al., 2016) parameterization of deep and shallow  
147 convection in addition to GF. Second, we want to evaluate the ability of MPAS to simulate the LWP, IWP, cloudiness,  
148 and TOA long- and short-wave radiation against the Clouds and the Earth’s Radiant Energy System (CERES; Wielicki  
149 et al., 1996) Single Scanner FootPrint (SSF; Minnis et al., 2011) data set, and precipitation against the TRMM  
150 Multisatellite Precipitation Analysis (TMPA; Huffman et al., 2007). Our third goal aims at understanding differences  
151 in the LWP, IWP, precipitation, and cloud radiative effects as functions of horizontal resolution with GF and MSKF  
152 using the capability of local mesh refinement developed for MPAS.

153 In Section 2, we summarize the characteristics of the GF and MSKF parameterizations of deep and shallow  
154 convection. In Section 3, we provide a short description of MPAS, including physics parameterizations used with both  
155 convective parameterizations, the design of our experiments using the uniform- and variable-resolution meshes, and  
156 description of the satellite data sets used to validate our results. In Section 4, we analyze our results in terms of  
157 precipitation and varying contribution of the convective and grid-scale precipitation to the total precipitation as a  
158 function of horizontal resolution. In Section 5, we compare the LWP, IWP, and TOA long- and short-wave radiation  
159 against satellite data. In Section 6, we summarize our results and propose areas of future research.

Deleted: with

Deleted: spatial

## 160 2 Description of the convective parameterizations

Deleted: parameterizations0

161 Mass flux-based convective parameterizations distinguish themselves through the use of different triggering  
162 functions to initiate convection, the details of their entraining-detraining cloud models, and formulation of their  
163 closures that control the intensity of convection and computation of the cloud base mass flux. For convective  
164 parameterizations that include deep and shallow convection, criteria that characterize the two kinds of convection  
165 strongly vary. Furthermore, how convective parameterizations account for the dependence of convection on the  
166 horizontal resolution differs in complexity. In this section, we summarize the chief characteristics of GF and MSKF,  
167 including differences in their treatment of deep and shallow convection, and spatial-scale dependence.

### 168 2.1 The Grell-Freitas (GF) parameterization

169 The version of GF used in our numerical experiments is that implemented in version 3.8.1 of the Advanced  
170 Research Weather Research Forecast model (Skamarock et al., 2008), as described in Grell and Freitas (2014). Its

174 properties were first discussed in Grell (1993) and later expanded by Grell and Devenyi (2002) to include  
 175 stochasticism. GF treats deep and shallow convection separately by using different initial entrainment rates ( $7 \times 10^{-5}$   
 176  $\text{m}^{-1}$  and  $1 \times 10^{-2} \text{m}^{-1}$  for deep and shallow convection, respectively) to control the depth of convective cloud layers and  
 177 closures to calculate the cloud base mass flux. GF includes an ensemble of closures from well-known convective  
 178 parameterizations to compute a mean cloud-base mass flux. For deep convection, these four closures are the *AS* closure  
 179 (Arakawa and Schubert, 1974) that assumes instantaneous equilibrium between the large-scale forcing and subgrid-  
 180 scale convection; the *W* closure (Brown, 1979; Frank and Cohen, 1987) that relates the cloud base mass flux to the  
 181 grid-scale upward vertical velocity; the *MC* closure (Krishnamurti et al., 1983) that calculates the cloud base mass  
 182 flux as a function of the vertically-integrated vertical moisture advection; and the *KF* closure (Kain and Fritsch, 1993)  
 183 that reduces the convective available potential energy over a prescribed convective time-scale. Qiao and Liang (2015)  
 184 analyze the separate and combined impacts of the four closures on the simulated summer precipitation over the United  
 185 States coastal oceans. On the one hand, they found that computing the cloud base mass flux using the *W* and *MC*  
 186 closures led to precipitation patterns and amounts that are in better agreement against TMPA data than those using the  
 187 *AS* and *KF* closures. On the other hand, they found that the *AS* and *KF* closures yield improved diurnal cycle of  
 188 precipitation relative to the other two closures. In our numerical experiments, GF gives an equal weight to each closure  
 189 to calculate the mean cloud base mass flux for deep convection. As for deep convection, GF includes different closures  
 190 for shallow convection. In our numerical experiments using GF, we choose the boundary layer quasi-equilibrium  
 191 (*BLQE*) closure of Raymond (1995) for shallow convection.

192 Both types of convection transport total water and moist static energy in a conservative manner but neglect to  
 193 include ice phase processes in updrafts and downdrafts. In this version of GF, the only feedback between shallow  
 194 convection and the large-scale environment is lateral and cloud-top detrainment of water vapor and corresponding  
 195 heating, as liquid water formed in shallow updrafts evaporates immediately. Deep convection returns potential  
 196 temperature, water vapor, and condensed water tendencies to the environment. Detrained condensed water acts as a  
 197 source of liquid water (ice) if the large-scale temperature is warmer (colder) than the prescribed 258 K threshold.  
 198 While GF assumes that shallow convective plumes are not deep enough to produce precipitation, the conversion of  
 199 liquid water to rain water in deep convective plumes depends on a simple Kessler-type (Kessler, 1969) conversion  
 200 threshold and precipitation reaches the surface instantaneously.

201 As discussed in Grell and Freitas (2014), deep convection includes a simplified representation of the unified  
 202 parameterization of deep convection described in Arakawa and Wu (2013). Arakawa and Wu (2013) demonstrate that  
 203 mass flux-based convective parameterizations can be modified to work at all resolutions spanning between hydrostatic  
 204 and **nonhydrostatic** scales through the reduction of the convective vertical eddy transport as a quadratic function of  
 205 the horizontal fraction of the grid box occupied by convective updrafts. In GF, the convective updraft fraction ( $\sigma$ ) is  
 206 computed as a simple function of the initial entrainment rate ( $\varepsilon = 7 \times 10^{-5} \text{m}^{-1}$ ) and half-width radius ( $R$ ) of convective  
 207 updrafts following Simpson and Wiggert (1969), or

208 
$$\sigma = \frac{\pi R^2}{4} \text{ and } R = \frac{0.2}{\varepsilon} \quad (1)$$

Deleted: non-hydrostatic

Formatted: Font: 10 pt, Bold

Formatted: Font: 10 pt

Formatted: Font: 10 pt, Bold

Formatted: Font: 10 pt, Bold

Formatted: Equation, Indent: Left: 0", First line: 0"

Formatted: Font: 10 pt, Bold

Formatted: Font: 10 pt, Bold

Formatted: Font: 10 pt

Formatted: Font: 10 pt, Bold

Formatted: Font: 10 pt

Formatted: Font: 10 pt, Bold

Formatted: Font: 10 pt

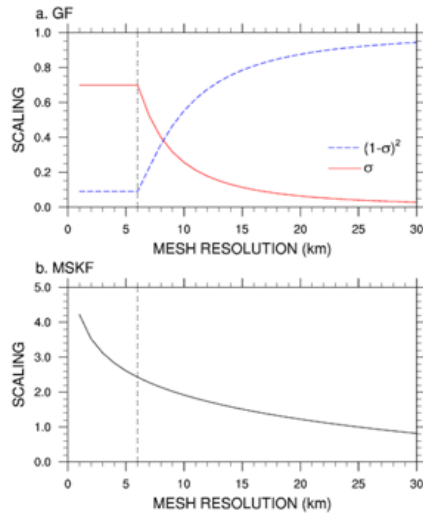
Formatted: Font: 10 pt, Bold

Formatted: Font: 10 pt, Bold

Formatted: Font: 10 pt, Bold

Field Code Changed

210 where  $A$  is the area of the grid box. In Eq. (1),  $\sigma$  is not allowed to exceed 0.7. As discussed in Fowler et al. (2016),  
 211 when  $\sigma$  becomes greater than 0.7,  $\sigma$  is set to 0.7 and  $\varepsilon$  is recalculated using Eq. (1), leading to increased entrainment  
 212 and decreased convective cloud-tops as  $A$  becomes smaller. Another option would be to turn off deep convection when  
 213  $\sigma$  reaches values close to 1, in which case a better choice for its maximum value may be between 0.9 and 1 (Grell and  
 214 Freitas, 2014). Figure 1.a highlights the rapid decrease in  $\sigma$  from 0.7 to 0.3 as spatial resolution decreases from 6 to  
 215 9 km.  $\sigma$  further decreases from 0.3 to 0.1 for resolutions between 9 and 16 km, and from 0.1 to 0.05 for resolutions  
 216 between 16 and 30 km. The  $(1-\sigma)^2$  quadratic function used to scale the mass flux starts to be significant at resolutions  
 217 greater than 20 km and decreases rapidly to a minimum value of 0.1 for horizontal grid-spacing smaller than 6 km.  
 218 Using a maximum value for  $\sigma$  ensures that over the most refined area of the mesh, parameterized deep convection is  
 219 not completely turned off since deep convection is not explicitly resolved. Using a variable-resolution mesh varying  
 220 between 50 km over the coarse area of the mesh down to 3 km over the refined area of the mesh centered over South  
 221 America, Fowler et al. (2016) show that the impact of parameterized deep convection weakens and that of grid-scale  
 222 cloud microphysics strengthens as horizontal grid-spacing increases from hydrostatic to nonhydrostatic scales.



223 **Figure 1:** a) Convective updraft fraction as a function of the mesh resolution used to scale the cloud base mass flux in GF; and b)  
 224 Scaling factor as a function of the mesh resolution used to scale the convective time scale in MSKF.  
 225

226 **2.2 The Multi-Scale Kain-Fritsch (MSKF) parameterization**

227 MSKF is the scale-aware version of the Kain-Fritsch (KF) convective parameterization, first developed by Kain  
 228 and Fritsch (1990; 1993), and later updated by Kain (2004) to include, among other improvements, non-precipitating  
 229 shallow convection. The trigger function is that used in Fritsch and Chappell (1980), originally tested in Kain and  
 230 Fritsch (1992) and recently in Suhas and Zhang (2014). In MSKF, convection may be triggered if the temperature of  
 231 a mixed layer is greater than that of the environment. The pressure thickness of that mixed layer must be at least 50

Deleted: cannot  
 Deleted: , as  
 Deleted: ).

Formatted: Font: Italic  
 Deleted: resolutions decrease  
 Deleted: .1  
 Deleted: .2  
 Formatted: Font: Italic  
 Deleted: .2  
 Deleted: spanning  
 Formatted: Font: Italic  
 Deleted: cloud-base  
 Deleted: significantly impact the cloud-base mass flux  
 Deleted: vertical motion  
 Deleted: non-hydrostatic

Formatted: Font: Bold

Deleted: the  
 Deleted: is



283 using the LCL as a function of the scale-dependent *Tokioka* parameter (Tokioka et al., 1988), a scale-dependent  
284 conversion rate for liquid water and ice condensates to precipitation, an increased grid-scale velocity expressed in  
285 terms of the subgrid scale updraft mass flux, and elimination of double counting of precipitation in cloudy layers. The  
286 separate and combined impacts of the development of MSKF on high resolution weather forecasts and regional climate  
287 simulations are discussed in Herwehe et al. (2014), Mahoney (2016), He and Alapaty (2018), Zheng et al. (2016), and  
288 Glotfelty et al. (2019).

### 289 3 Methodology

#### 290 3.1 Numerical experiments

291 We discuss differences in our MPAS results between GF and MSKF configurations on precipitation, cloud  
292 properties, and TOA radiation using 30-day long numerical experiments in MPAS (Skamarock et al., 2012). MPAS  
293 is a global nonhydrostatic atmospheric model developed for NWP and climate studies. The horizontal discretization  
294 uses an unstructured spherical centroidal Voronoi tessellation with a C-grid staggering, as described in Ju et al. (2011),  
295 while the vertical discretization is the height-based hybrid terrain-following coordinate of Klemp (2011). The  
296 dynamical solver integrates the prognostic equations (cast in flux form) for the horizontal momentum, vertical  
297 velocity, potential temperature, dry air density, and scalars using the split-explicit technique of Klemp et al. (2007).  
298 The temporal discretization uses a third-order Runge-Kutta scheme and the explicit time-splitting technique described  
299 in Wicker and Skamarock (2002). We use the monotonic option of the scalar transport scheme of Skamarock and  
300 Gassmann (2011) for horizontal and vertical advection of all moist scalars on the unstructured Voronoi mesh. Finally,  
301 horizontal filtering of the state variables is based on Smagorinsky (1963), as described in Skamarock et al. (2012). For  
302 variable-resolution meshes, the eddy viscosity coefficient is scaled as a function of the inverse mesh density so that  
303 horizontal diffusion is increased in the coarse area relative to the refined area of the mesh.

304 In MPAS, the computational flow includes three distinct steps. The first step calls the physics parameterizations  
305 that update the surface energy budget and calculate the tendencies of potential temperature, moist species, and zonal  
306 and meridional wind due to long- and short-wave radiation, sub-grid scale convection, condensation and mixing in  
307 the PBL and free troposphere, and gravity wave drag due to orography. The physics parameterizations use the same  
308 input surface boundary conditions and soundings to compute their respective tendencies. Besides GF and MSKF, these  
309 parameterizations are,

- 310 • the Noah land surface parameterization described by Chen and Dudhia (2001),
- 311 • the long- and short-wave Rapid Radiative Transfer Model for GCMs (RRTMG) described by Mlawer et al. (1997)  
312 and Iacono et al. (2000),
- 313 • the semi-empirical parameterization of the cloud fraction of grid-scale clouds from Xu and Randall (1996) and  
314 convective clouds from Xu and Krueger (1991) for use in the long- and short-wave RRTMG schemes. Following  
315 Xu and Randall (1996), the fractional amount of grid-scale clouds is a function of the relative humidity and grid-  
316 averaged condensate mixing ratio of cloud liquid water, ice, and snow. In MSKF, the fractional amount of shallow  
317 and deep convective clouds depends on the convective mass flux.

Deleted: )

Deleted: which

Deleted: length scale is defined as the minimum distance between cell centers

- 322 • the Mellor–Yamada–Nakanishi–Niino (MYNN) Planetary Boundary Layer (PBL) and surface layer scheme  
323 described by Nakanishi and Niino (2009) with many updates described in Olson et al. (2019), and  
324 • the gravity wave-drag parameterization of Hong et al. (2008).

325 The second step calls the dynamical solver which updates the state variables with their respective diabatic  
326 tendencies in conjunction to applying horizontal and vertical advection. Finally, the third step calls the grid-scale cloud  
327 microphysics parameterization so that at the end of the model time step, supersaturation has been entirely removed or  
328 the relative humidity does not exceed 100%. Unlike the physics parameterizations listed for step one, the grid-scale  
329 cloud microphysics scheme updates the potential temperature and moist species for the next time step instead of  
330 providing individual tendencies. The bulk cloud microphysics parameterization of Thompson et al. (THOM; 2004,  
331 2008) is used in all our numerical experiments. THOM includes prognostic equations for temperature, mass mixing  
332 ratio of water vapor, cloud liquid water, rain, cloud ice, snow, and graupel, and number concentration of cloud ice and  
333 rain. We set the number concentration of cloud droplets to  $300 \times 10^6 \text{ m}^{-3}$  over land and  $100 \times 10^6 \text{ m}^{-3}$  over oceans. In  
334 RRTMG, we diagnose the radiative effective radii of cloud liquid water, cloud ice, and snow as functions of the  
335 THOM cloud particle assumptions to add coupling between the cloud microphysics and cloud optical properties, as  
336 discussed in Thompson et al. (2016).

337 To compare the two convective parameterizations against satellite-derived data at hydrostatic scales, we use a  
338 quasi-uniform resolution mesh for which the mean distance between cell centers is 30 km, corresponding to 655,362  
339 cells. The vertical scale includes 55 layers with monotonically increasing thicknesses varying from 50 meters next to  
340 the surface to 700 meters below 10 km to 1000 meters below the model top over ocean cells. The model top is set at  
341 30 km. The dynamics and physics time steps are both set to 150 s, and the horizontal diffusion length scale is set to  
342 30 km. Long- and short-wave radiation is called every 15 mins and THOM is cycled twice so that the cloud  
343 microphysics time-step is less than 90 s to ensure computational stability (Thompson, private communication). With  
344 each convection scheme, we have performed a one-month long experiment preceded by a two-day spin-up to simulate  
345 Northern Hemisphere early winter, initializing our experiments with ERA-Interim (Dee et al., 2011) reanalyses for  
346 0000 UTC 29 November 2015. ERA-Interim sea surface temperatures and sea ice fractions are used to update ocean  
347 cells daily. We refer to our quasi-uniform resolution experiments run with GF and MSKF as GFu and MSKFu,  
348 respectively.

### 349 3.2 Sensitivity experiments

350 Using a variable-resolution mesh spanning between 50 km and 3 km in MPAS, Fowler et al. (2016) demonstrate  
351 that subgrid-scale convection parameterized with GF weakens and grid-scale cloud microphysics parameterized with  
352 WSM6 (Hong and Lim, 2006) strengthens as resolution increases from the coarse to most refined area of the mesh.  
353 Over the most refined area, grid-scale precipitation contributes a major part to total precipitation, and vertical profiles  
354 of subgrid-scale convective heating and drying resemble those obtained with a precipitating shallow convection  
355 scheme. Fowler et al. (2016) suggest investigating the effect of variable resolution on cloud macrophysical properties  
356 and TOA radiation, as grid-scale cloud microphysics parameterizations provide a more physically-based description  
357 of condensation and precipitation over the refined area of the mesh, compared to simpler entraining-detraining cloud

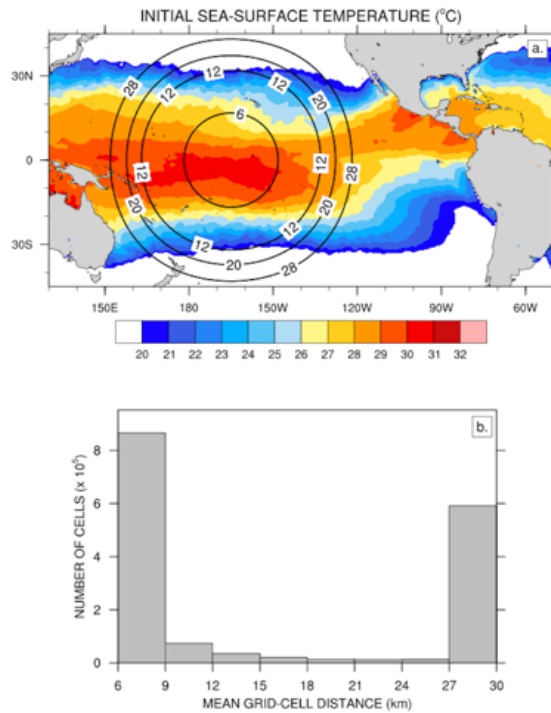
Deleted:

Deleted: later

Deleted: shift from being

361 models used in parameterized convection schemes. With the aim to quantify changes in cloud properties and radiation  
 362 across scales using GF and MSKF, we repeat the early winter experiments but with a variable-resolution mesh that  
 363 spans between 30 km and 6 km and includes 1,622,018 cells. As shown in Fig. 2.a, we centered the refined area of the  
 364 mesh over the Pacific warm pool which we defined as the area in the Western Pacific Ocean where sea-surface  
 365 temperatures (SSTs) exceed 28.5°C, or between 170°E and 140°W. East of 140°W, the north-south width of warmest  
 366 SSTs across the transition zone between the refined and coarse mesh narrows to delineate the location of the ITCZ in  
 367 the Tropical Eastern Pacific. West of 170°E, the end of mesh refinement borders the eastern tip of Papua New Guinea.  
 368 Along the Equator, the transition zone between nonhydrostatic and hydrostatic scales spans 20° in the meridional  
 369 direction on either side of the most refined area of the mesh. Figure 2.b displays a histogram of the mean

**Deleted:** rather simply in the GF convective cloud model to being described in detail in WSM6



370 **Figure 2:** a) Initial sea-surface temperature and refined variable-resolution mesh depicted using isolines of the mean distance  
 371 between grid-cell centers (km) over the Tropical Pacific Ocean; and b) histogram of the number of cells as a function of the mean  
 372 distance between grid-cell centers.  
 373

**Formatted:** Font: Bold

374 distance between cell centers. Differences between the initialization of the variable- versus quasi uniform-  
 375 resolution experiments include a reduced time-step from 150 s to 30 s and a reduced horizontal diffusion length scale  
 376 from 30 km to 6 km. Also, THOM is called only once per time-step. We refer to our variable-resolution experiments  
 377 run with GF and MSKF as GFv and MSKFv, respectively. Differences between GFu, GFv, MSKFu, and MSKFv are  
 378 listed in Table 1.

	GFu	MSKFu	GFv	MSKFv
No. of cells	655,362	655,362	1,622,018	1,622,018
Min. cell distance (km)	22.8	22.8	4.4	4.4
Max. cell distance (km)	31.8	31.8	37.8	37.8
Time step (s)	150	150	30	30
<u>Minimum diffusion</u> length scale (km)	30	30	6	6
CP	GF	MSKF	GF	MSKF

382 **Table 1:** Horizontal mesh resolution, minimum and maximum distance between grid-cell centers, time-step, horizontal diffusion  
383 length scale, and convective parameterization (CP) for numerical experiments with the quasi uniform- and variable-resolution  
384 meshes.

### 385 3.3 Satellite data sets

386 We compare the cloud liquid water path (LWP) and ice water path (IWP), cloud area fraction (CF), and the top-  
387 of-the-atmosphere longwave upward (TOALW) and shortwave net (TOASW) radiation simulated in our numerical  
388 experiments against the Edition-4 Single Scanner Footprint (SSF) products from the Clouds and the Earth's Radiant  
389 Energy System (CERES; Wielicki et al., 1996). Minnis et al. (2011) describe in great details the retrieval of  
390 simultaneous and collocated radiation fluxes and cloud properties from the CERES radiometers and the Moderate-  
391 resolution Imaging Spectroradiometer (MODIS) using consistent algorithms and calibration across satellite platforms,  
392 and shared auxiliary input (temperature and humidity profiles). SSF data are available in two different formats. The  
393 first data file format contains one hour of radiation fluxes and cloud properties at the instantaneous CERES 20 km  
394 footprint level from the sun-synchronous afternoon (morning) equatorial crossing time Aqua (Terra) satellites. As  
395 illustrated in Minnis et al. (2011; their Fig. 15), the CF in each SSF is given in terms of a clear fraction, a fraction for  
396 an upper and lower cloud layer separately, and a fraction for an upper layer over a lower layer, although the overlap  
397 CF is not available and set to zero in the Edition 4 release version that we are using. The LWP, IWP, and all other  
398 cloud fields are provided for the lower and upper layers, separately. Figure 3 illustrates two orbits of the Aqua satellite,  
399 one between 00 GMT and 01 GMT, and one between 14 GMT and 15 GMT, showing the TOALW (top panel) and  
400 CF (bottom panel), after gridding the hourly orbital data to a  $0.2^\circ \times 0.2^\circ$  latitude-longitude grid. Gridded radiation fluxes  
401 and cloud data are means over all SSF data contained inside each rectangular grid, after applying a linear interpolation  
402 to reduce the number of missing values. Missing values, highlighted in gray in all figures, depict rectangular grids that  
403 did not contain radiation and cloud data in any of the SSF inside the  $0.2^\circ \times 0.2^\circ$  grid. As seen in Fig. 3, our gridding of  
404 the orbital data removes most of the missing data along each orbit, providing a clear depiction of the relationship  
405 between the TOALW and CF for cloudy and cloud-free grid cells. Areas of high (low) TOALW coincide with areas  
406 of small (large) cloudy areas, but it is also interesting to note that areas of each orbit are characterized as overcast in  
407 conjunction with areas that are not as spatially uniform in TOALW as in CF.

Formatted Table

Formatted: Left

Formatted: Left

Formatted: Left

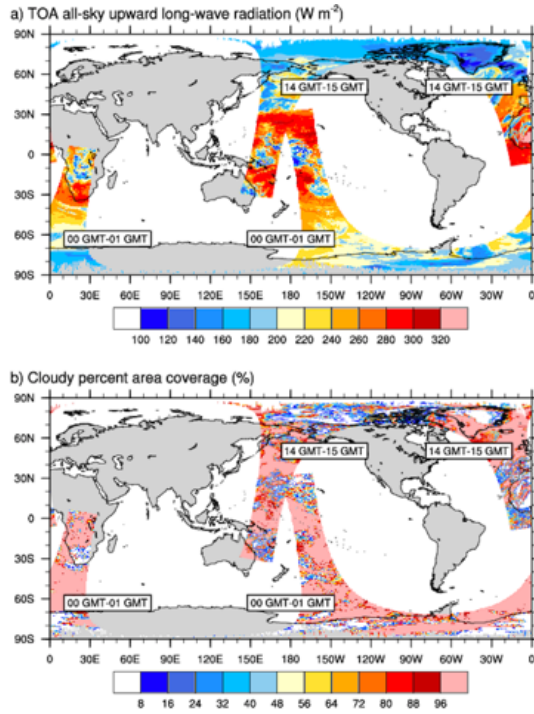
Deleted: Diffusion

Formatted: Left

Formatted: Left

Formatted: Space Before: 0 pt, After: 0 pt



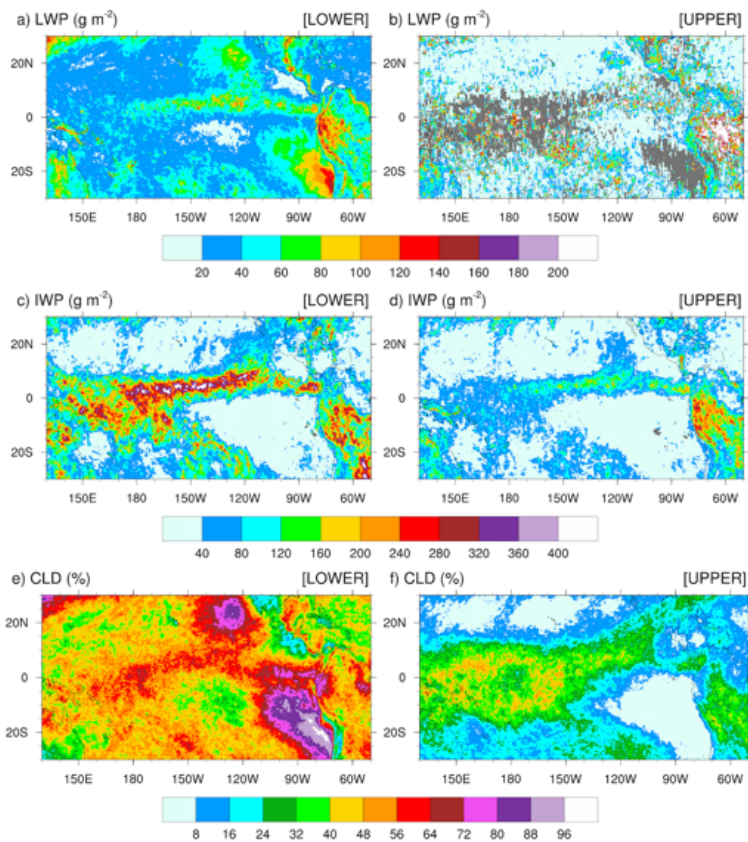


409  
 410 **Figure 3:** Orbital paths of the Aqua satellite between 00 GMT-01 GMT and 14 GMT-15 GMT after binning the SSF data onto a  
 411 0.2°x0.2° rectangular grid for a) the TOA all-sky upward long-wave radiation, and b) the cloudy percent area coverage for 1<sup>st</sup>  
 412 December 2015.

413 The second data file format (SSF1deg) includes daily and monthly averages of the original SSF orbital data but  
 414 interpolated on a 1°x1° latitude-longitude grid. The difficulty in using hourly higher-resolution orbital data instead of  
 415 monthly mean lower-resolution 1°x1° latitude-longitude gridded product is that the former are available in two distinct  
 416 *dynamic* layers while the latter is provided at fixed pressure levels and for the atmospheric column. The lower and  
 417 upper layers are referred to as *dynamic* layers because the cloud-top (base) pressure of each layer varies between SSFs  
 418 along each orbit. The advantage of using orbital hourly data is that they can be gridded and interpolated to a spatial  
 419 resolution close to that of our uniform and variable-resolution numerical experiments prior to computing monthly  
 420 mean radiation and cloud fields. We choose the 0.2°x0.2° latitude-longitude gridded hourly data derived from the first  
 421 data file format through the entire manuscript.

422 In order to best compare the simulated against satellite-derived LWP and IWP, we need to understand the  
 423 partitioning of the SSF LWP and IWP between the two cloud layers. In brief, a lower and an upper cloud layer can be  
 424 detected simultaneously if they lie adjacent to each other inside an SSF. In that case, the cloud properties for each  
 425 layer are reported separately. In the case when an opaque upper cloud layer is detected to be above a lower cloud  
 426 layer, it is impossible to identify the two layers separately. Then, only one cloud layer is reported and always classified

427 as the lower cloud layer, regardless of its cloud-base (top) pressure (Loeb, private communication). Further details on  
428 the cloud classification, including determination of the cloud phase, are found in Geier et al. (2003) and Minnis et al.  
429 (2011). Figure 4 shows the monthly-mean LWP, IWP, and CF for the lower (left panels) and upper (right panels) layer  
430 measured by Aqua for December 2015 over the Tropical Pacific Ocean. Figure S1 is as Fig. 4, but for the Terra satellite  
431 (see supplemental figures). LWP and IWP are *in-cloud* values meaning that they have not been weighted by CF. The  
432 lower cloud layer includes stratiform clouds that form over colder sea-surface temperatures along the coast of Peru  
433 and off the Baja Peninsula. Over these areas of CF greater than 72% for the lower cloudy layer, CF for the upper cloud  
434 layer is less than 8%, highlighting that a single layer of low-level clouds fills a major fraction of the SSF. Increased  
435 values of CF are seen in conjunction with increased (decreased) values for the LWP (IWP) in the lower cloud layer  
436 indicative of warm-phase clouds, as well seen as off the coast of Peru. High values for the CF and IWP juxtaposed  
437 with lower values for the LWP in the lower cloud layer depict clearly deep convection over the Eastern Pacific Ocean,  
438 ITCZ, and warm pool region. Over areas of deep convection, upper cloud layers are often detected in conjunction with  
439 lower cloud layers within the same SSF but are defined by decreased values for the CF and IWP. For the LWP, the  
440 coexistence of a lower and upper cloud layer is quite infrequent, as seen by the number of missing grid-points in Fig.  
441 4.b (S1.b). Where detected, the LWP in the upper layer exceeds that in the lower layer, indicative of warm-phase  
442 mature thicker cumulus clouds coexisting with developing thinner cumulus clouds in the lower layer. Finally, outside  
443 of the typical stratus cloud regions and either sides of the ITCZ and warm pool region, SSF data reveal extended  
444 regions of warm-phase thinner clouds characteristic of widespread shallow convection over tropical oceans.



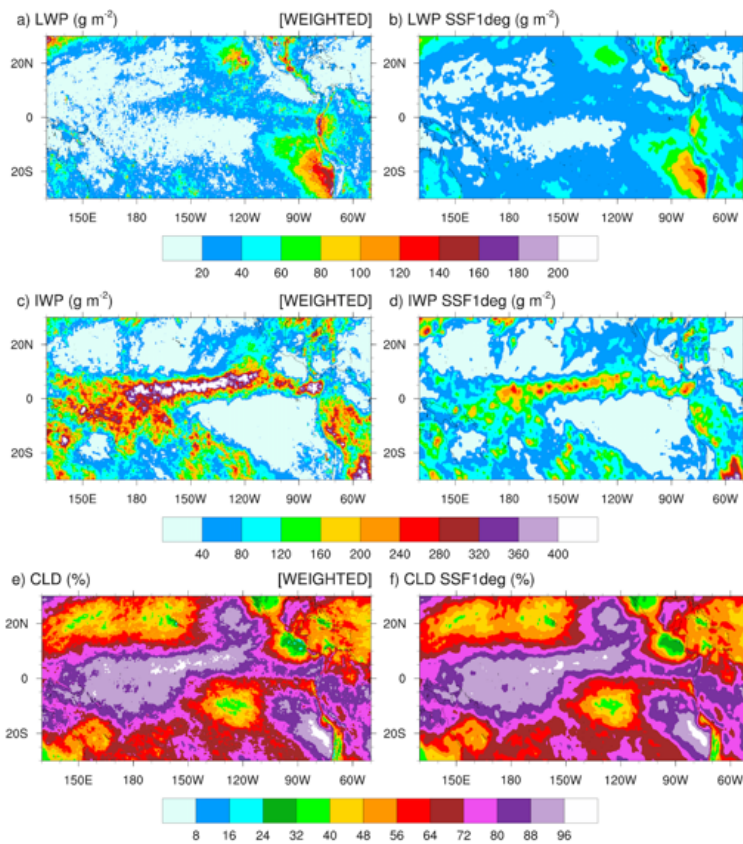
445  
 446 **Figure 4:** Monthly-mean cloud liquid water path (LWP, top panels), cloud ice water path (IWP, middle panels), and cloud fraction  
 447 (CLD, bottom panels) over the Tropical Pacific Ocean for December 2015 from the Aqua satellite. Panels a), c), and e) are for the  
 448 lower cloud layer; panels b), d), and f) are for the upper cloud layer.

Formatted: Font: Bold

449 Calculating the satellite-retrieved LWP and IWP in an atmospheric column for validation of those from our  
 450 numerical simulations is a two-step process. Because simulated LWPs and IWPs are *gridcell mean* values and not  
 451 *local* values, we first multiply the SSF LWP and IWP by CF to get their mean values in the lower and upper cloud  
 452 layers separately, prior to gridding the hourly orbital data. Second, because the lower and upper layers are defined as  
 453 adjacent to each other and never overlap in a SSF, we simply add the gridcell mean LWP and IWP in the lower layer  
 454 to that in the upper layer to compute the total LWP and IWP. Our processing method is simpler than the processing  
 455 steps taken by the CERES Science Team to spatially grid and temporally average SSF hourly orbital data to SSF1deg  
 456 gridded monthly mean data. Figure 5 compares the monthly-mean 0.2°x0.2° latitude-longitude CF-weighted LWP  
 457 and IWP and CF (left panels) against the SSF1deg products (right panels) for December 2015 over the Tropical Pacific  
 458 Ocean. The top panels of Fig. 5 show that our method reproduces successfully the geographical patterns and magnitude

459 of the LWP over the Tropical Pacific when compared against the SSF1deg data for both months. In contrast, because  
 460 our method does not weigh the IWP as a function of height, it systematically overestimates the SSF IWP when  
 461 compared against the SSF1deg data, as seen over the ITCZ and South Pacific Convergence Zone (SPCZ) in both  
 462 months.

463



464 **Figure 5:** Monthly-mean cloudy area-weighted cloud liquid water path (LWP, top panels), cloudy-area weighted cloud ice water  
 465 path (IWP, middle panels), and cloud fraction (CLD, bottom panels) over the Tropical Pacific Ocean for December 2015. Panels  
 466 a), c), and e) are SSF data; panels b), d), and f) are SSF1deg climatological data.

468 Using ice water content data from the ascending (daytime) and descending (nighttime) portion of CloudSat orbits,  
 469 Waliser et al. (2009; Fig. 7) estimate that day-night fluctuations in the ice water content at 215 hPa account for as  
 470 much as 13% (20 %) of the annual mean ice water content over the warm pool (Tropical Eastern Pacific), in response  
 471 to the diurnal cycle of deep convection over the tropical oceans. Therefore, when computing the monthly-mean CF,  
 472 LWP, IWP, TOALW, and TOASW produced with GFu, GFv, MSKFu and MSKFv, we first sample the hourly model

Formatted: Font: Bold

473 diagnostics in accordance with the Aqua and Terra satellite orbits in order to reduce biases from different diurnal  
474 sampling between our experiments and SSF data. Because the MODIS-based retrieval of the LWP and IWP is  
475 insensitive to precipitation, and the rain, snow, and graupel mixing ratios are prognostic variables in THOM and fall  
476 through the atmosphere at finite velocities, we infer that the LWP and IWP must include all precipitating and non-  
477 precipitating condensates.

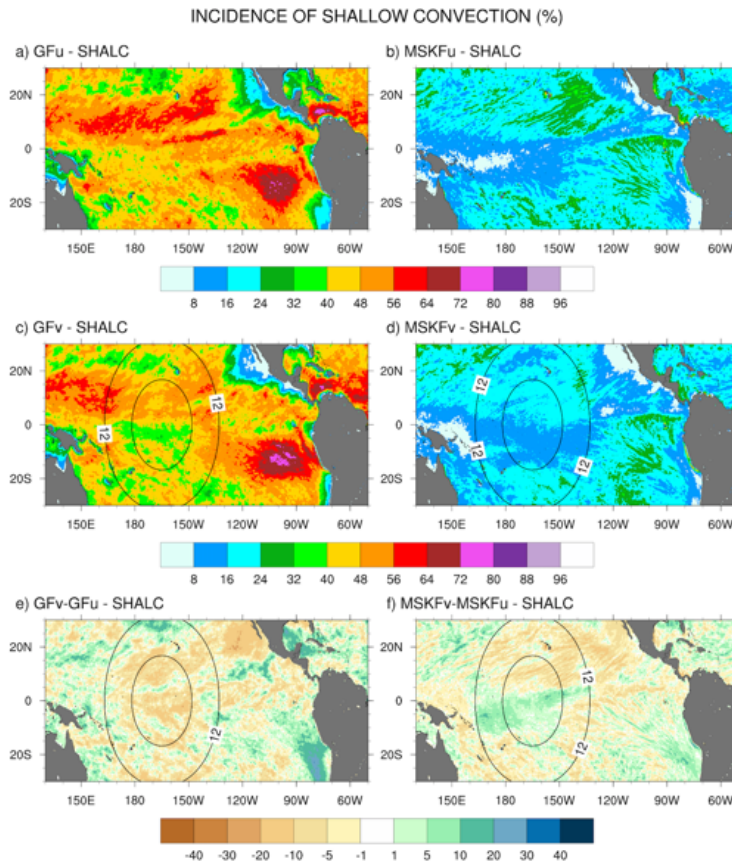
478 In addition to CERES SSF data, we use the monthly-mean precipitation rates from the TRMM Multisatellite  
479 Precipitation Analysis (TMPA Version 7; Huffman et al., 2007) to compare simulated versus observed precipitation  
480 rates, and monthly mean ERA-Interim reanalyses (Dee et al., 2011) to compare simulated versus observed precipitable  
481 water in the lower troposphere.

## 482 **4 Simulated versus satellite-retrieved precipitation**

### 483 **4.1 Incidence of subgrid-scale shallow and deep convection**

484 Differences in the treatment of interactions between shallow and deep convection in GF and MSKF, as described  
485 in Section 2, are bound to modify the partitioning between shallow and deep convection as spatial resolution increases  
486 over the refined area of the mesh. A useful diagnostic to analyze the response of shallow and deep convection to local  
487 mesh refinement is the incidence of convection. Because shallow convection in both GF and MSKF is non-  
488 precipitating, we set the incidence of shallow convection to 100 % when cloud-tops of shallow convective updrafts  
489 are detected, and 0 % otherwise. We set the incidence of deep convection to 100 % when convective precipitation  
490 occurs and 0 % otherwise. Figures 6 and 7 highlight the impact of the horizontal scale dependence of convection on  
491 the monthly-mean incidence of subgrid-scale shallow and deep convection in our uniform- and variable-resolution  
492 experiments for December 2015.

493 Figure 6 shows that simulated shallow convection occurs over the entire Tropical Pacific, and that its incidence  
494 is about twice as large in GFu and GFv as in MSKFu and MSKFv. In GFu and GFv, incidence in excess of 48 %  
495 covers most of the Tropical Pacific, including the ITCZ and warm pool where GF allows shallow and deep convection  
496 to occur simultaneously. GFu and GFv exhibit highest incidence of shallow convection off the coast of Peru where  
497 persistent low-level stratiform clouds are formed. In contrast, the incidence of shallow convection in MSKFu and  
498 MSKFv never exceeds 32 % over the entire domain and is less than 16 % over the ITCZ and warm pool where shallow  
499 and deep convection are not allowed to coexist in MSKF. The bottom panels highlight differences in the incidence of  
500 shallow convection between GFv and GFu, and MSKFv and MSKFu. Despite the fact that GF does not include a  
501 spatial scale dependence in its formulation of shallow convection, GFv produces reduced shallow convection relative  
502 to GFu over most of the Tropical Pacific, except most notably immediately off the coast of Peru. In contrast to GFv,  
503 MSKFv yields increased incidence of shallow convection over most of the warm pool region. In MSKF, the height of  
504 deep convective clouds decreases as horizontal resolution increases. As the classification between deep and shallow  
505 convection is a function of cloud depth, convective clouds originally defined as deep are reclassified as shallow,  
506 leading to increased incidence of shallow convection in the refined area of the mesh.



507  
 508 **Figure 6:** Monthly-mean incidence of shallow convection (SHALC) over the Tropical Pacific Ocean simulated in GFu and MSKFu  
 509 (top panels) and GFv and MSKFv (middle panels), and difference in the incidence of shallow convection between GFv and GFu  
 510 (bottom left panel) and MSKFv and MSKFu (bottom right panel) for December 2015.

**Formatted: Font: Bold**

511 In Fig. 7, the top and middle panels show that, in contrast to shallow convection, the incidence of deep convection  
 512 has the same order of magnitude in GFu and MSKFu, and GFv and MSKFv. The top panels reveal that the incidence  
 513 of deep convection is higher in MSKFu than GFu over the ITCZ and warm pool. In MSKFu, a sharp transition between  
 514 areas of high and low incidence of deep convection causes areas outside of the ITCZ and warm pool to be mostly void  
 515 of deep convection, as seen between 10°N and 30°N. In GFu, the incidence of deep convection is decreased over the  
 516 warm pool relative to the ITCZ west of 160°W. Outside of the ITCZ and warm pool, GFu and GFv lead to higher  
 517 incidence of deep convection than MSKFu and MSKFv because, in contrast to MSKF, GF allows deep and shallow  
 518 convection to coexist in the same grid-cell. Middle panels highlight decreased incidence of subgrid-scale deep  
 519 convection inside the refined area of the mesh over the warm pool in both GFv and MSKFv, as we expect clouds to

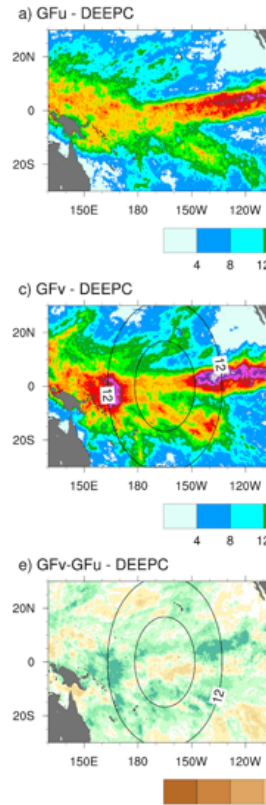
520 be resolved on the higher resolution grid, in conjunction with increased incidence east and west of the refined area.  
 521 The decreased incidence in the refined area is more pronounced between MSKFu and MSKFv than between GFu and  
 522 GFv whereas the upscaling impact of spatial refinement outside the refined area is greater in GFv than MSKFv. The  
 523 scale-aware formulation in GF does not produce the same contrast between the refined and coarse mesh in GFv and  
 524 GFu as that in MSKF in MSKFv and MSKFu. Fig. 7.f reveals a reduced incidence in excess of 25 % between MSKFu  
 525 and MSKFv starting at resolutions higher than 12 km flanked by increased incidence of deep convection east and west  
 526 of the refined area. In contrast, Fig. 7.e displays a longitudinal band of decreased incidence of deep convection between  
 527 90°W and the dateline, bordered by increased deep convection north of the equator and south of 10°S. Table 2 lists  
 528 the area-averaged incidence of deep and shallow convection for an area inside the refined mesh (REFINED: 0.1°N to  
 529 5.1°N; 150°W to 180°W) and an area over the Tropical Eastern Pacific (EAST: 3.1°N to 8.1°N; 90°W to 120°W), as  
 530 later shown in Figure 9.a. The REFINED and EAST areas display little variation in the incidence of shallow  
 531 convection between GFu (MSKFu) and GFv (MSKFv), but the incidence of shallow convection in GFu and GFv is  
 532 much higher than in MSKFu and MSKFv. The incidence of subgrid-scale deep convection is higher in the EAST area  
 533 compared to the REFINED area in all four experiments. Over the REFINED area, the incidence of subgrid-scale deep  
 534 convection remains about the same between GFu and GFv but strongly decreases between MSKFu and MSKFv.

	DEEP CONVECTION (%)		SHALLOW CONVECTION (%)	
	REFINED	EAST	REFINED	EAST
GFu	20	30	52	52
GFv	23	36	47	48
MSKFu	27	33	14	17
MSKFv	10	36	17	15

536 Table 2: Area-averaged incidence of deep and shallow convection. The REFINED and EAST areas are shown in Figure 9.a.

537 As described in Section 2, MSKF differentiates shallow from deep convection as a function of the convective  
 538 cloud depth. As spatial resolution increases, the scale aware formulation leads to a reduction in the intensity of  
 539 convection and depth of convective clouds, mostly deep convection, over the refined area as seen in Fig. 7.f. As the  
 540 depth of convective clouds originally classified as precipitating deep convective clouds become shallower, MSKF  
 541 reclassifies those same clouds as nonprecipitating shallow clouds, leading to near-equal compensation between the  
 542 decreased and increased incidence of deep and shallow convection over the warm pool. In contrast to MSKF, GF  
 543 causes precipitating deep convection to become precipitating shallow convection at increased spatial resolution. As  
 544 this process occurs in the deep convection scheme and both cloud types precipitate, variations in the incidence of deep  
 545 convection between GFu and GFv are small. Further analysis of the response of shallow convection between GFu and  
 546 GFv over the refined area is beyond the objectives of this research.

Deleted: over...or an area located ...inside the refined mesh (REFINED: 0.1°N to 5.1°N; 150°W to 180°W) and an area over the Tropical Eastern Pacific (EAST: 3.1°N to 8.1°N; 90°W to 120°W)[1]



Moved down [1]:  
 Figure 7: As Fig. 6, but for the monthly-mean incidence of deep convection (DEEPC).

Deleted: ...6, but for the monthly-mean incidence of deep convection (DEEPC).  
 Table 2 summarizes our results displayed... as later shown in Figs. 6 and 7.... REF\_Ref8663567 Figure 9.a. The REFINED and EAST areas display little variation in the incidence of shallow convection between GFu (MSKFu) and GFv (MSKFv), but the incidence of shallow convection in any of the experiments. The incidence of shallow convection in ...Fu and GFv is much higher than in MSKF[2]

Formatted Table

Formatted: Space Before: 0 pt, After: 0 pt

Deleted: Units are %.

Formatted: Font: Bold

Formatted: Tab stops: Not at 1.69"

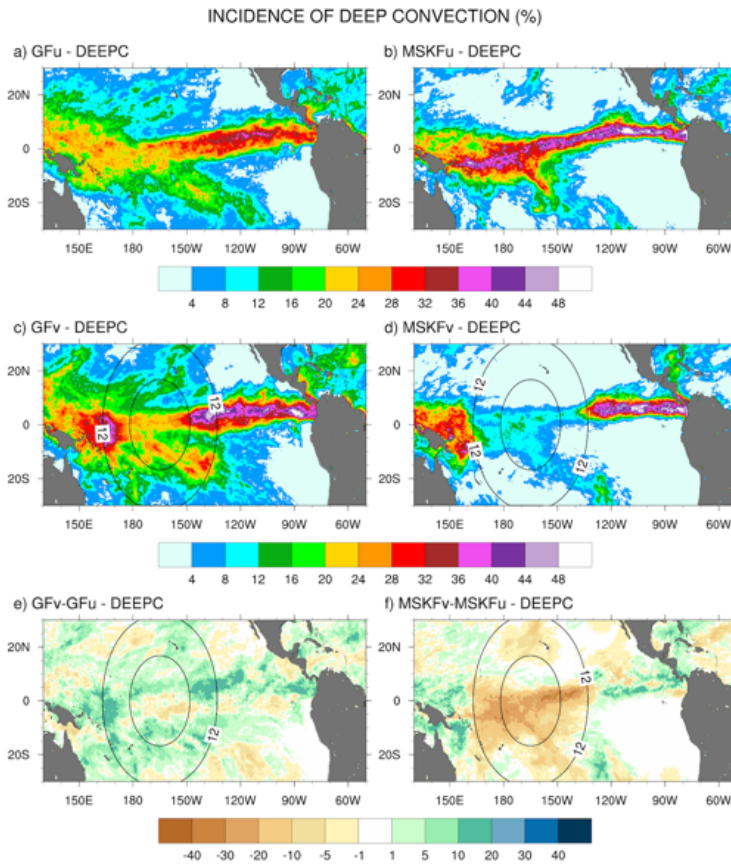


Figure 7: As Fig. 6, but for the monthly-mean incidence of deep convection (DEEPC).

#### 4.2 Precipitation rates

Figure 8 shows the monthly-mean convective precipitation rate simulated in GFu and MSKFu (top panels), and GFv and MSKFv (middle panels). The bottom panels in Figure 8 display the ratio between the convective precipitation rate simulated in GFv (MSKFv) and GFu (MSKFu) to contrast the impact of the scale aware formulation in GF and MSKF. The top panels highlight similar geographical patterns of convective precipitation in GFu and MSKFu. Between 80°W and 160°W, increased convective precipitation is located along the ITCZ, in conjunction with increased incidence of deep convection, as seen in Figs. 7.a,b. West of 160°W, GFu leads to decreased but more widespread convective precipitation relative to MSKFu over the warm pool, in conjunction with decreased but more widespread incidence of convection. In GF, this result infers that while deep convection is not triggered as often over the warm pool as along the ITCZ, the amount of convective precipitation produced in one time-step is higher over the

Moved (insertion) [1]

Formatted: Font: Bold

Deleted: Figures

Deleted: and 9 show

Deleted: and grid-scale

Deleted: rates

Deleted: )

Deleted: )

Deleted: and grid-scale

Deleted: rates

Deleted: and grid-scale

Deleted: rates are

Deleted: over

Deleted: Fig

Deleted: ,

Deleted: contrast to convective precipitation, there are few differences in grid-scale precipitation between GFu and MSKFu (Figs. 9.a,b). This

Deleted: over



621 warm pool than along the ITCZ, so that monthly-mean convective precipitation rates remain about the same in both  
622 regions. In Fig. 8, and in agreement with the middle panels of Fig. 7, middle panels display a strong decrease in  
623 convective precipitation in both GFv and MSKFv over the refined area of the mesh. In MSKFv, the strong reduction  
624 in convective precipitation occurs, not only over the most refined area of the mesh, but also where horizontal grid-  
625 spacing increases from 6 to 12 km. Convective precipitation increases sharply as soon as grid-spacing is greater than  
626 12 km. In GFv, the monthly-mean convective precipitation rate is higher than that in MSKFv over the most refined  
627 area of the mesh but starts to increase more rapidly between 6 and 12 km than in MSKFv. Differences in increasing  
628 convective precipitation across the transition zone between the refined and coarse areas reflect different impacts of  
629 the scale-aware formulation in GF and MSKF. In order to start understanding the strong increase in convective  
630 precipitation across the transition zones in GFv, we run GFu with the 30s time step used in GFv to quantify the  
631 dependence of a shorter time-step on a coarser resolution mesh with GF. As seen in Fig. S2.a, reducing the time step  
632 from 150s to 30s yields increased convective precipitation over all the convectively active areas of the Tropical Pacific  
633 Ocean. Differences in convective precipitation (Fig. S2.b) display maxima over the Tropical Eastern Pacific (east of  
634 110°W) and east of Papua New Guinea (east of 160°E), and superimpose relatively well with maxima display in GFv  
635 east and west of the refined area of the mesh seen in Fig. 8.c. This result implies that some of the closures used in GF  
636 are sensitive to the model time step. Further research is needed to investigate how the troposphere in GFv becomes  
637 more unstable than MSKFv between the refined and coarse area of the mesh. The bottom panels in Figure 8 show that  
638 the ratio in convective precipitation between GFv and GFu has the same order of magnitude as that between MSKFv  
639 and MSKFu over the refined area of the mesh. While it remains as small in the transition zone as in the refined mesh  
640 with MSKF, this ratio increases to values greater than 1 between 6 and 12 km with GF, indicating increased convective  
641 precipitation on each side of the refined area in GFv relative to GFu, as also seen in Figure 8.c. Maps of monthly-  
642 mean grid-scale precipitation rate would show similar geographical patterns of grid-scale precipitation between GFu  
643 and MSKFu. Over the refined area, increased grid-scale precipitation compensates decreased convective precipitation  
644 in GFv and MSKFv. Over the coarse area, grid-scale precipitation is strongly decreased along the ITCZ and warm  
645 pool in GFv while remaining nearly the same in MSKFv (not shown for brevity).

**Deleted:** over

**Deleted:** This result may also explain the decrease in grid-scale precipitation over the warm pool compared to the ITCZ, as increased convective drying inhibits grid-scale cloud microphysics processes and precipitation in the lower troposphere.

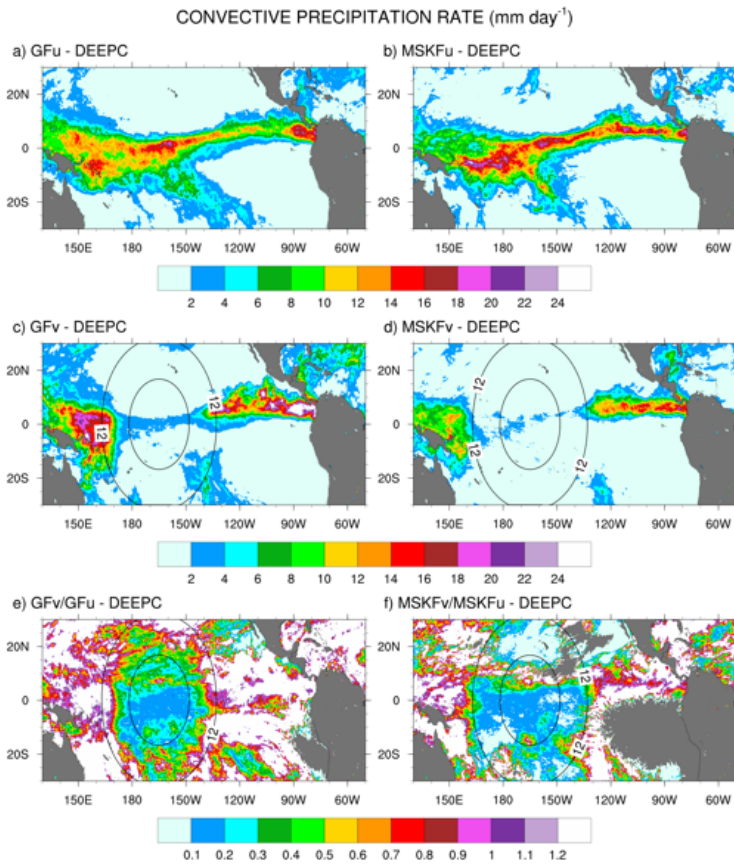
**Deleted:** , bottom panels show that the scale-aware formulation in MSKF reduces convective precipitation more efficiently than GF, leading to precipitation rates that are systematically smaller in MSKFv than GFv in the refined area. The upscaling effect of spatial refinement produces different convective precipitation patterns between MSKFv and GFv over the coarse area of the mesh. In GFv, increased incidence of deep convection on each side of the refined area leads to increased convective precipitation and strongly decreased grid-scale precipitation in the warm pool and Tropical Eastern Pacific, as seen in Figs.

**Deleted:** .c and 9.c. In contrast to GFv, MSKFv yields similar convective (grid-scale) precipitation as MSKFu over those two areas, when comparing Fig. 8.b to Fig 8.d (Fig. 9.b to

**Moved down [2]:** Fig.

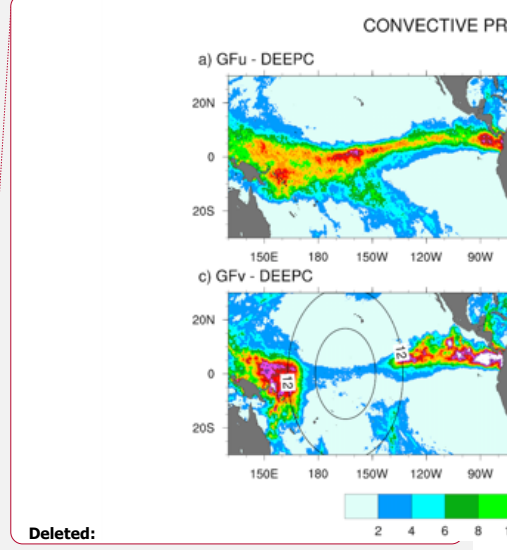
**Formatted:** Font color: Auto

**Deleted:** 9.d). Over the refined area, grid-scale precipitation increases to compensate for the decrease in convective precipitation in GFv and MSKFv so that total precipitation remains about the same between GFu (MSKFu) and GFv (MSKFv). Comparing Fig. 9.c (Fig. 9.d) against Fig. 9.a (Fig. 9.b) reveals that grid-scale precipitation increases the most along the ITCZ in conjunction with the greatest decrease in convective precipitation. GFv and MSKFv also lead to an increase in grid-scale precipitation over the SPCZ, more so in MSKFv than GFv. MSKFv does not produce as drastic a reduction in grid-scale precipitation as GFv over the coarse area of the mesh, indicating a smaller upscaling impact of the refined mesh in MSKFv than GFv.

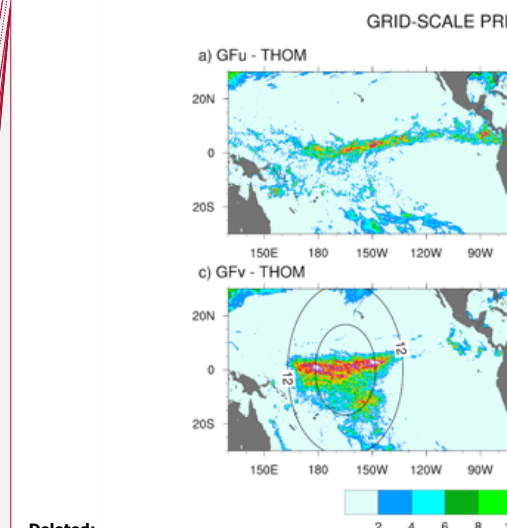


677  
 678 **Figure 8:** Monthly-mean convective (DEEPC) precipitation rate over the Tropical Pacific Ocean simulated in GfU and MSKFu  
 679 (top panels), GfV and MSKFv (middle panels), and ratio between the monthly-mean convective precipitation rate in GfV (MSKFv)  
 680 and GfU (MSKFu) for December 2015.

681 The simulated total precipitation rate can be compared to observed TMPA precipitation using Figs. 9 and 10  
 682 which show the precipitation rates and differences between simulated and observed precipitation rates, respectively.  
 683 Areas of maximum satellite-retrieved precipitation are found over the ITCZ between 130°W and the dateline (Fig.  
 684 9.a). Observed precipitation decreases over the warm pool west of the dateline and decreases strongly over the Tropical  
 685 Eastern Pacific (between 80°W and 120°W) and the SPCZ. The four simulations overestimate precipitation in the  
 686 Tropical Eastern Pacific between 80°W and 120°W (Figs. 9.b-e) with biases in excess of 11 mm day<sup>-1</sup> (Figs. 10.a-d).  
 687 The four simulations also overestimate precipitation between 130°E and 160°E, or west of the refined area, with biases  
 688 about as large as those seen east of the refined area, except for MSKFu. The uniform-grid results (Figs. 9.b-c) display  
 689 the highest precipitation rates over the area of warmest SSTs where we expect deepest convection to occur and are in

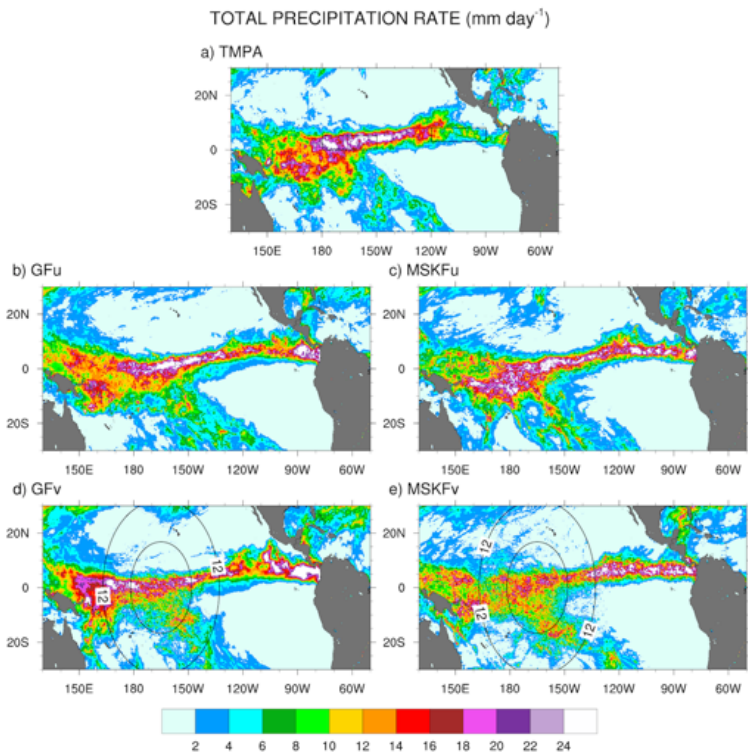


Deleted:  
 Deleted: ) and ..., GfV and MSKFv (bottom ... [3]  
 Formatted: Font: Bold



Deleted:  
 Figure 9: As Fig. 8, but the monthly mean grid-scale (THOM) precipitation rate.  
 The simulated total precipitation rate can be evaluated... compared to observed TMPA precipitation using Figs. 9 and 10 which show the precipitation rates and differences between simulated and observed precipitation rates, respectively. Areas of maximum... [4]

729 reasonable agreement with TMPA data. However, GFu and MSKFu locate the ITCZ south of its observed location  
 730 (Figs. 10.a-b), producing a positive bias straddling the Equator and a negative bias north of the Equator. The scale-  
 731 aware dependence of deep convection in GF leads to decreased total precipitation in GFv compared to GFu over the  
 732 entire refined area (Fig. 10.e). In contrast, Fig. 10.f shows that while the scale-aware dependence in MSKF leads to  
 733 decreased precipitation in MSKFv over a major fraction of the refined area, it also leads to an improved location of  
 734 the simulated ITCZ, as evidenced by increased precipitation north of the Equator.



735 **Figure 9:** Monthly-mean total precipitation rate over the Tropical Pacific Ocean from TMPA data (top panel) and simulated with  
 736 GFu and MSKFu (middle panels) and GFv and MSKFv (bottom panels) for December 2015.

738 Table 3 summarizes the area-mean monthly-mean convective, grid-scale, and total simulated and observed TMPA  
 739 precipitation rates over the REFINED and EAST areas. Over the two areas, the simulated total precipitation is about  
 740 the same for all four experiments, but is underestimated (overestimated) relative to TMPA data, over the REFINED  
 741 (EAST) areas, respectively. Over the REFINED area, total precipitation decreases by 2.1 mm day<sup>-1</sup> between GFu and  
 742 GFv and 2.3 mm day<sup>-1</sup> between MSKFu and MSKFv, highlighting a near-equal compensation between decreased deep  
 743 convective and increased grid-scale precipitation over the most refined area of the mesh. Over the EAST area, total  
 744 precipitation increases by 2.7 mm day<sup>-1</sup> between GFu and GFv resulting from a 5.3 (2.6) mm day<sup>-1</sup> increase (decrease)

Deleted: Fig

Deleted: ,

Formatted: Font: Bold

Deleted: REFINED area

Deleted: in

Deleted: ,

Deleted: less than that from

Deleted: , This bias results because the simulated ITCZ is located south of that actually observed (see Fig. 11). Total precipitation is reduced

Deleted: (2.3)

Deleted: (MSKFu)

Deleted: (

Deleted: ),

Deleted: rates as horizontal resolution increases. GFu and MSKFu, and GFv and MSKFv, have similar partitioning between convective and grid-scale precipitation rates. Table 3 quantifies the increased (decreased) convective (grid-scale) precipitation between GFu and GFv observed outside of

Deleted: in Fig. 6. For

Deleted: Table 3 shows that

Deleted: (1.2)

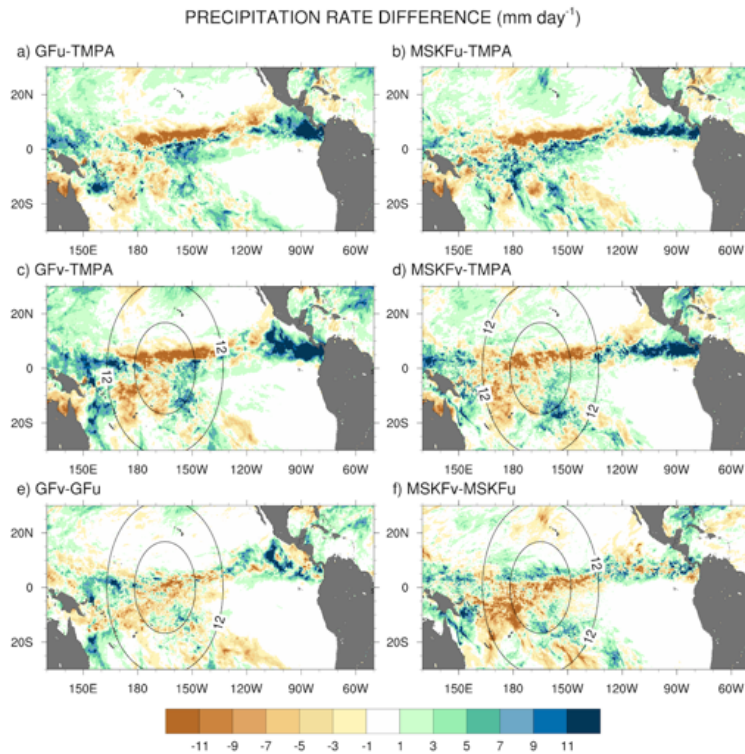
Deleted: in conjunction with

Deleted: 0.5

768 in convective (grid-scale) precipitation. In contrast, total precipitation increases by 1.2 mm day<sup>-1</sup> between MSKFu and  
 769 MSKFv resulting from a 0.5 (0.6) mm day<sup>-1</sup> increase in convective (grid-scale) precipitation. The large (small) increase  
 770 in convective precipitation in GFv (MSKFv) over the coarse areas east (and west) of the refined area highlights distinct  
 771 upscaling effect of the refined area on the coarse area of the mesh between GFv and MSKFv.

Deleted: between GFu and GFv (MSKFu and MSKFv), highlighting the impact

Deleted: in



772 **Figure 10:** Monthly-mean precipitation rate difference over the Tropical Pacific Ocean between GFu (MSKFu) and TMPA data  
 773 (top panels), GFv (MSKFv) and TMPA data (middle panels), and between GFv (MSKFv) and GFu (MSKFu) (bottom panels) for  
 774 December 2015.  
 775

776 In summary, the scale dependence of convection in GF and MSKF produces the same partitioning between  
 777 convective and grid-scale precipitation inside the refined area or decreased convective and compensating increased  
 778 grid-scale precipitation as horizontal resolution increases. The upscaling impact on convective and grid-scale  
 779 precipitation varies between GF and MSKF. As seen in Fig. 8 and Table 3, convective precipitation increases strongly  
 780 over the warm pool and Eastern Pacific starting across the transition zones east and west of the refined area in GFv.  
 781 In contrast, while the parameterization of the scale dependence of deep convection in MSKF produces a stronger  
 782 decrease in convective precipitation in MSKFv than GFv, it produces a smoother transition in convective precipitation  
 783 and decreased upscaling effect as spatial resolution reaches 30 km.

	CONVECTIVE ( $\text{mm day}^{-1}$ )		GRID-SCALE ( $\text{mm day}^{-1}$ )		TOTAL ( $\text{mm day}^{-1}$ )	
	REFINED	EAST	REFINED	EAST	REFINED	EAST
GFu	10.0	8.7	6.1	3.7	16.1	12.4
GFv	1.9	14.0	12.1	1.1	14.0	15.1
MSKFu	10.9	10.6	4.9	4.8	15.8	15.5
MSKFv	1.7	11.1	11.8	5.4	13.5	16.5
TMPA					20.7	7.3

788 **Table 3:** Area-averaged convective, grid-scale, and total precipitation rates over the same areas as those described for Table 2. The  
789 REFINED and EAST areas are shown in Figure 9.a.

Deleted: 76

Deleted: 3

Deleted: Units are  $\text{mm day}^{-1}$ 

Formatted: Space Before: 0 pt, After: 0 pt

## 790 5 Simulated relative humidity and simulated versus satellite-retrieved LWP and IWP

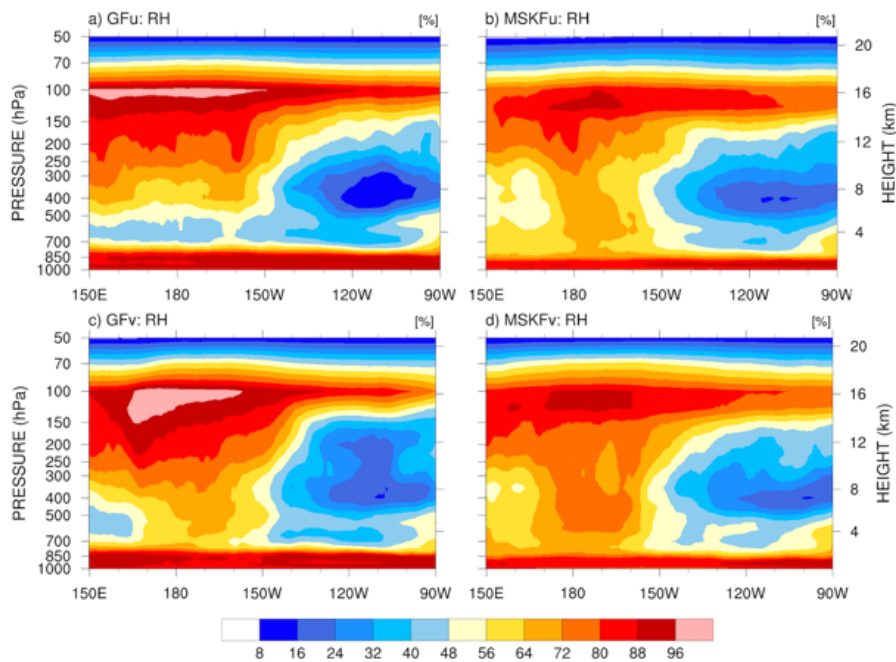
### 791 5.1 Relative humidity

792 One effect of local mesh refinement is the decreased contribution of parameterized convection compensated by  
793 increased contribution of grid-scale cloud microphysics to condensation processes and cloud formation with  
794 increasing spatial resolution. Therefore, prior to comparing the simulated LWP and IWP against SSF data, we first  
795 investigate differences in relative humidity (RH) between our uniform- and variable-resolution experiments. Figure  
796 11 displays the monthly-mean longitude-pressure cross sections of RH latitudinally-averaged between  $5^{\circ}\text{S}$  and  $5^{\circ}\text{N}$ .  
797 East of  $150^{\circ}\text{W}$  over the Tropical Eastern Pacific, the four experiments display similar vertical distributions of RH,  
798 with relatively lower RH between 700 hPa and 150 hPa and higher RH in the PBL below 700 hPa and in the upper-  
799 troposphere above 150 hPa. All four experiments show significant increase in RH west of  $150^{\circ}\text{W}$  across the entire  
800 troposphere, over the warm pool where the warmest SSTs are seen (Fig. 2.a) and deepest convective updrafts are  
801 formed. Comparing GFu against MSKFu over the warm pool shows that GF has stronger drying than MSKF in the  
802 lower troposphere, leading to a lower RH between 850 hPa and 300 hPa in GFu than MSKFu. In addition, GF produces  
803 stronger moistening than MSKF in the upper troposphere leading to a higher RH between 300 hPa and 100 hPa in  
804 GFu than MSKFu. As seen in the bottom panels of Fig. 11, reducing parameterized deep convection while enhancing  
805 grid-scale cloud microphysics produces a higher RH over the refined area in GFv and MSKFv, but without  
806 significantly modifying RH over the coarse area of the mesh. Variations in the vertical distribution of RH at pressures  
807 less than 400 hPa are more pronounced between GFu and GFv than between MSKFv and MSKFu. Because the cloud  
808 fraction (CF) is a function of RH, as described in Xu and Randall (1996; Eq. 1), there is a strong relationship between  
809 the longitude-pressure cross sections of RH and CF, as seen in Fig. S3 (see supplemental figures). The highest CF  
810 coincide with the highest RH at about 100 hPa over the warm pool in all four experiments. As for RH, GFu and GFv  
811 display higher and lower values of CF than MSKFu and MSKFv in the upper and lower troposphere. The top and  
812 bottom panels of Fig. S4 show differences in RH and CF between GFv and GFu, and between MSKFv and MSKFu.  
813 One notable difference is a stronger increase in upper-tropospheric clouds between MSKFu and MSKFv than between

Deleted: S2

Deleted: S3

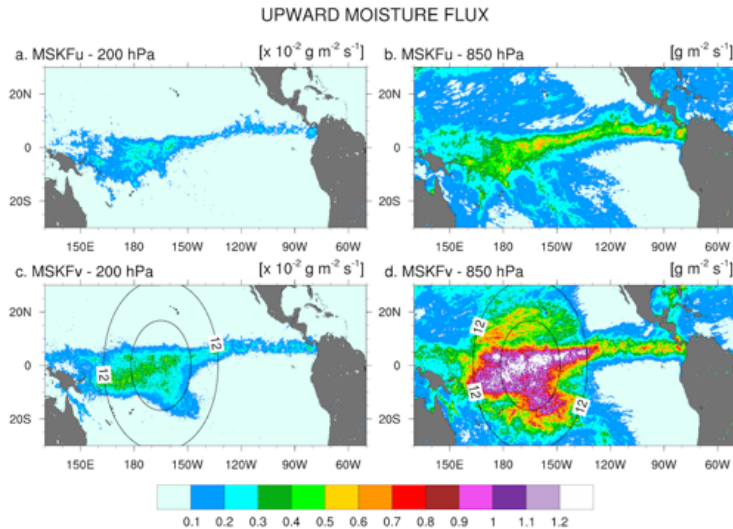
819 GFv and GFu, particularly over the refined area of the mesh. While increased grid-scale condensation over the refined  
 820 area impacts the entire tropospheric in GFv, it more strongly affects the upper-troposphere in MSKFv.



821  
 822 **Figure 11:** Longitude versus pressure cross-section of latitudinally-averaged (between 5°S and 5°N) relative humidity (RH) across  
 823 the Tropical Pacific Ocean simulated in GFu and MSKFu (top panels) and GFu and GFv (bottom panels) for December 2015.

**Formatted: Font: Bold**

824 To explain the change in RH over the refined area between the uniform- and variable-resolution experiments, we  
 825 compare the monthly-mean upward moisture flux at 850 hPa and 200 hPa between MSKFu and MSKFv over the  
 826 Tropical Eastern Pacific (Fig. 12). There is a significant decrease in the upward moisture flux between 850 hPa and  
 827 200 hPa in conjunction with decreased specific humidity with height in MSKFu and MSKFv (Fig. 11). As seen in the  
 828 top panels of Fig. 12, MSKFu yields highest values of the upward moisture flux along the ITCZ and over the warm  
 829 pool in association with parameterized deep convection. Outside the ITCZ and warm pool, lower values of the upward  
 830 moisture flux at 850 hPa result because of reduced deep convection in conjunction with shallow convection, as seen  
 831 over the SPCZ. At increased spatial resolution, convective processes transition from being parameterized to resolved,  
 832 producing larger grid-scale vertical velocities, stronger upward moisture flux, and increased grid-scale condensation  
 833 through the entire troposphere over the refined area of the mesh. Comparing the bottom versus top panels of Fig. 12  
 834 outlines the intensification of vertical moisture transport at both pressure levels over the refined area, leading to the  
 835 increased relative humidity with increased spatial resolutions shown in Fig. 11.



836  
 837 **Figure 12:** 200 hPa (left panels) and 850 hPa (right panels) monthly-mean upward moisture flux simulated with MSKF over the  
 838 Tropical Pacific Ocean for December 2015. Top panels are for MSKFu and bottom panels are for MSKFv. Note the  $1 \times 10^{-2}$  scaling  
 839 between 200 hPa and 850 hPa.

840 **5.2 Liquid Water Path (LWP)**

841 ~~Figure 13 displays difference maps between the simulated and satellite-derived LWP, and between GFv (MSKFv)~~  
 842 ~~and GFu (MSKFu). In Fig. 13, the simulated LWP is calculated using only the grid-scale cloud liquid water mixing~~  
 843 ~~ratio from THOM. Separate analyses would show that adding the prognostic grid-scale rain mixing ratio to the~~  
 844 ~~simulated LWP further increases biases when compared against the SSF LWP (not shown for brevity). We also did~~  
 845 ~~not include the contribution of the convective cloud liquid water mixing ratio to the LWP which is small compared to~~  
 846 ~~that from the grid-scale cloud microphysics. Fig. 13 highlights that GFu strongly overestimates the LWP over the~~  
 847 ~~ITCZ, and between 20°N (20°S) and the northern (southern) limits of our analysis. As seen in Fig. 6, GFu attempts to~~  
 848 ~~form low-level boundary layer clouds off the coast of Peru but these clouds form too far west from the coast when~~  
 849 ~~compared against observations. This same bias is depicted in Fig 13.a since these low-level boundary layer clouds are~~  
 850 ~~characterized by high LWP. In Fig. 13.b, decreased bias between the MSKFu and SSF LWP reflects that the LWP is~~  
 851 ~~strongly decreased in MSKFu compared to GFu, outside of areas of low-level boundary layer clouds. If we set aside~~  
 852 ~~that MSKFu is unable to simulate low-level clouds off the Baja Peninsula and coast of Peru, the magnitude and~~  
 853 ~~regional patterns of the LWP simulated in MSKFu is in fairly good agreement with the SSF LWP. Because MSKF~~  
 854 ~~does not allow deep and shallow convection to coexist within the same grid-cell and deep convection dominates~~  
 855 ~~shallow convection over the ITCZ and warm pool, we suggest that detrained cloud water from deep convection as a~~  
 856 ~~source to grid-scale microphysics contributes a major part to the LWP produced by MSKF. The bottom panels of~~  
 857 ~~Fig. 13 reveal that the mesh refinement impacts the LWP simulated with MSKF more effectively than that simulated~~

**Formatted:** Font: Bold

**Deleted:** The LWP from the four simulations (Fig. 14) is evaluated with satellite-derived LWP (shown in Fig. 5) as well as compared among the simulations. In Fig. 14, the

**Deleted:** Comparing

**Deleted:** a with Fig. 5.a

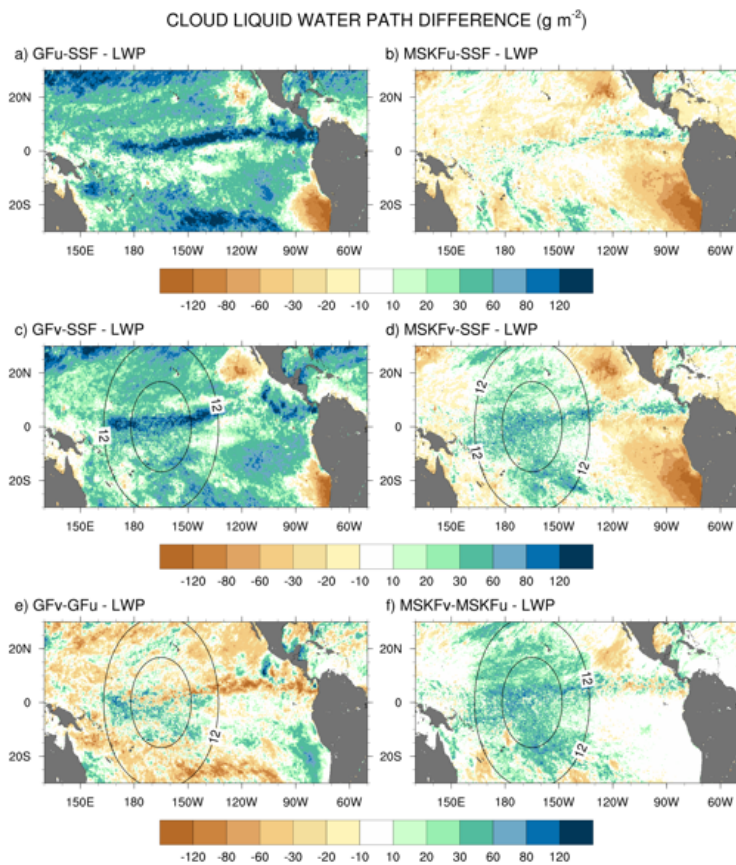
**Deleted:** shows

**Deleted:** relatively

**Deleted:** convective

**Deleted:** (Fig. 14.b).

867 with GF inside the refined area. This result is in agreement with the stronger increase in RH between MSKFu and  
 868 MSKFv than between GFu and GFv at lower levels. MSKFv yields an increased LWP relative to MSKFu over the  
 869 entire refined area (Fig. 13.f). MSKFv also has increased LWP compared to MSKFu over the coarse area, but not as  
 870 large as that seen over the refined area. Fig. 13.e shows that LWP differences do not have a strong positive or negative  
 871 trend inside the refined area, due to the fact that GF allows deep and shallow convection to coexist within the same  
 872 grid-cell of deepest convective activity, mainly over the ITCZ and warm pool, and shallow convection does not  
 873 account for variations in horizontal grid-spacing. Over the coarse area, an obvious decrease in the LWP between GFv  
 874 and GFu is seen over the ITCZ, in the Tropical Eastern Pacific as well as along the southern boundary of our analysis.



875  
 876 **Figure 13:** Monthly-mean cloud liquid water path (LWP) difference over the Tropical Pacific Ocean between GFu (MSKFu) and  
 877 SSF data (top panels), GFv (MSKFv) and SSF data (middle panels), and monthly-mean LWP difference between GFv (MSKFv)  
 878 and GFu (MSKFu) (bottom panels) for December 2015.

**Deleted:** and outside

**Moved (insertion) [2]**

**Deleted:** of the mesh. The

**Deleted:** predicted by GFu and GFv does

**Formatted:** Font color: Auto

**Deleted:** While GFv mostly leads to a decrease in the LWP between GFu and GFv over the coarse area, some grid cells inside the refined area show a decrease in the LWP while other neighboring grid-cells show an increase in the LWP between GFu and GFv.

**Deleted:** along

**Deleted:** .....Section Break (Next Page).....

**Deleted:** simulated with

**Deleted:** and

**Deleted:** ) and

**Deleted:** and

**Deleted:** and GFu, and

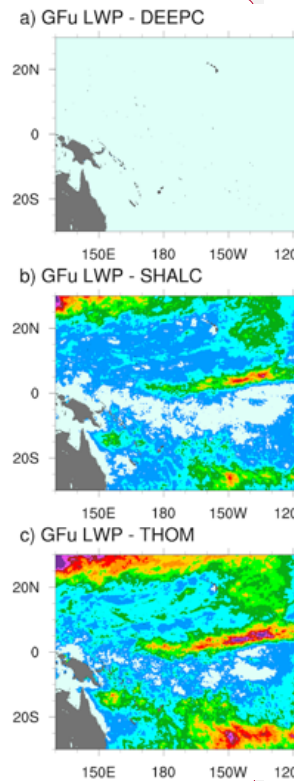
**Formatted:** Font: Bold



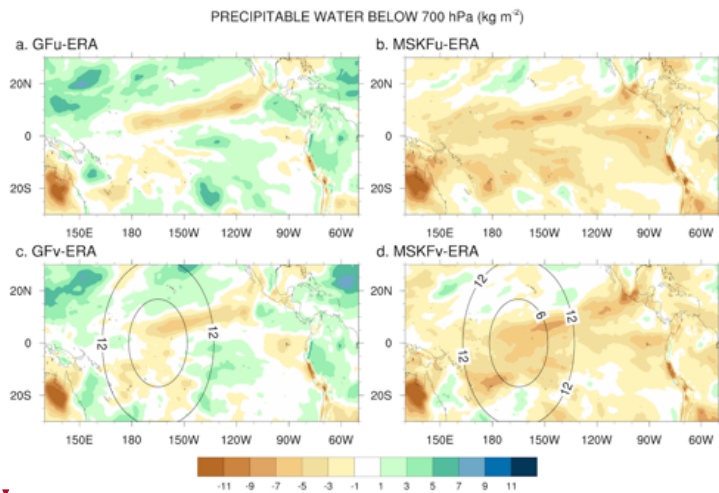
896 In order to investigate the reasons why the LWP simulated in GFu strongly exceeds that from the SSF products  
 897 and MSKFu, we calculated the monthly-mean LWP produced in grid-cells with incidence of deep convection, shallow  
 898 convection, and no convection, using LWP hourly outputs from GFu. Separate maps would show that a major fraction  
 899 of the LWP over convectively active regions such as the ITCZ is actually produced at times when no convection is  
 900 active or when only shallow convection is triggered. In GF, and in contrast to deep convection, shallow convection  
 901 detrains total water as a source of grid-scale water vapor instead of detrainning water vapor, cloud liquid and ice water,  
 902 separately. Because the detrained total water is treated as a source of water vapor, supersaturation conditions are more  
 903 likely to persist and later removed by grid-scale condensation. In contrast, detrainment from deep convective updrafts  
 904 acts as a source of liquid water if temperatures are warmer than 258 K. Deep convection in conjunction with grid-  
 905 scale condensation contributes the least to the LWP because updrafts are taller and their cloud-top temperatures colder  
 906 than those from shallow convection, leading to condensation and deposition to occur at levels where temperatures are  
 907 colder than 258 K, and where ice phase processes dominate.

908 The impact of more active shallow convection in GFu (GFv) than in MSKFu (MSKFv) is analyzed using Fig. 14  
 909 which shows differences in the monthly-mean precipitable water below 700 hPa between our experiments and ERA-  
 910 Interim reanalyses. Because varying horizontal resolution does not affect shallow convection, GFv (MSKFv) displays  
 911 similar biases as GFu (MSKFu) over the entire analysis domain, including the refined area. Comparing the left versus  
 912 right panels of Figure 14 reveals that the precipitable water simulated in GFu (GFv) displays a positive bias whereas  
 913 that simulated in MSKFu (MSKFv) displays a negative bias in the lower troposphere relative to ERA-Interim data,  
 914 mainly over areas of shallow convection. In GF, the abundance of shallow convection (Figure 6.a, Figure 6.c)  
 915 associated with detrained total water acting as a source of grid-scale water vapor promotes the lower troposphere to  
 916 stay more humid and cloud liquid water to form more often than actually observed (Figure 13.a, Figure 13.c), north  
 917 and south of the ITCZ and warm pool. In MSKF, while shallow convection is as widespread over the Tropical Pacific  
 918 Ocean as in GF, it cannot act as a major source of detrained total water to the grid-scale microphysics because it is not  
 919 triggered as often as deep convection. In addition, because MSKF partitions detrained water into water vapor, cloud  
 920 water, cloud ice, rain, and snow, instead of detraining total water in the form of water vapor as in GF, the amounts of  
 921 available water vapor and cloud liquid water are reduced relative to GF.

**Deleted:** calculate...calculated the monthly-mean LWP produced in grid-cells with incidence of deep convection, shallow convection, and without any kind of...o convection, using LWP hourly outputs of the LWP ...rom GFu. Comparing Fig. 15 a against Figs. 15.b and 15.c shows...eparate maps would show that a major fraction of the LWP over convectively active regions such as the ITCZ is actually produced at times when no convection is active or when only shallow convection is triggered. In contrast, the LWP produced in grid-cells with deep convection does not exceed 20 g m<sup>-2</sup> at the scale used in Fig. 15. ...n GF, and in contrast to deep convection, shallow convection detrains total water as a source to ...f grid-scale water vapor instead of detraining water vapor, and ...loud liquid and ice water, separately. Because the detrained total water is treated as a source of water vapor, supersaturation conditions are more likely to persist and later removed by grid-scale condensation. In contrast, detrainment from deep convective updrafts acts as a source of liquid water if temperatures are warmer than 258 K. Deep convection in conjunction with grid-scale condensation contributes the least to the LWP because updrafts are taller and their cloud-top temperatures colder than those formed ... [6]



**Deleted:**  
**Figure 15:** Monthly-mean of cloud liquid water path of corresponding to a) deep convection only (DEEPC); b) shallow convection only (SHALC); and c) no convection (THOM) simulated with GFu over the Tropical Pacific Ocean for December 2015.¶ ... [7]



1036

1037 **Figure 14:** Monthly-mean difference between the simulated and ERA-Interim precipitable water below 700 hPa over the Tropical  
 1038 Pacific Ocean for December 2015.

1039 **5.3 Ice Water Path (IWP)**

1040 Because MODIS is relatively insensitive to precipitation, the simulated IWP should comprise cloud ice, snow,  
 1041 and graupel. Because graupel contributes a minor part to the IWP relative to cloud ice and snow and our results  
 1042 highlight strong biases against SSF data, we do not include graupel in our computation of the simulated IWP. It is also  
 1043 important to note that because THOM has the propensity to rapidly convert cloud ice to snow (Thompson et al. 2016),  
 1044 most of the IWP is in the form of snow which falls at higher speeds than cloud ice, enhancing the depth of ice clouds.  
 1045 Lastly, the middle panels of Fig. 5 show that our gridding of the IWP orbital data produce increased monthly mean  
 1046 IWP than the official SSF1deg product. This result implies that biases between the simulated and satellite-derived  
 1047 IWP will be underestimated when using our SSF 0.2°x0.2° IWP data. Figure 15 shows difference maps between the  
 1048 simulated and satellite-derived IWP, and between GFv (MSKFv) and GFu (MSKFu). When compared against the SSF  
 1049 IWP, GFu is the only experiment that mostly underestimates the IWP along the ITCZ and warm pool, whereas GFv  
 1050 yields a strong increase in the IWP over the refined area of the mesh relative to GFu. Both GFu and GFv overestimate  
 1051 the IWP along the west coast of Central America, as they did for the LWP and precipitation. Comparing MSKFu  
 1052 (MSKFv) against GFu (GFv) shows that MSKF leads to increased positive biases in the IWP compared to GF over  
 1053 the entire ITCZ and warm pool. Increased convective detrainment of cloud ice as a source of grid-scale cloud ice to  
 1054 THOM in MSKF than in GFv, because partitioning between cloud liquid and ice water starts at warmer temperatures,  
 1055 may be responsible to the increased IWP. The bottom panels of Figure 15 reveal that increasing spatial resolution  
 1056 worsens the simulated IWP compared to the SSF IWP over the refined area in GFv and MSKFv. As shown in Fig. 11,  
 1057 mesh refinement over the warm pool yields higher upper-tropospheric relative humidity leading to increased ice cloud

1036

1037 **Figure 14:** Monthly-mean difference between the simulated and ERA-Interim precipitable water below 700 hPa over the Tropical  
 1038 Pacific Ocean for December 2015.

1039 **5.3 Ice Water Path (IWP)**

1040 Because MODIS is relatively insensitive to precipitation, the simulated IWP should comprise cloud ice, snow,  
 1041 and graupel. Because graupel contributes a minor part to the IWP relative to cloud ice and snow and our results  
 1042 highlight strong biases against SSF data, we do not include graupel in our computation of the simulated IWP. It is also  
 1043 important to note that because THOM has the propensity to rapidly convert cloud ice to snow (Thompson et al. 2016),  
 1044 most of the IWP is in the form of snow which falls at higher speeds than cloud ice, enhancing the depth of ice clouds.  
 1045 Lastly, the middle panels of Fig. 5 show that our gridding of the IWP orbital data produce increased monthly mean  
 1046 IWP than the official SSF1deg product. This result implies that biases between the simulated and satellite-derived  
 1047 IWP will be underestimated when using our SSF 0.2°x0.2° IWP data. Figure 15 shows difference maps between the  
 1048 simulated and satellite-derived IWP, and between GFv (MSKFv) and GFu (MSKFu). When compared against the SSF  
 1049 IWP, GFu is the only experiment that mostly underestimates the IWP along the ITCZ and warm pool, whereas GFv  
 1050 yields a strong increase in the IWP over the refined area of the mesh relative to GFu. Both GFu and GFv overestimate  
 1051 the IWP along the west coast of Central America, as they did for the LWP and precipitation. Comparing MSKFu  
 1052 (MSKFv) against GFu (GFv) shows that MSKF leads to increased positive biases in the IWP compared to GF over  
 1053 the entire ITCZ and warm pool. Increased convective detrainment of cloud ice as a source of grid-scale cloud ice to  
 1054 THOM in MSKF than in GFv, because partitioning between cloud liquid and ice water starts at warmer temperatures,  
 1055 may be responsible to the increased IWP. The bottom panels of Figure 15 reveal that increasing spatial resolution  
 1056 worsens the simulated IWP compared to the SSF IWP over the refined area in GFv and MSKFv. As shown in Fig. 11,  
 1057 mesh refinement over the warm pool yields higher upper-tropospheric relative humidity leading to increased ice cloud

Deleted: and simple weighting

Deleted: higher

Deleted: that from

Deleted: Comparing

Deleted: ) shown in Fig. 17

Deleted: (Fig. 5.c) reveals that

Deleted: (MSKFu) tends to underestimate (overestimate)

Deleted: over

Deleted: , and that

Deleted: MSKFu both

Deleted: , Comparing the top and middle panels of Fig. 17 highlights that MSKFu

Deleted: MSKFv yield higher IWP than GFu and GFv

Deleted: MSKFu

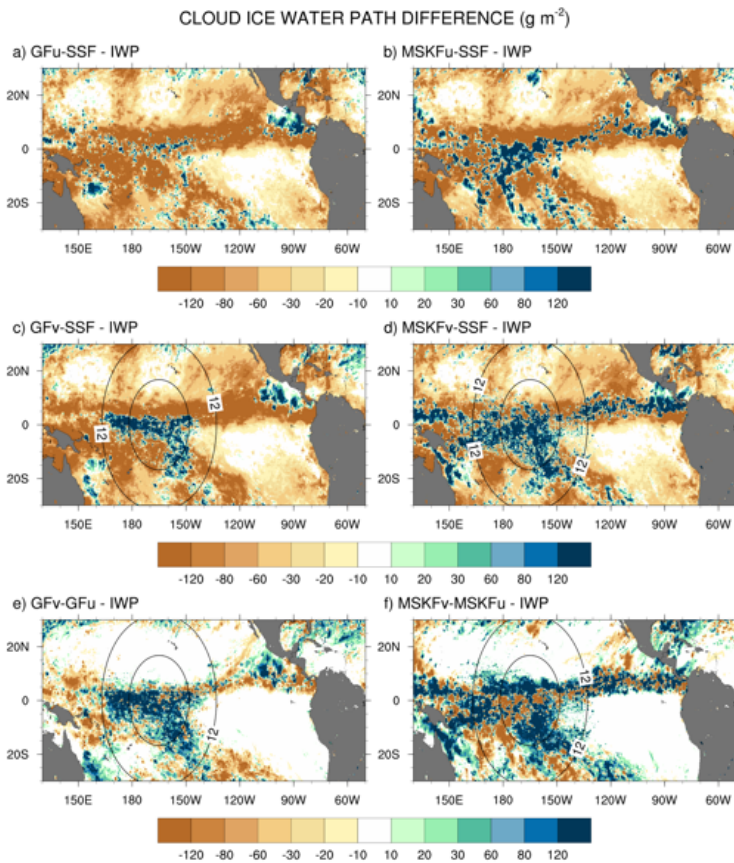
Deleted: due to the fact that

Deleted: in MSKFu than GFu

Deleted: Fig.

Deleted: produces

1077 microphysics. In contrast to GFv, MSKFv displays an increase in the IWP over the coarse area of the mesh, showing  
 1078 a stronger impact of the refined area on the coarse area of the mesh in MSKFv than GFv in the upper-troposphere.

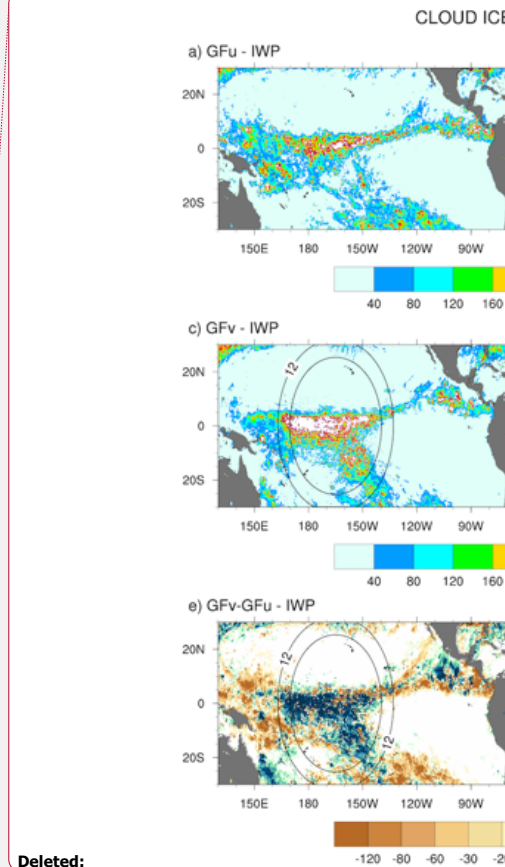


1079  
 1080 **Figure 15:** As Fig. 13, but for the cloud ice water path (IWP).

1081 **5.4 TOA radiation budget**

1082 Biases in the LWP and IWP introduce biases in the cloud fraction and cloud optical properties which in turn lead  
 1083 to biases in the simulated TOALW and TOASW compared to CERES-SSF data. Figures ~~S5~~, ~~S6~~, and ~~S7~~ display the  
 1084 monthly-mean CF, TOALW, and TOASW from SSF data for December 2015 and the differences between the model  
 1085 results and observations. Focusing on areas of deep convection over the ITCZ and warm pool, all four simulations  
 1086 overestimate CF with larger biases seen in the GF than the MSKF experiments, and larger biases seen in the variable-  
 1087 resolution than the uniform-resolution experiments. All four simulations also overpredict CF along the west coast of  
 1088 Central America while underpredicting CF over areas of stratiform clouds along the west coast of South America and

Deleted: upscaling effect



Deleted:

Deleted: S4,

Deleted: S6

1093 Baja Peninsula. The impact of CF biases is that all four experiments underestimate the size of the warm pool and  
1094 width of the ITCZ, leading the TOALW (TOASW) to be too high (low) over areas of deep convection. These  
1095 differences are clearly linked to the differences noted in the LWP and IWP between MPAS and SSF data.

## 1096 6 Discussion and future research

1097 Uniform- and variable-resolution experiments with two scale-aware parameterizations of deep convection (GF  
1098 and MSKF) in MPAS yield significant biases between the simulated and satellite-derived monthly-mean precipitation  
1099 rates, LWP, IWP, and CF over the Tropical Pacific Ocean for December 2015. In turn, biases affect the cloud fraction  
1100 and optical properties producing significant differences in the TOALW and TOASW compared to CERES-SSF data.  
1101 Tropical precipitation simulated with uniform-resolution experiments is overestimated compared to TMPA, due  
1102 to subgrid-scale deep convection. Biases using GF are as large as those using MSKF, and result in part because the  
1103 simulated ITCZ is located south of its observed location. Variable-resolution experiments do not produce significant  
1104 improvement in simulating precipitation against TMPA. Inside the refined area, decreased convective precipitation  
1105 plus compensating increased grid-scale precipitation have the simulated total precipitation to exhibit similar biases  
1106 between the uniform- and variable-resolution experiments with GF and MSKF. One major difference in using GF  
1107 instead of MSKF is the strong upscaling effect of the refined mesh on the coarse mesh, producing a strong increase in  
1108 convective precipitation east and west of the refined mesh. Because deep convection does not exhibit similar behaviour  
1109 over the transition zone between the coarse and refined areas of the mesh in MSKF, we plan further to investigate this  
1110 difference in convective precipitation in terms of the size of convective updrafts as a function of horizontal resolution  
1111 and increased moistening of the lower troposphere from shallow convection.

1112 Differences in the simulated LWP between the uniform- and variable-resolution experiments using GF and MSKF  
1113 and against the CERES-SSF LWP highlight the need to revise the treatment of shallow convection to improve warm-  
1114 phase clouds in both schemes. While experiments using MSKF yield the simulated LWP to be in reasonable agreement  
1115 against that from the CERES-SSF product, those using GF yield the simulated LWP to be strongly overestimated.  
1116 Analyses show that shallow convection and cloud microphysics processes explain most of the increased LWP in GFu  
1117 and GFv compared to MSKFu and MSKFv, and satellite-derived data. We plan to update the GF shallow convection  
1118 scheme with that implemented in version 4.1 of the Advanced Research Weather Forecast (WRF) model. Because the  
1119 updated scheme includes an improved cloud model that allows water vapor and cloud liquid water to detrain separately  
1120 and a fraction of condensed water to precipitate, we will focus on the impact of explicit detrainment of cloud liquid  
1121 water and precipitation from shallow convective updrafts on the simulated LWP in GF. Results show that MSKF  
1122 underestimates shallow convection, leading the troposphere below 700 hPa to be drier than actually observed. These  
1123 results imply that the shallow convection in MSKF needs to be updated or that a separate parameterization of shallow  
1124 convection needs to be used in addition to that in MSKF. Using the same parameterization of shallow convection, and  
1125 partitioning of the detrained condensed water between cloud liquid water and ice in GF and MSKF, will further provide  
1126 understanding in the partitioning of the LWP between subgrid-scale deep and shallow convection. Variable-resolution  
1127 experiments strongly overestimate the IWP compared to CERES-SSF data over the refined area of the mesh, leading  
1128 to strong biases in the cloud fraction, and TOA long- and short-wave radiation. Because subgrid-scale deep convection

**Deleted:** and shallow ... convection (GF and MSKF) in MPAS yield significant biases between the simulated and satellite-derived monthly-mean precipitation rates, LWP, IWP, and CF over the Tropical Pacific Ocean at horizontal resolutions of 30 km down to 6 km. Because these ... or December 2015. In turn, biases affect the cloud fraction and cloud ... ptical properties, the four experiments present ... producing significant differences in the TOALW and TOASW compared to CERES-SSF data for December 2015 ... [8]

**Deleted:** Precipitation ... tropical precipitation simulated with the uniform-resolution experiments is overestimated compared to TMPA data ... due to subgrid-scale deep convection. Biases using GF are as large as those using MSKF, but part of the biases ... and result in part because the simulated ITCZ is located south of its observed location depicted as an area of maximum precipitation ... Variable-resolution experiments do not yield ... reduce significant improvement in simulating precipitation against TMPA. Inside the refined area, decreased convective precipitation plus compensating increased grid-scale precipitation have the simulated total precipitation to exhibit similar biases between our ... the uniform- and variable-resolution experiments with both ... F and MSKF. One major difference in using GF instead of MSKF is the strong upscaling effect of the refined grid ... mesh on the coarse grid ... mesh, producing a strong increase in convective precipitation east and west of the refined area ... mesh. Because deep convection does not exhibit similar behaviour over the transition zone between the coarse and refined areas of the mesh which did not exist ... in the ... SKF. We ... we plan to ... further understand how the scale-aware formulation ... o investigate this difference in convective precipitation in terms of deep convection in GF affect large-scale moist processes, leading to ... he size of convective updrafts as a function of horizontal resolution and increased triggering of ... oistening of the lower troposphere from shallow convection over the coarse area of the mesh ... [9]

**Deleted:** convection ... schemes and of its interactions with deep convection and cloud microphysics ... While experiments using MSKF yield the simulated LWP to be in reasonable agreement against that from the CERES-SSF product, those using GF yield the simulated LWP to be strongly overestimated. Analyses show that the treatment of ... hallow convection in conjunction with ... and cloud microphysics processes explains ... explain most of the increased LWP in GFu and GFv compared to MSKFu and MSKFv, and satellite-derived data. We propose ... lan to update our version of ... he GF shallow convection scheme to ... ith that implemented in version 4.1 of the Advanced Research Weather Forecast (WRF) model. Because the updated GF parameterization of shallow convection ... scheme includes a revised ... n improved cloud model that allows water vapor and cloud liquid water to detrain separately and a fraction of the condensed water to precipitate, we propose to ... ill focus future research ... on the impact of explicit detrainment of cloud liquid water and precipitation from shallow convective updrafts on the simulated LWP in GF. Results show that MSKF underestimates shallow convection, leading the troposphere below 700 hPa to be drier than actually observed. These results imply that the shallow convection parameterization ... n MSKF needs to be updated or that a separate parameterization of shallow convection needs to be used in addition to that in MSKF, which can be a part ... Using the same parameterization of our future study. The uniform- ... hallow convection, and variable ... aritioning of the detrained condensed water between cloud liquid water and ice in GF and MSKF, will further provide understanding in the partitioning of the LWP between subgrid-scale deep and shallow convection. Variable-resolution experiments performed here all overestimated ... strongly overestimate the IWP compared to CERES-SSF data over the tropical Pacific region. This overprediction ... efined area of the IWP led ... mesh, leading to strong biases in the cloud fraction, and TOA long- and short-wave radiation budget compared ... [10]

1243 ~~is reduced at increased horizontal resolutions. grid-scale cloud microphysics contributes a major part to biases in the~~  
1244 ~~simulated IWP.~~

1245 ~~Parameterizing the dependence of subgrid-scale deep convection as a function of horizontal resolution allows the~~  
1246 ~~use of variable-resolution meshes spanning between hydrostatic and nonhydrostatic scales within a global framework~~  
1247 ~~for regional NWP and climate experiments. Although deep convection is not fully explicitly resolved over the refined~~  
1248 ~~area of the mesh in our variables-resolution experiments, it is substantially reduced relative to that over the coarse area~~  
1249 ~~of the mesh, allowing to contrast the contribution of subgrid-scale convection and cloud microphysics processes.~~ As  
1250 horizontal resolution increases from the coarse to refined area of the mesh, ~~deep convection gradually~~ transitions from  
1251 parameterized to resolved and cloud microphysics contribute a major part to moist processes over the refined ~~mesh.~~  
1252 ~~Shallow convection coupled with grid-scale microphysics contributes a major part to the low-level cloud liquid water~~  
1253 ~~and mixed-phase clouds whereas grid-scale cloud microphysics contribute a major part to the formation of upper-~~  
1254 ~~tropospheric ice clouds over the refined area.~~ Our results show that mesh refinement ~~does not systematically improve~~  
1255 precipitation and clouds ~~over the Tropical Pacific Ocean as grid-scale condensation increases at increased resolutions.~~  
1256 As cloud microphysics processes drive the moisture budget over the refined area of the mesh, we propose to expand  
1257 this diagnostic study to a process study by further understanding the cloud microphysics ~~processes that need to be~~  
1258 improved ~~in order to reduce discrepancies between model and observations.~~ In that vein, the recently developed MSKF  
1259 that includes a double moment microphysics (Glotfelty et al., 2019) would be useful in a future process study.

1260  
1261  
1262 *Code and data availability:* The source code used to initialize and run our experiments is based on MPAS-v5.2 which  
1263 is freely available from <https://github.com/MPAS-Dev/MPAS-Model/releases/tag/v5.2>. Modifications to the original  
1264 source code and scripts to run the experiments are available from <https://doi.org/10.5281/zenodo.3515440> (Fowler,  
1265 2019) while initialization files, and outputs from the experiments are located on the NCAR Campaign Storage System.  
1266 These files can be made available by contacting the corresponding author. Examples of CERES SSF Aqua and Terra  
1267 orbital and gridded data, daily-mean and monthly-mean simulated diagnostics, and post-processing scripts are also  
1268 available from <https://doi.org/10.5281/zenodo.3515440> (Fowler, 2019).

1269  
1270  
1271 *Author contributions:* LF developed all the modifications that were made to the MPAS-v5.2 released version and were  
1272 necessary to run the different experiments. KA made all the updates to the MultiScale Kain-Fritsch parameterization  
1273 of convection. LF and MB designed the experiments, and LF conducted and analyzed the simulations. LF prepared  
1274 the manuscript with contributions from all co-authors.

1275  
1276  
1277 *Competing interests:* The authors declare that they have no conflict of interest.

1278  
1279

**Deleted:** observations

**Deleted:** The scale-aware

**Deleted:** parameterized

**Deleted:** allows

**Deleted:** to be used

**Deleted:** .

**Deleted:** grid-scale

**Deleted:** grid mesh. Stronger grid-scale vertical velocities associated

**Deleted:** smaller grid-spacing over the refined area produce increased upward moisture flux and grid-scale condensation, further increasing biases between the simulated and satellite-retrieved LWP, IWP,

**Deleted:** .

**Deleted:** over the Tropical Pacific Ocean

**Deleted:** , due to complicated interactions between convection, cloud microphysics, and radiation

**Deleted:** tendencies

**Deleted:** with the aim

1299 *Acknowledgments:* This research is based upon work supported by the National Center for Atmospheric Research  
1300 which is a major facility sponsored by the National Science Foundation under Cooperative Agreement No. 1852977.  
1301 The authors thank Dr. Hugh Morrison for his careful review and constructive suggestions of the manuscript prior to  
1302 its submission. The CERES-SSF data were obtained from the NASA Langley Research Center Atmospheric Science  
1303 Data Center. The TMPA data were acquired as part of the activities of NASA's Science Mission Directorate and are  
1304 archived and distributed by the Goddard Earth Sciences (GES) Data and Information Services Center (DISC). We  
1305 would like to acknowledge high-performance computing support from Cheyenne (doi:10.5065/D6RX99hX) provided  
1306 by NCAR's Computational and Information Systems Laboratory, sponsored by the National Science Foundation. We  
1307 acknowledge the use of the NCAR Command Language (Version 6.3.2) [Software]. (2019). Boulder, Colorado:  
1308 UCAR/NCAR/CISL/TDD. <http://dx.doi.org/10.5065/D6WD3XH5> for all figures.

1309

## References

- 1310 Alapaty, K., Herwehe, J.A., Otte, T.L., Nolte, C.G., Bullock, O.R., Ballard, M.S., Kain, J.S., and Dudhia, J.:  
1311 Introducing subgrid-scale cloud feedbacks to radiation for regional meteorological and climate modeling,  
1312 *Geophys. Res. Lett.*, 39, L24809, <https://doi.org/10.1029/2012GL054031>, 2012.
- 1313 Alishouse, J.C., Snider, J.B., Westwater, E.R., Swift, C.T., Ruf, C.S., Vongsathron, S.A., and Ferraro, R.R.:  
1314 Determination of cloud liquid water content using the SSM/I, *IEEE T. Geosci. Remote*, 28, 817-822,  
1315 <https://doi.org/10.1109/36.58968>, 1990.
- 1316 Arakawa, A., and Schubert, W.H.: Interaction of a cumulus cloud ensemble with the large-scale environment, Part I,  
1317 *J. Atmos. Sci.*, 31, 674-701, [https://doi.org/10.1175/1520-0469\(1974\)031<0674:IOACCE>2.0.CO;2](https://doi.org/10.1175/1520-0469(1974)031<0674:IOACCE>2.0.CO;2), 1974.
- 1318 Arakawa, A., and Wu, C.-M.: A unified representation of deep moist convection in numerical modeling of the  
1319 atmosphere. Part I, *J. Atmos. Sci.*, 70, 1977-1992, <https://doi.org/10.1175/JAS-D-12-0330.1>, 2013.
- 1320 Bechtold, P., Bazile, E., Guichard, F., Mascart, P., and Richard, E.: A mass-flux convection scheme for regional and  
1321 global models, *Q. J. Roy. Meteor. Soc.*, 130, 3139-3172, <https://doi.org/10.1002/qj.49712757309>, 2001.
- 1322 Bechtold, P., Köhler, M., Jung, T., Doblas-Reyes, F., Leutbecher, M., Rodwell, M. J., Vitart, F., and Balsamo, G.:  
1323 Advances in simulating atmospheric variability with the ECMWF model: From synoptic to decadal time-scales,  
1324 *Q. J. Roy. Meteor. Soc.*, 134, 1337-1351, <https://doi.org/10.1002/qj.289>, 2008.
- 1325 Brown, J.M.: Mesoscale unsaturated downdrafts driven by rainfall evaporation: A numerical study, *J. Atmos. Sci.*, 36,  
1326 313-338, [https://doi.org/10.1175/1520-0469\(1979\)036<0313:MUDDBR>2.0.CO;2](https://doi.org/10.1175/1520-0469(1979)036<0313:MUDDBR>2.0.CO;2), 1979.
- 1327 Chen, F., and Dudhia, J.: Coupling an advanced land surface-hydrology model with the Penn State-NCAR MM5  
1328 modeling system. Part I: Model implementation and sensitivity, *Mon. Weather Rev.*, 129, 569-585,  
1329 [https://doi.org/10.1175/1520-0493\(2001\)129<0569:CAALSH>2.0.CO;2](https://doi.org/10.1175/1520-0493(2001)129<0569:CAALSH>2.0.CO;2), 2001.
- 1330 Dee, D.P., and 35 co-authors: The ERA-Interim reanalysis: configuration and performance of the data assimilation  
1331 system, *Q. J. Roy. Meteor. Soc.*, 137, 553-597, <https://doi.org/10.1002/qj.828>, 2011.
- 1332 Dolinar, E.K., Dong, X., Xi, B., Jiang, J.H., and Su, H.: Evaluation of CMIP5 simulated clouds and TOA radiation  
1333 budgets using NASA satellite observations, *Clim. Dynam.*, 44, 2229-2247, <https://doi.org/10.1007/s00382-014-2158-9>, 2015.
- 1335 Fowler, L.D., Skamarock, W.C., Grell, G.A., Freitas, S.R., and Duda, M.G.: Analyzing the Grell-Freitas convection  
1336 scheme from hydrostatic to nonhydrostatic scales within a global model, *Mon. Weather Rev.*, 144, 2285-2306,  
1337 <https://doi.org/10.1175/MWR-D-15-0311.1>, 2016.
- 1338 Frank, W.M., and Cohen, C.: Simulation of tropical convective systems. Part I: A cumulus parameterization, *J. Atmos.*  
1339 *Sci.*, 44, 3787-3799, [https://doi.org/10.1175/1520-0469\(1987\)044<3787:SOTCSP>2.0.CO;2](https://doi.org/10.1175/1520-0469(1987)044<3787:SOTCSP>2.0.CO;2), 1987.

1340 Fritsch, J.M., and Chappell, C.F.: Numerical prediction of convectively driven mesoscale pressure systems. Part I:  
1341 Convective parameterization, *J. Atmos. Sci.*, 37, 1722–1733, [https://doi.org/10.1175/1520-0469\(1980\)037<1722:NPOCDM>2.0.CO;2](https://doi.org/10.1175/1520-0469(1980)037<1722:NPOCDM>2.0.CO;2), 1980.

1342

1343 Fowler, L.D.: experimentsMPAS-v5.2, Zenodo, <https://doi.org/10.5281/zenodo.3515440>, 2019.

1344 Geier, E.B., Green, R.N., Kratz, D.P., Minnis, P., Miller, W.F., Nolan, S.K., and Franklin, C.B.: Clouds and the Earth’s  
1345 Radiant Energy System (CERES) data management system. Single Satellite Footprint TOA/Surface Fluxes and  
1346 Clouds (SSF) collection document. Release 2, Version 1, 243 pp, 2003.

1347 Giorgetta, M.A., Brokopf, R., Crueger, T., Esch, M., Fiedler, S., Helmert, J., Hohenegger, C., Kornbluh, L., Köhler,  
1348 M., Manzini, E., Mauritsen, T., Nam, C., Raddatz, T., Rast, S., Reinert, D., Sakradzija, M., Schmidt, H., Schneck,  
1349 R., Schnur, R., Silvers, L., Wan, H., Zängl, G., and Stevens, B: ICON-A, the atmosphere component of the ICON  
1350 Earth System Model: I. Model description, *J. Adv. Model. Earth Sy.*10, 1613-1637,  
1351 <https://doi.org/10.1029/2017MS001242>, 2018.

1352 Glotfelty, T., Alapaty, K., He, J., Hawbecker, P., Song, X., and Zhang, G.: The Weather Research and Forecasting  
1353 Model with aerosol cloud-interactions (WRF-ACI): Development, evaluation, and initial applications, *Mon. Wea.*  
1354 *Rev.*, 147, 1491-1511, <https://doi.org/10.1175/MWR-D-18-0267.1>, 2019.

1355 Greenwald, T.J., Stephens, G.L., Vonder Haar, T.H., and Jackson, D.L.: A physical retrieval of cloud liquid water  
1356 over global oceans using special sensor microwave/imager (SSM/I) observations, *J. Geophys. Res.*, 98, 18471-  
1357 18488, <https://doi.org/10.1029/93JD00339>, 1993.

1358 Grell, G.A: Prognostic evaluation of assumptions uses by cumulus parameterizations, *Mon. Weather Rev.*, 121, 764-  
1359 787, [https://doi.org/10.1175/1520-0493\(1993\)121<0764:PEOAUB>2.0.CO;2](https://doi.org/10.1175/1520-0493(1993)121<0764:PEOAUB>2.0.CO;2), 1993.

1360 Grell, G.A., and Dévényi, D.: A generalized approach to parameterizing convection combining ensemble and data  
1361 assimilation techniques, *Geophys. Res. Lett.*, 29, 38-1-38-4, <https://doi.org/10.1029/2002GL015311>, 2002.

1362 Grell, G.A., and Freitas, S.R.: A scale and aerosol aware stochastic parameterization for weather and air quality  
1363 modeling, *Atmos. Chem. Phys.*, 14, 5233-5250, <https://doi.org/10.5194/acp-14-5233-2014>, 2014.

1364 Guo, H., Golaz, J.-C., Donner, L., Wyman, B., Zhao, M., and Ginoux, P.: CLUBB as a unified cloud parameterization:  
1365 opportunities and challenges, *Geophys. Res. Lett.*, 42, 4540-4547, <https://doi.org/10.1002/2015GL063672>, 2015.

1366 He, J., and Alapaty, K.: Precipitation partitioning in multiscale atmospheric simulations: Impacts of stability  
1367 restoration methods, *J. Geophys. Res.*, 123, 10185-10201, <https://doi.org/10.1029/2018JD028710>, 2018.

1368 Herwehe, J.A., Alapaty, K., and Bullock Jr., O.R: Evaluation of developments toward a multi-scale Kain-Fritsch  
1369 parameterization in WRF. 2014 Community Modeling and Analysis System Conference, Chapel Hill, NC, EPA,  
1370 2014.

1371 Hong, S.-Y., and Lim, J.-O: The WRF single moment 6-class microphysics scheme (WSM6), *J. Korean Meteor. Soc.*,  
1372 42, 129-151, 2006.



1373 Hong, S.-Y., Choi, J., Chang, E.-C., Park, H., and Kim Y.-J.: Lower-tropospheric enhancement of gravity wave drag  
1374 in a global spectral atmospheric forecast model, *Weather Forecast*, 23, 523-531,  
1375 <https://doi.org/10.1175/2007WAF2007030.1>, 2008.

1376 Huffman, G.J., Balvin, D.T., Nelkin, E.J., and Wolff, D.B.: The TRMM Multisatellite Precipitation Analysis (TMPA):  
1377 Quasi-global, multiyear, combined-sensor precipitation at fine scales, *J. Hydrometeorol.*, 8, 38-55,  
1378 <https://doi.org/10.1175/JHM560.1>, 2007.

1379 Iacono, M. J., Mlawer, E. J., Clough, S. A., and Morcrette, J.-J.: Impact of an improved longwave radiation model,  
1380 RRTM, on the energy budget and thermodynamic properties of the NCAR Community Climate Model, CCM3,  
1381 *J. Geophys. Res.*, 105, 14 873–14 890, <https://doi.org/10.1029/2000JD900091>, 2000.

1382 Jiang, J.H., Su, H., Zhai, C., Perun, V.S, Del Genio, A., Nazarenko, L.S., Donner, L.J., Horowitz, L., Seman, C., Cole,  
1383 J., Gettelman, A., Ringer, M.A., Rotstayn, L., Jeffrey, S., Wu, T., Briant, F., Dufresne, J.-L., Kawai, H., Koshiro,  
1384 T., Watanabe, M., L'Ecuyer, T.S., Volodin, E.M., Iversen, T., Drange, H., Mesquita, M.D.S., Read, W.G., Waters,  
1385 J.W., Tian, B., Teixeira, J., and Stephens, G.L.: Evaluation of cloud and water vapor simulations in CMIP5  
1386 climate models using NASA “A-Train” satellite observations, *J. Geophys. Res.*, 117, D14105,  
1387 <https://doi.org/10.1029/2011JD017237>, 2012.

1388 Ju, L., Ringler, T., and Gunzburger, M.: Voronoi tessellations and their applications to climate and global modeling,  
1389 *Numerical Techniques for Global Atmospheric Models*, P. Lauritzen et al., Eds., Springer, 313-342, 2011.

1390 Kain, J.S.: The Kain-Fritsch parameterization: An update, *J. Appl. Meteorol.*, 43, 170-181,  
1391 [https://doi.org/10.1175/1520-0450\(2004\)043<0170:TKCPAU>2.0.CO;2](https://doi.org/10.1175/1520-0450(2004)043<0170:TKCPAU>2.0.CO;2), 2004.

1392 Kain, J.S, and Fritsch, J.M.: A one-dimensional entraining/detraining plume model and its application in convective  
1393 parameterization, *J. Atmos. Sci.*, 47, 2784-2802, [https://doi.org/10.1175/1520-0469\(1990\)047<2784:AODEPM>2.0.CO;2](https://doi.org/10.1175/1520-0469(1990)047<2784:AODEPM>2.0.CO;2), 1990.

1395 Kain, J.S., and Fritsch, J.M.: The role of convective “trigger function” in numerical forecasts of mesoscale convective  
1396 systems, *Meteorol. Atmos. Phys.*, 49, 93-106, <https://doi.org/10.1007/BF01025402>, 1992.

1397 Kain, J.S., and Fritsch, J.M.: Convective parameterization for mesoscale models: The Kain-Fritsch scheme, *The*  
1398 *Representation of Cumulus Convection in Numerical Models*, Meteor. Mon., No. 24, American Meteorological  
1399 Society, Boston, MA, 165-170, [https://doi.org/10.1007/978-1-935704-13-3\\_16](https://doi.org/10.1007/978-1-935704-13-3_16), 1993.

1400 Kay, J.E., Deser, C., Phillips, A., Mai, A., Hannary, C., Strand, G., Arblaster, J.M., Bates, S.C., Danabasoglu, G.,  
1401 Edwards, J., Holland, M., Kushner, P., Lamarque, J.-F., Lawrence, D., Lindsay, K., Middleton, A., Munoz, E.,  
1402 Neale, R., Oleson, K., Polvani, L., and Vertenstein, M.: The Community Earth System Model (CESM) large  
1403 ensemble project, *B. Am. Meteorol. Soc.*, 96, 1333-1349, <https://doi.org/10.1175/BAMS-D-13-00255.1>, 2015.

1404 Kessler, E.: On the distribution and continuity of water substances in atmospheric circulation, *Meteor. Mon.*, No. 10,  
1405 American Meteorological Society, Boston, MA, 1-84, [https://doi.org/10.1007/978-1-935704-36-2\\_1](https://doi.org/10.1007/978-1-935704-36-2_1), 1969.

1406 Klemp, J.B.: A terrain-following coordinate with smoothed coordinate surfaces, *Mon. Weather Rev.*, 139, 2163-2169,  
1407 <https://doi.org/10.1175/MWR-D-10-05046.1>, 2011

1408 Klemp, J.B., Skamarock, W.C., and Dudhia, J.: Conservative split-explicit time integration methods for the  
1409 compressible ~~nonhydrostatic~~ equations, *Mon. Weather Rev.*, 135, 2897-2913,  
1410 <https://doi.org/10.1175/MWR3440.1>, 2007.

1411 Krishnamurti, T.N., Low-Nam, S., and Pasch, R.: Cumulus parameterization and rainfall rates II, *Mon. Weather Rev.*,  
1412 111, 815-828, [https://doi.org/10.1175/1520-0493\(1983\)111<0815:CPARRI>2.0.CO;2](https://doi.org/10.1175/1520-0493(1983)111<0815:CPARRI>2.0.CO;2), 1983.

1413 Li, J.-L., Waliser, D., Woods, C., Teixeira, J., Baumeister, J., Chern, J., Shen, B.-W., Tompkins, A., Tao, W.-K., and  
1414 Köhler, M.: Comparisons of satellites liquid water estimates to ECMWF and GMAO analyses, 20<sup>th</sup> century IPCC  
1415 AR4 climate simulations and GCM simulations, *Geophys. Res. Lett.*, 35, L9710,  
1416 <https://doi.org/10.1029/2008GL035427>, 2008.

1417 Li, J.-L., Waliser, D.E., Chen, W.-T., Guan, B., Kubar, T., Stephens, G., Ma, H.-Y., Deng, M., Donner, L., Seman, C.  
1418 , and Horowitz, L.: An observational based evaluation of cloud ice water in CMIP3 and CMIP5 GCMs and  
1419 contemporary reanalyses using contemporary satellite data, *J. Geophys. Res.*, 117, D16105,  
1420 <https://doi.org/10.1029/2012JD017640>, 2012.

1421 Li, J.-L., Lee, S., Ma, H.-Y., Stephens, G., and Guan, B.: Assessment of the cloud liquid water from climate models  
1422 and reanalysis using satellite observations, *Terr. Atmos. Ocean. Sci.*, 29(6), 653-678,  
1423 <https://doi.org/10.3319/TAO.2018.07.04.01>, 2018.

1424 Mahoney, K.M.: The representation of cumulus convection in high-resolution simulations of the 2013 Colorado front  
1425 range flood, *Mon. Weather Rev.*, 144, 4265-4278, <https://doi.org/10.1175/MWR-D-16-0211.1>, 2016.

1426 Meehl, G.A., Delworth, T.L., Latiff, M., McAveney, B., Mitchell, J.F.B., Stouffer, R.J., and Taylor, K.E.: The WCRP  
1427 CMIP3 multimodel dataset: A new era in climate change research, *B. Am. Meteorol. Soc.*, 88, 1383-1394,  
1428 <https://doi.org/10.1175/BAMS-88-9-1383>, 2007.

1429 Minnis, P., and coauthors: CERES Edition-2 cloud property retrievals using TRMM VIRS and Terra and Aqua  
1430 MODIS data-Part I: Algorithms, *IEEE T. Geosci. Remote.*, Vol. 49, NO 11, 4374-4400,  
1431 <https://doi.org/10.1109/TGRS.2011.2144601>, 2011.

1432 Minnis, P., Kratz, D.P., Coakley, J.J.A., King, M.D., Garber, D., Heck, P., Mayor, S., Young, D.F., and Arduini, R.:  
1433 Cloud optical property retrieval (Subsystem 4.3), in *Clouds and the Earth's Radiant Energy System (CERES)*  
1434 *Algorithm Theoretical Basis Document*, Vol III, Clouds and Radiance Inversions (Subsystem 4), NASA RP  
1435 1376, edited by Science Team CERES, pp. 135-176, NASA, Washington D.C., 1995.

1436 Mlawer, E. J., Taubman, S. J., Brown, P. D., Iacono, M. J., and Clough, S. A.: Radiative transfer for inhomogeneous  
1437 atmospheres: RRTM, a validated correlated-k model for the longwave, *J. Geophys. Res.*, 102, 16663-16682,  
1438 <https://doi.org/10.1029/97JD00237>, 1997.

Deleted: non-hydrostatic

1440 Molod, A., Takacs, L., Suarez, M., Bacmeister, J., Song, I.-S., and Eichman, A.: The GEOS-5 atmospheric general  
1441 circulation model: Mean climate from MERRA to Fortuna, Technical Report Series on Global Modeling and  
1442 Assimilations, Vol. 28, 124 pp, 2012.

1443 Nakanishi, M., and Niino, H.: Development of an improved turbulence closure model for the atmospheric boundary  
1444 layer, *J. Meteor. Soc. Japan*, 87, 895–912, <https://doi.org/10.2151/jmsj.87.895>, 2009.

1445 Ogura, Y., and Cho, H.-R.: Diagnostic determination of cumulus cloud populations from observed large-scale  
1446 variables, *J. Atmos. Sci.*, 30, 1276-1286, [https://doi.org/10.1175/1520-  
1447 0469\(1973\)030<1276:DDOCCP>2.0.CO;2](https://doi.org/10.1175/1520-0469(1973)030<1276:DDOCCP>2.0.CO;2), 1973.

1448 Olson, J.B., Kenyon, J.S., Angevine, W.M., Brown, J.M., Pagowski, M., and Suselj, K.: A description of the MYNN-  
1449 EDMF scheme and the coupling to other components in WRF-ARW, NOAA Technical Memorandum OAR GSD,  
1450 61, pp 37, 2019.

1451 Platnick, S., King, M.D., Ackerman, S.A., Wenzel, W.P., Baum, B.A., Riedl, J.C., and Frey, R.A.: The MODIS cloud  
1452 products: Algorithms and examples from Terra, *IEEE T. Geosci. Remote*, 41, 459-473,  
1453 <https://doi.org/10.1109/TGRS.2002.808301>, 2003.

1454 Qiao, F., and Liang, X-Z: Effects of cumulus parameterization closures on the simulations of summer precipitation  
1455 over the United States coastal oceans, *J. Adv. Model. Earth Sy.*, 8, 764-785,  
1456 <https://doi.org/10.1002/2015MS000621>, 2015.

1457 Raymond, D.J.: Regulation of moist convection over the west Pacific warm pool, *J. Atmos. Sci.*, 52, 3945-3959,  
1458 [https://doi.org/10.1175/1520-0469\(1995\)052<3945:ROMCOT>2.0.CO;2](https://doi.org/10.1175/1520-0469(1995)052<3945:ROMCOT>2.0.CO;2), 1995.

1459 Schwarz, C.S.: Medium-range convection-allowing ensemble forecasts with a variable-resolution global model, *Mon.*  
1460 *Weather Rev.*, 147, 2997-3023, <https://doi.org/10.1175/MWR-D-18-0452.1>, 2019.

1461 Simpson, J., and Wiggert, V.: Models of precipitating cumulus towers, *Mon. Weather Rev.*, 97, 471-489,  
1462 [https://doi.org/10.1175/1520-0493\(1969\)097<0471:MOPCT>2.3.CO;2](https://doi.org/10.1175/1520-0493(1969)097<0471:MOPCT>2.3.CO;2), 1969.

1463 Skamarock, W.C., and Gassmann, A.: Conservative transport schemes for spherical geodesic grids: High-order flux  
1464 operators for ODE-based time integration, *Mon. Weather Rev.*, 139, 2962-2975, [https://doi.org/10.1175/MWR-  
1465 D-10-05056.1](https://doi.org/10.1175/MWR-D-10-05056.1), 2011.

1466 Skamarock, W.C., Klemp, J.B., Duda, M.G., Fowler, L.D., Park, S.-H., and Ringler, T.D.: A multiscale nonhydrostatic  
1467 atmospheric model using Centroidal Voronoi tessellations and C-grid staggering, *Mon. Weather Rev.*, 140, 3090-  
1468 3105, <https://doi.org/10.1175/MWR-D-11-00215.1>, 2012.

1469 Skamarock, W.C., and Coauthors: A description of the Advanced Research WRF version 3, NCAR Tech. Note  
1470 NCAR/TN-475+STR, 113 pp, 2008.

1471 Smagorinsky, J.: General circulation experiments with the primitive equations. I. The basic experiment, *Mon. Weather*  
1472 *Rev.*, 91, 99-164, [https://doi.org/10.1175/1520-0493\(1963\)091<0099:GCEWTP>2.3.CO;2](https://doi.org/10.1175/1520-0493(1963)091<0099:GCEWTP>2.3.CO;2), 1963.

1473 Stanfield, R.E., Dong, X., Xi, B., Del Genio, A.D., Minnis, P., Doelling, D., and Loeb, N.: Assessment of NASA  
1474 GISS CMIP5 and Post-CMIP5 simulated clouds and TOA radiation budgets using satellite observations. Part II:  
1475 TOA radiation budget and CREs, *J. Climate*, 28, 1842-1863, <https://doi.org/10.1175/JCLI-D-14-00249.1>, 2015.

1476 Stephens, G.L., and Kummerow, C.D.: The remote sensing of clouds and precipitation from space: A review, *J. Atmos.*  
1477 *Sci.*, 64, 3742-3765, <https://doi.org/10.1175/2006JAS2375.1>, 2007.

1478 Stephens, G.L., Vane, D.G., Boain, R.J., Mace, G.G., Sassen, K., Wang, Z., Illingworth, A.J., O'Connor, E.J., Rossow,  
1479 W.B., Durden, S.L., Miller, S.D., Austin, R.T., Benedetti, A., Mitrescu, C., and the CloudSat Science Team: The  
1480 CloudSat mission and the A-Train: A new dimension and space-based observations of clouds and precipitation,  
1481 *B. Am. Meteorol. Soc.*, 83, 1771-1790, <https://doi.org/10.1175/BAMS-83-12-1771>, 2002.

1482 Storer, R.L., Griffin, B.M., Hoft, J., Weber, J.K., Raut, E., Larson, V.E., Wang, M., and Rasch, P.J.: Parameterizing  
1483 deep convection using the assumed probability density function method, *Geosci. Model Dev.*, 8, 1-19,  
1484 <https://doi.org/10.5194/gmd-8-1-2015>, 2015.

1485 Suhas, E., and Zhang, Q.J.: Evaluation of trigger functions for convective parameterization schemes using  
1486 observations, *J. Climate*, 27, 7647-7666, <https://doi.org/10.1175/JCLI-D-13-00718.1>, 2014.

1487 Taylor, K.E., Stouffer, R.J., and Meehl, G.A.: An overview of CMIP5 and the experiment design, *B. Am. Meteorol.*  
1488 *Soc.*, 93, 485-4398, <https://doi.org/10.1175/BAMS-D-11-00094.1>, 2012.

1489 Thayer-Calder, K., Gettelman, A., Craig, C., Goldhaber, S., Bogenschutz, P.A., Chen, C.-C., Morrison, H., Höft, J.,  
1490 Raut, E., Griffin, B.M., Weber, J.K., Larson, V.E., Wyant, M.C., M. Wang, Guo, Z., and Ghan, S.J.: A unified  
1491 parameterization of clouds and turbulence using CLUBB and subcolumns in the Community Atmosphere Model,  
1492 *Geosci. Model Dev.*, 8, 3801-3821, <https://doi.org/10.5194/gmd-8-3801-2015>, 2015.

1493 Thompson, G., Field, P.R., Rasmussen, R.M., and Hall, W.D.: Explicit forecasts of winter precipitation using an  
1494 improved bulk cloud microphysics scheme. Part II: Implementation of a new snow parameterization, *Mon.*  
1495 *Weather Rev.*, 136, 5095-5115, <https://doi.org/10.1175/2008MWR2387.1>, 2008.

1496 Thompson, G., Rasmussen, R.M., and Manning, K.: Explicit forecasts of winter precipitation using an improved bulk  
1497 cloud microphysics scheme. Part I: Description and sensitivity analysis, *Mon. Weather Rev.*, 132, 519-542,  
1498 [https://doi.org/10.1175/1520-0493\(2004\)132<0519:EFOWPU>2.0.CO;2](https://doi.org/10.1175/1520-0493(2004)132<0519:EFOWPU>2.0.CO;2), 2004.

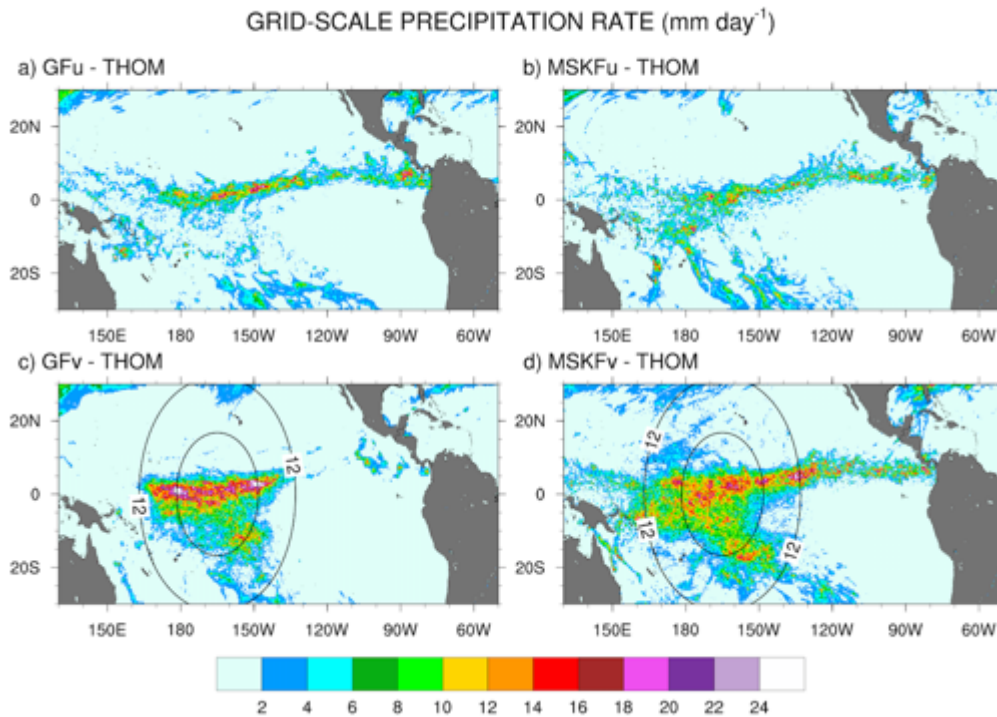
1499 Thompson, G., Tewari, M., Ikeda, K., Tessendorf, S., Weeks, C., Otkin, J., and Kong, F.: Explicitly-coupled cloud  
1500 physics and radiation parameterizations and subsequent evaluation in WRF high-resolution convective forecasts,  
1501 *Atmos. Res.*, 168, 92-104, <https://doi.org/10.1016/j.atmosres.2015.09.005>, 2016.

1502 Tokioka, T., Yamazaki, K., Kotoh, A., and Ose, T.: The equatorial 30-60 day oscillation and the Arakawa-Schubert  
1503 penetrative cumulus parameterization, *J. Meteor. Soc. Japan*, 66, 883-900,  
1504 <https://doi.org/10.2151/jmsj1965.66.6.883>, 1988.

1505 Waliser, D.E., Li, J.-L., Woods, C.P., Austin, R.T., Bacmeister, J., Chern, J., Del Genio, A., Jiang, J.H., Juang, Z.,  
1506 Meng, H., Minnis, P., Platnick, S., Rossow, W.B., Stephens, G.L., Sun-Mack, S., Tao, W.-K., Tompkins, A.M.,

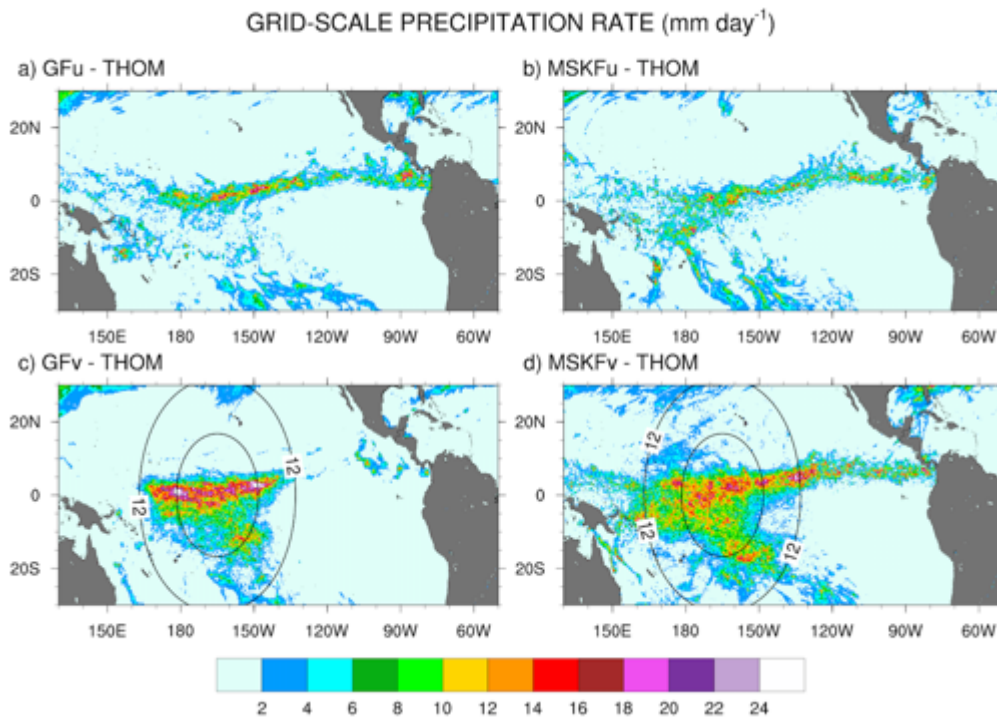
- 1507 Vane, D.G., Walker, C., and Wu, D.: Cloud ice: A climate model challenge with signs and expectations of  
1508 progress, *J. Geophys. Res.*, 114, D00A21, <https://doi.org/10.1029/2008JD010015>, 2009.
- 1509 Wicker, L.J., and W.C. Skamarock: Time-splitting methods for elastic models using forward time schemes, *Mon.*  
1510 *Weather Rev.*, 130, 2088-2097, [https://doi.org/10.1175/1520-0493\(2002\)130<2088:TSMFEM>2.0.CO;2](https://doi.org/10.1175/1520-0493(2002)130<2088:TSMFEM>2.0.CO;2), 2002.
- 1511 Wielicki, B.A., Barkstrom, B.R., Harrison, E.F., Lee III, R.B., Smith, G.L., and Cooper, J.E.: Clouds and the Earth's  
1512 Radiation Energy System (CERES): An Earth Observing System experiment, *B. Am. Meteorol. Soc.*, 77, 853-  
1513 868, [https://doi.org/10.1175/1520-0477\(1996\)077<0853:CATERE>2.0.CO;2](https://doi.org/10.1175/1520-0477(1996)077<0853:CATERE>2.0.CO;2), 1996.
- 1514 Wong, M., and Skamarock, W.C.: Spectral characteristics of convective-scale precipitation observations and forecasts,  
1515 *Mon. Weather Rev.*, 144, 4183-4195, <https://doi.org/10.1175/MWR-D-16-0183.1>, 2016.
- 1516 Xu, K.-M. and Krueger, S.K.: Evaluation of cloudiness parameterizations using a cumulus ensemble model, *Mon.*  
1517 *Weather Rev.*, 119, 342-367, [https://doi.org/10.1175/1520-0493\(1991\)119<0342:EOCPUA>2.0.CO;2](https://doi.org/10.1175/1520-0493(1991)119<0342:EOCPUA>2.0.CO;2), 1991.
- 1518 Xu, K.-M., and Randall, D. A.: A semi-empirical cloudiness parameterization for use in climate models, *J. Atmos.*  
1519 *Sci.*, 53, 3084–3102, [https://doi.org/10.1175/1520-0469\(1996\)053<3084:ASCPFU>2.0.CO;2](https://doi.org/10.1175/1520-0469(1996)053<3084:ASCPFU>2.0.CO;2), 1996.
- 1520 Zheng, Y., Alapaty, K., Herwehe, J. A., Del Genio, A.D., and Niyogi, D.: Improving high-resolution weather forecasts  
1521 using the Weather Research and Forecasting (WRF) model with an updated Kain-Fritsch scheme, *Mon. Weather*  
1522 *Rev.*, 144, 833-860, <https://doi.org/10.1175/MWR-D-15-0005.1>, 2016.

1	<b>Page 18: [1] Deleted</b>	<b>Laura Fowler</b>	<b>3/6/20 10:45:00 AM</b>
2	over		
3			
4	<b>Page 18: [1] Deleted</b>	<b>Laura Fowler</b>	<b>3/6/20 10:45:00 AM</b>
5	over		
6			
7	<b>Page 18: [1] Deleted</b>	<b>Laura Fowler</b>	<b>3/6/20 10:45:00 AM</b>
8	over		
9			
10	<b>Page 18: [2] Deleted</b>	<b>Laura Fowler</b>	<b>3/6/20 10:45:00 AM</b>
11			
12			
13	<b>Page 18: [2] Deleted</b>	<b>Laura Fowler</b>	<b>3/6/20 10:45:00 AM</b>
14			
15			
16	<b>Page 18: [2] Deleted</b>	<b>Laura Fowler</b>	<b>3/6/20 10:45:00 AM</b>
17			
18			
19	<b>Page 18: [2] Deleted</b>	<b>Laura Fowler</b>	<b>3/6/20 10:45:00 AM</b>
20			
21			
22	<b>Page 18: [2] Deleted</b>	<b>Laura Fowler</b>	<b>3/6/20 10:45:00 AM</b>
23			
24			
25	<b>Page 18: [2] Deleted</b>	<b>Laura Fowler</b>	<b>3/6/20 10:45:00 AM</b>
26			
27			
28	<b>Page 18: [2] Deleted</b>	<b>Laura Fowler</b>	<b>3/6/20 10:45:00 AM</b>
29			
30			
31	<b>Page 18: [2] Deleted</b>	<b>Laura Fowler</b>	<b>3/6/20 10:45:00 AM</b>
32			
33			
34	<b>Page 18: [2] Deleted</b>	<b>Laura Fowler</b>	<b>3/6/20 10:45:00 AM</b>
35			
36			
37	<b>Page 21: [3] Deleted</b>	<b>Laura Fowler</b>	<b>3/6/20 10:45:00 AM</b>
38	) and		
39			
40	<b>Page 21: [3] Deleted</b>	<b>Laura Fowler</b>	<b>3/6/20 10:45:00 AM</b>
41	) and		
42			
43	<b>Page 21: [4] Deleted</b>	<b>Laura Fowler</b>	<b>3/6/20 10:45:00 AM</b>



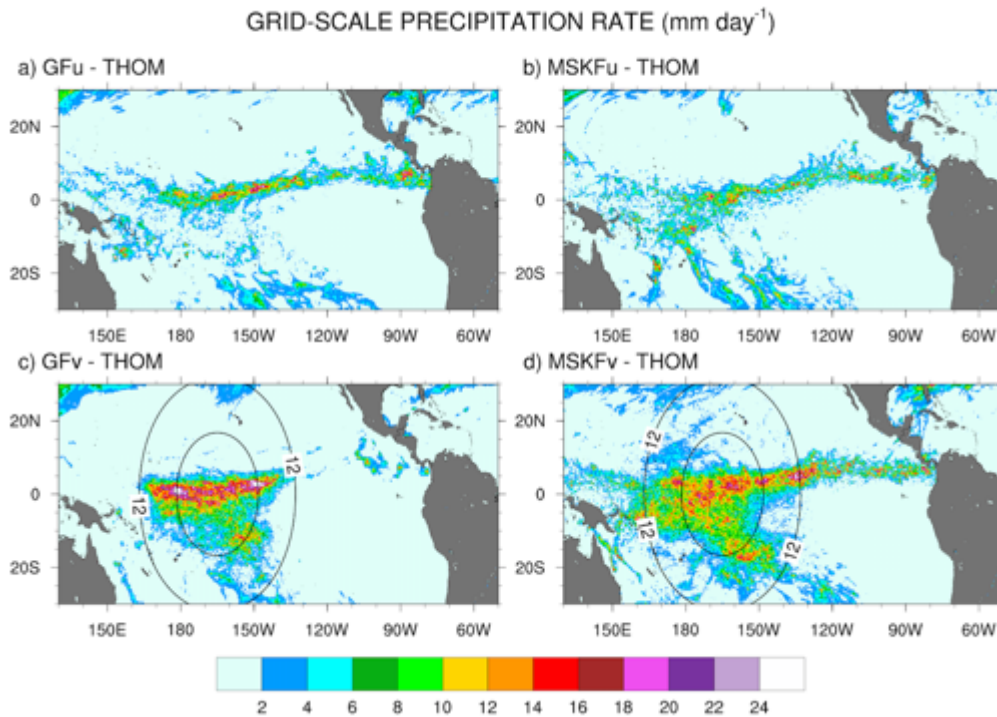
44  
45  
46  
47

Figure 9: As Fig. 8, but the monthly mean grid-scale (THOM) precipitation rate.



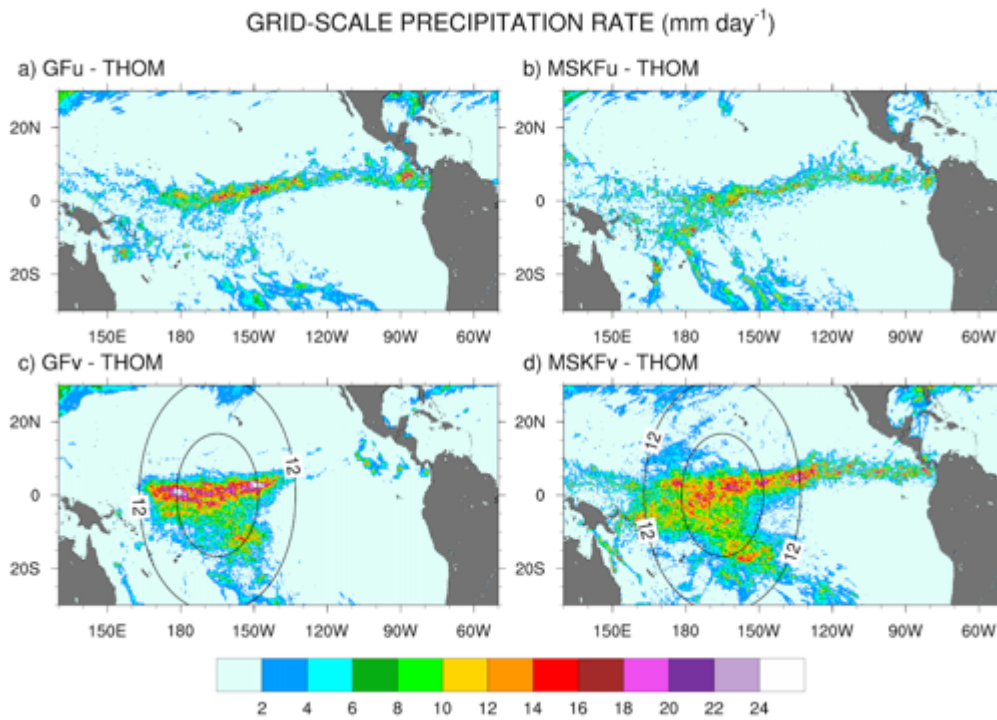
48  
49  
50  
51

Figure 9: As Fig. 8, but the monthly mean grid-scale (THOM) precipitation rate.



52  
53  
54  
55

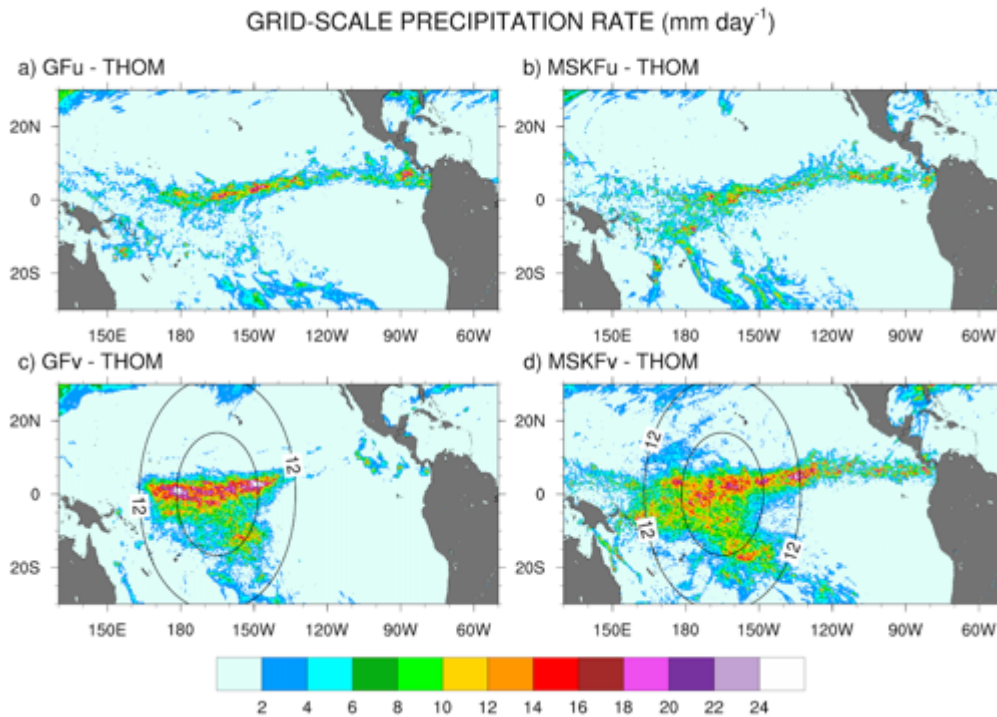
Figure 9: As Fig. 8, but the monthly mean grid-scale (THOM) precipitation rate.



56  
57  
58  
59

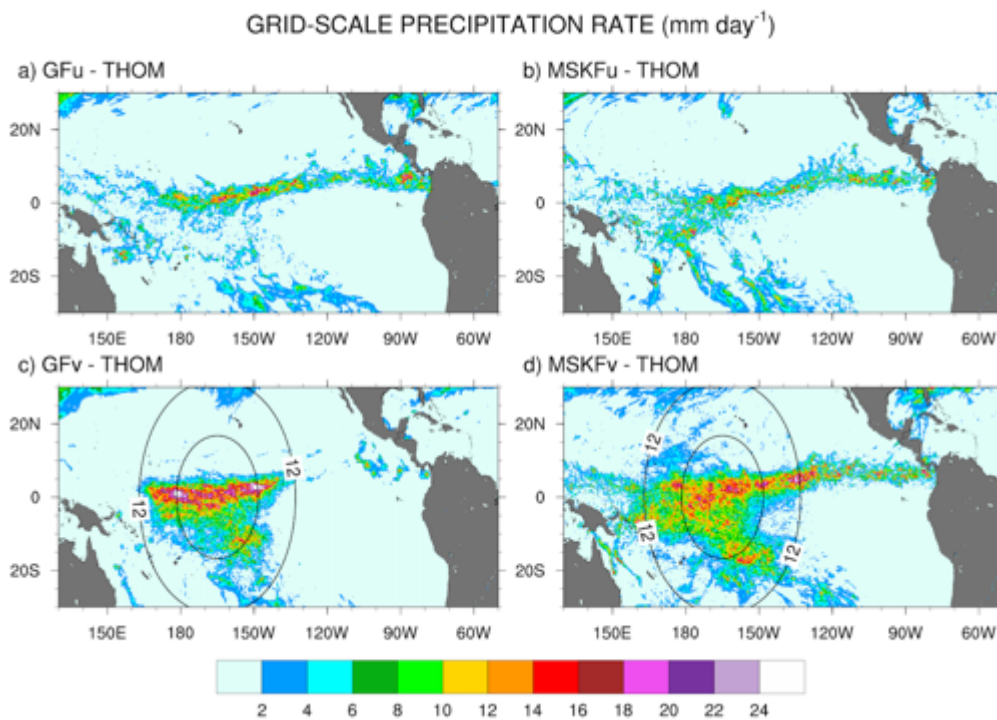
Figure 9: As Fig. 8, but the monthly mean grid-scale (THOM) precipitation rate.





60  
61  
62  
63

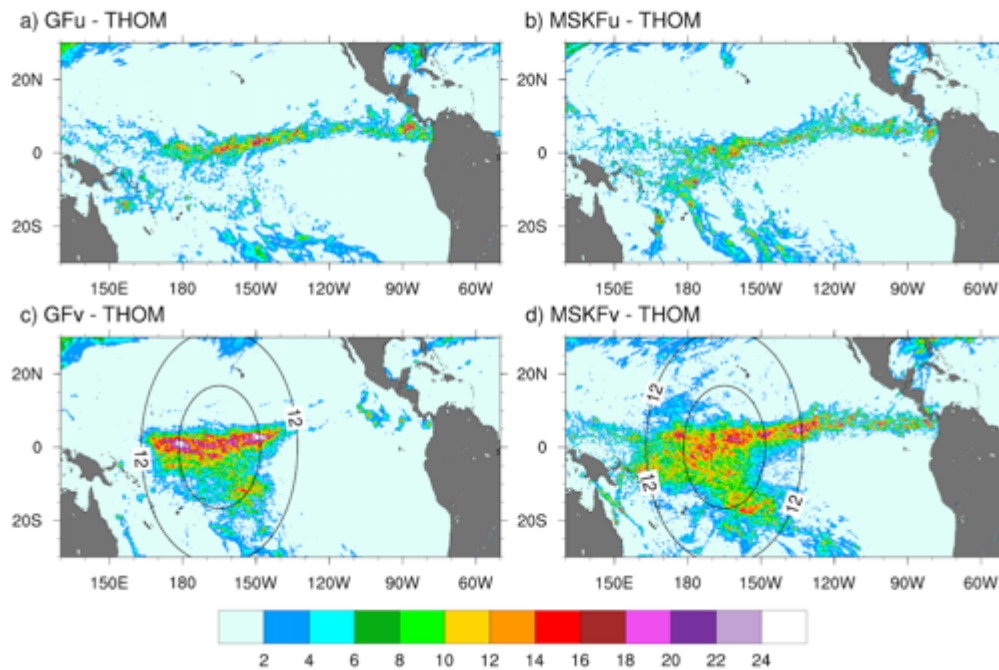
Figure 9: As Fig. 8, but the monthly mean grid-scale (THOM) precipitation rate.



64  
65  
66  
67

Figure 9: As Fig. 8, but the monthly mean grid-scale (THOM) precipitation rate.

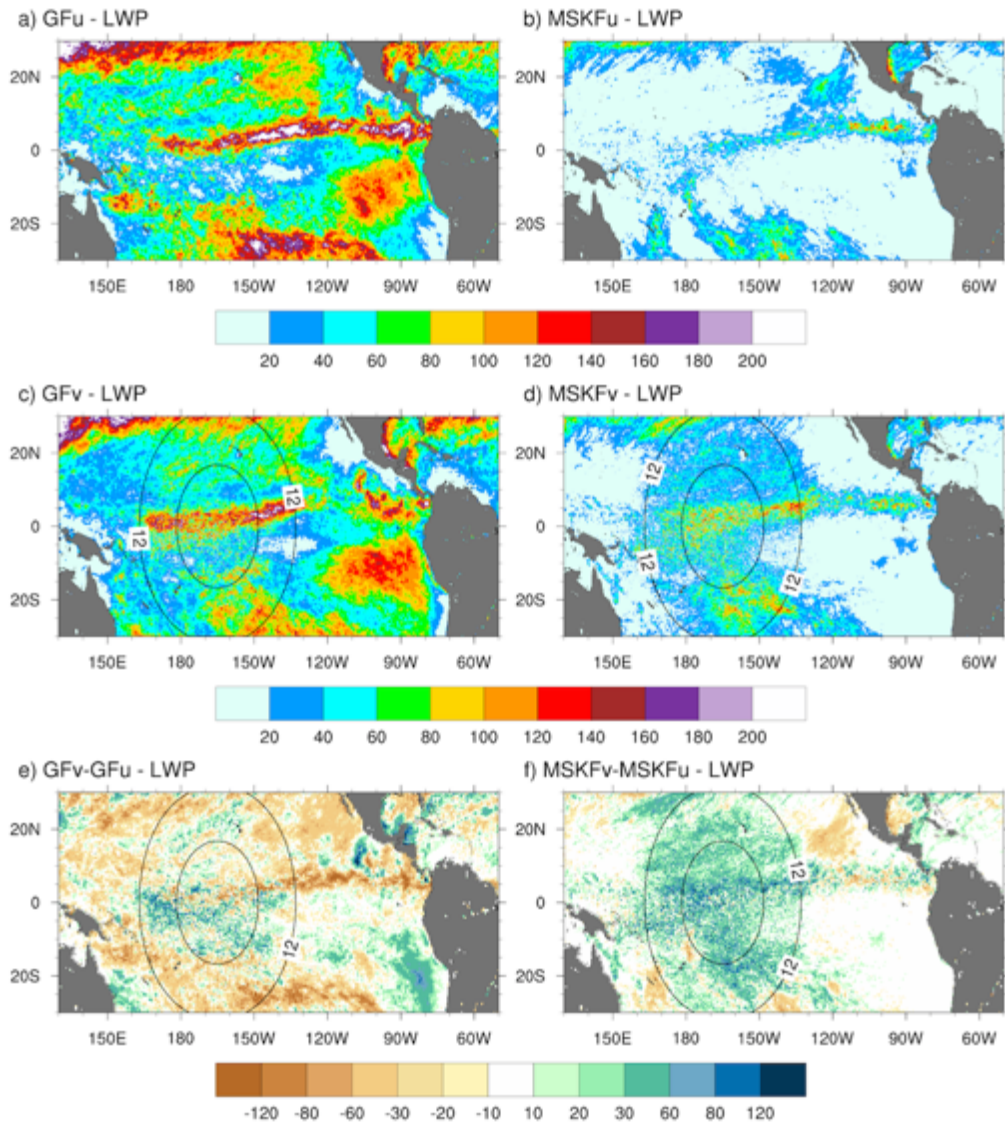
GRID-SCALE PRECIPITATION RATE (mm day<sup>-1</sup>)



68  
69  
70  
71  
72

**Figure 9:** As Fig. 8, but the monthly mean grid-scale (THOM) precipitation rate.

CLOUD LIQUID WATER PATH ( $\text{g m}^{-2}$ )



**Page 28: [6] Deleted** **Laura Fowler** **3/6/20 10:45:00 AM**

calculate

**Page 28: [6] Deleted** **Laura Fowler** **3/6/20 10:45:00 AM**

calculate

**Page 28: [6] Deleted** **Laura Fowler** **3/6/20 10:45:00 AM**

calculate

**Page 28: [6] Deleted** **Laura Fowler** **3/6/20 10:45:00 AM**

calculate

**Page 28: [6] Deleted** **Laura Fowler** **3/6/20 10:45:00 AM**

calculate

calculate

calculate

calculate

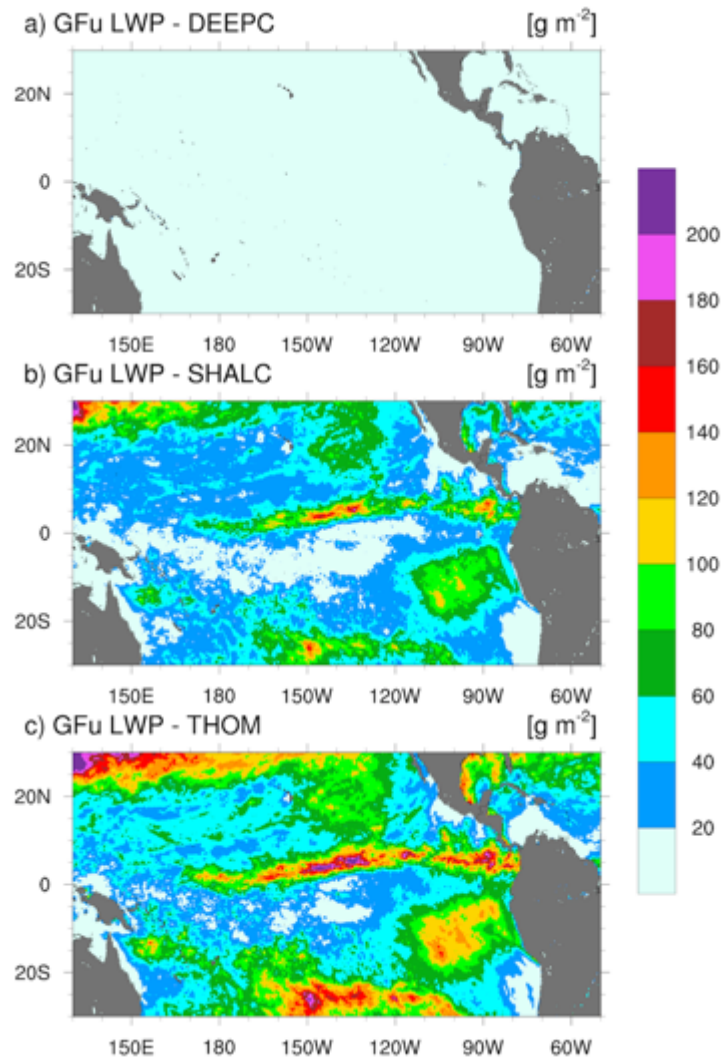
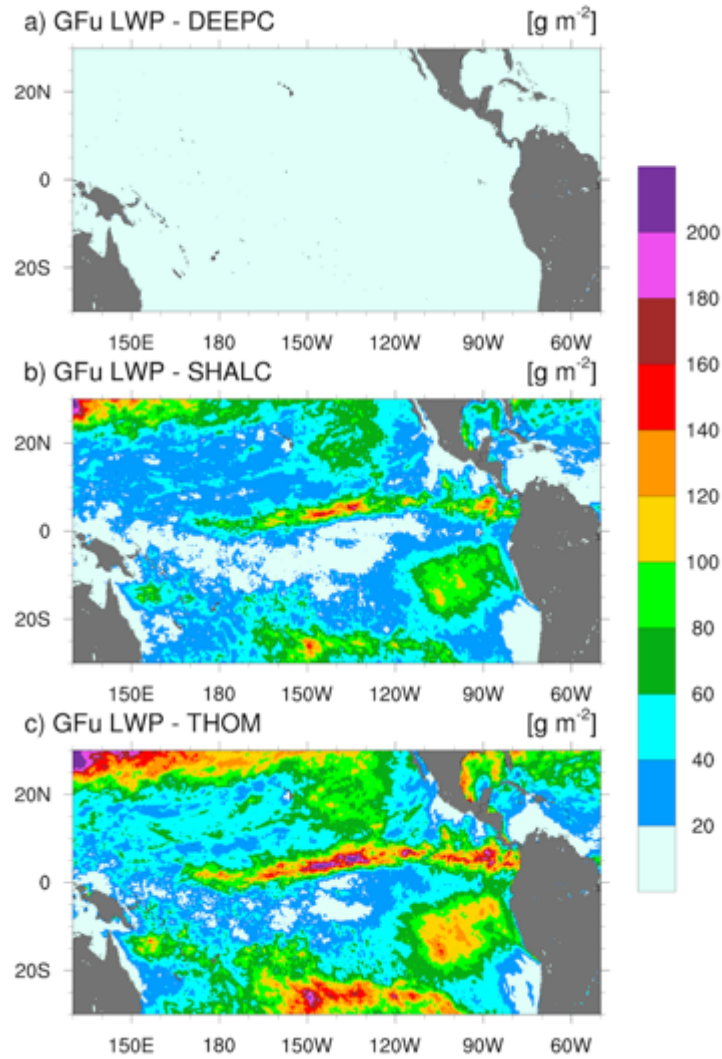
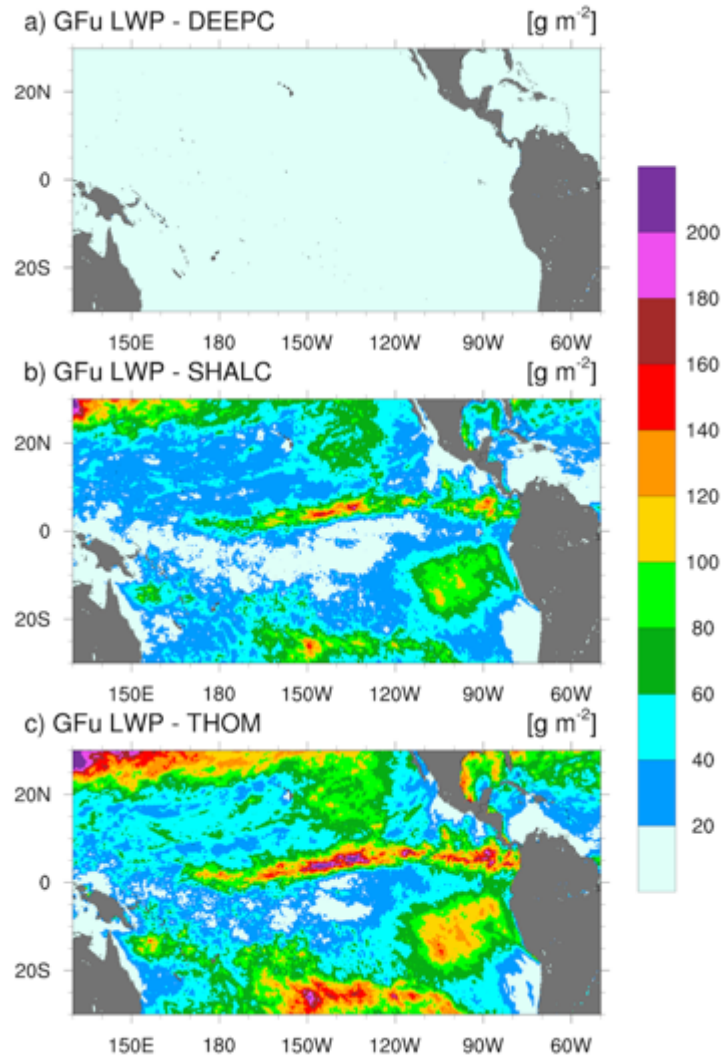


Figure 15: Monthly-mean of cloud liquid water path of corresponding to a) deep convection only (DEEPC); b) shallow convection only (SHALC); and c) no convection (THOM) simulated with GFu over the Tropical Pacific Ocean for December 2015.



**Figure 15:** Monthly-mean of cloud liquid water path of corresponding to a) deep convection only (DEEPC); b) shallow convection only (SHALC); and c) no convection (THOM) simulated with GFu over the Tropical Pacific Ocean for December 2015.



**Figure 15:** Monthly-mean of cloud liquid water path of corresponding to a) deep convection only (DEEPC); b) shallow convection only (SHALC); and c) no convection (THOM) simulated with GFu over the Tropical Pacific Ocean for December 2015.

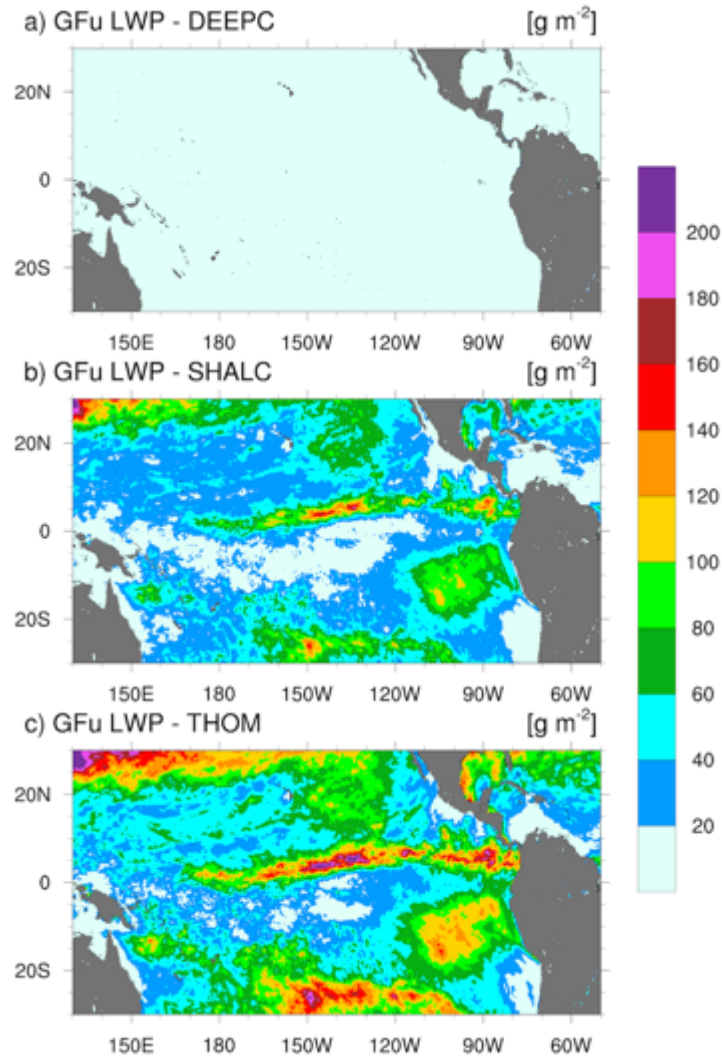


**Figure 15:** Monthly-mean of cloud liquid water path of corresponding to a) deep convection only (DEEPC); b) shallow convection only (SHALC); and c) no convection (THOM) simulated with GFu over the Tropical Pacific Ocean for December 2015.

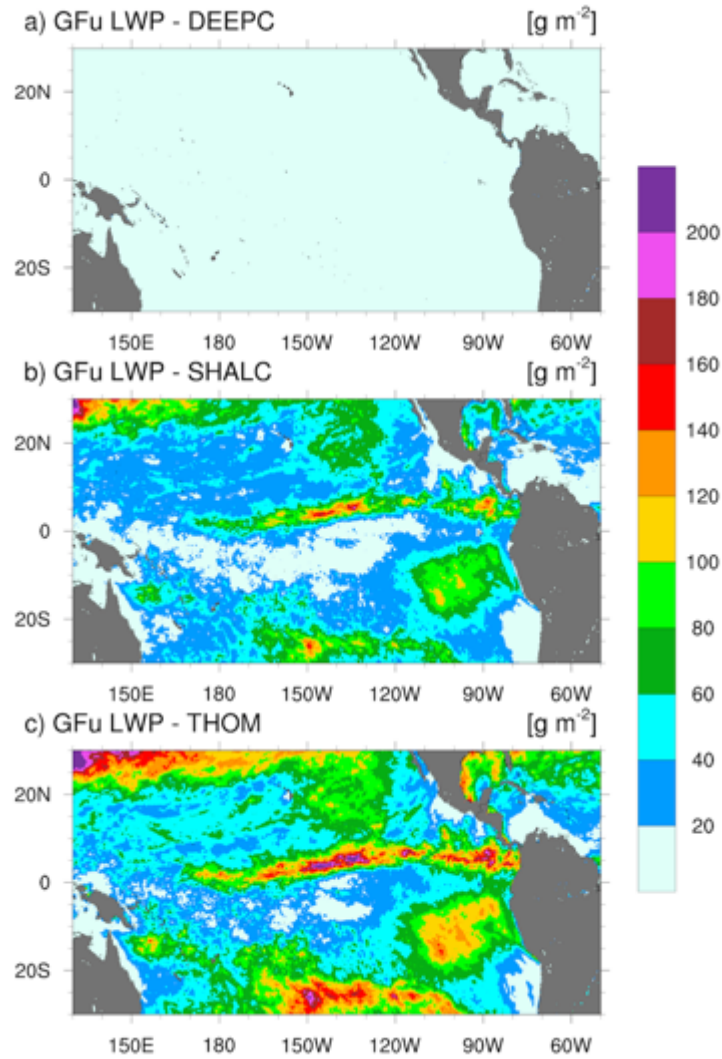


**Figure 15:** Monthly-mean of cloud liquid water path of corresponding to a) deep convection only (DEEPC); b) shallow convection only (SHALC); and c) no convection (THOM) simulated with GFu over the Tropical Pacific Ocean for December 2015.



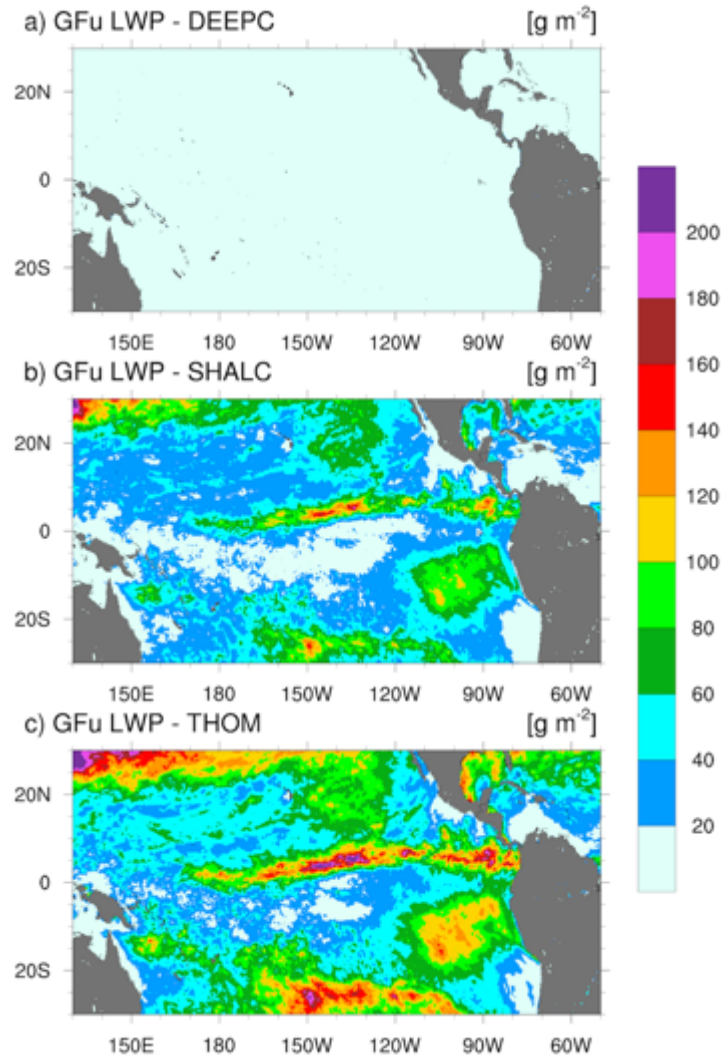


**Figure 15:** Monthly-mean of cloud liquid water path of corresponding to a) deep convection only (DEEPC); b) shallow convection only (SHALC); and c) no convection (THOM) simulated with GFu over the Tropical Pacific Ocean for December 2015.

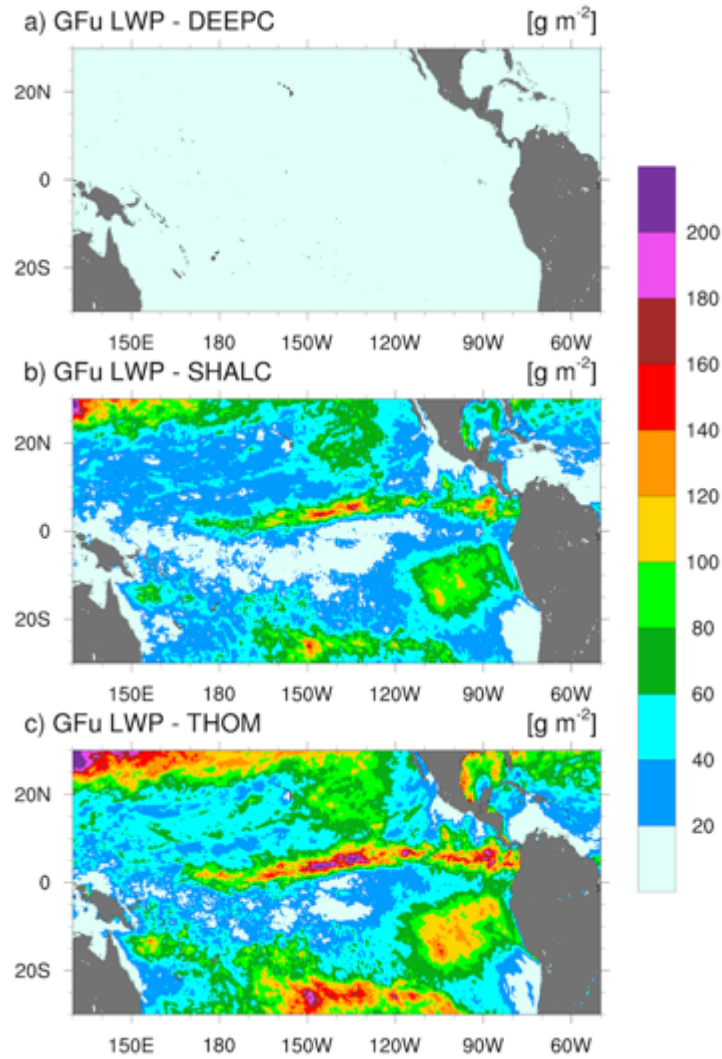


**Figure 15:** Monthly-mean of cloud liquid water path of corresponding to a) deep convection only (DEEPC); b) shallow convection only (SHALC); and c) no convection (THOM) simulated with GFu over the Tropical Pacific Ocean for December 2015.

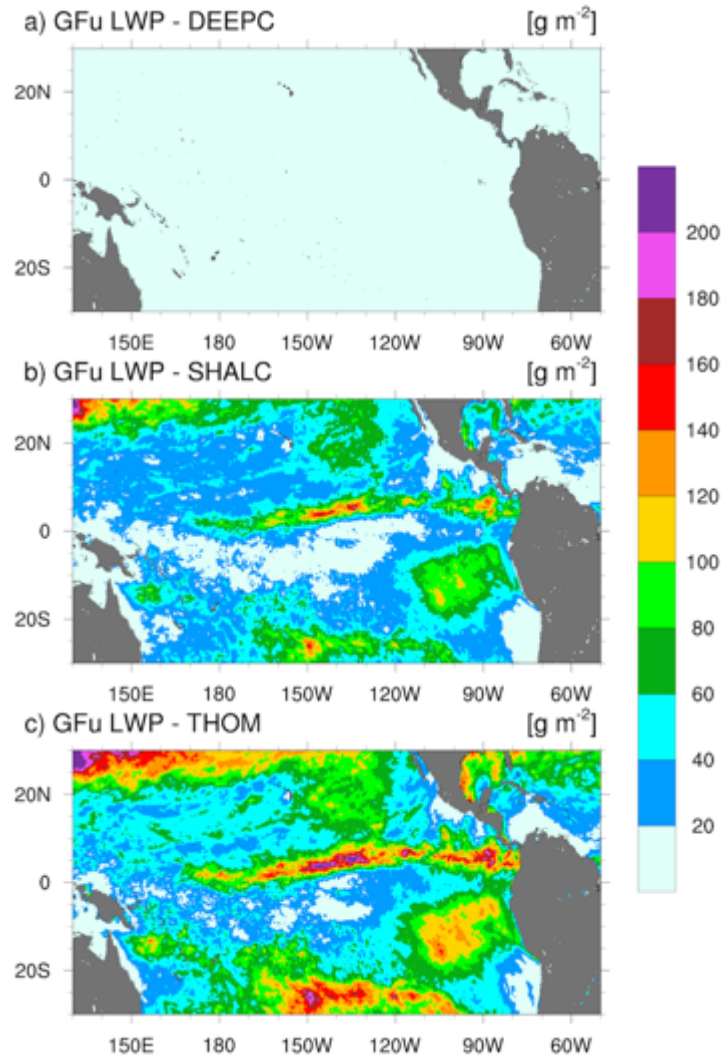


**Figure 15:** Monthly-mean of cloud liquid water path of corresponding to a) deep convection only (DEEPC); b) shallow convection only (SHALC); and c) no convection (THOM) simulated with GFu over the Tropical Pacific Ocean for December 2015.

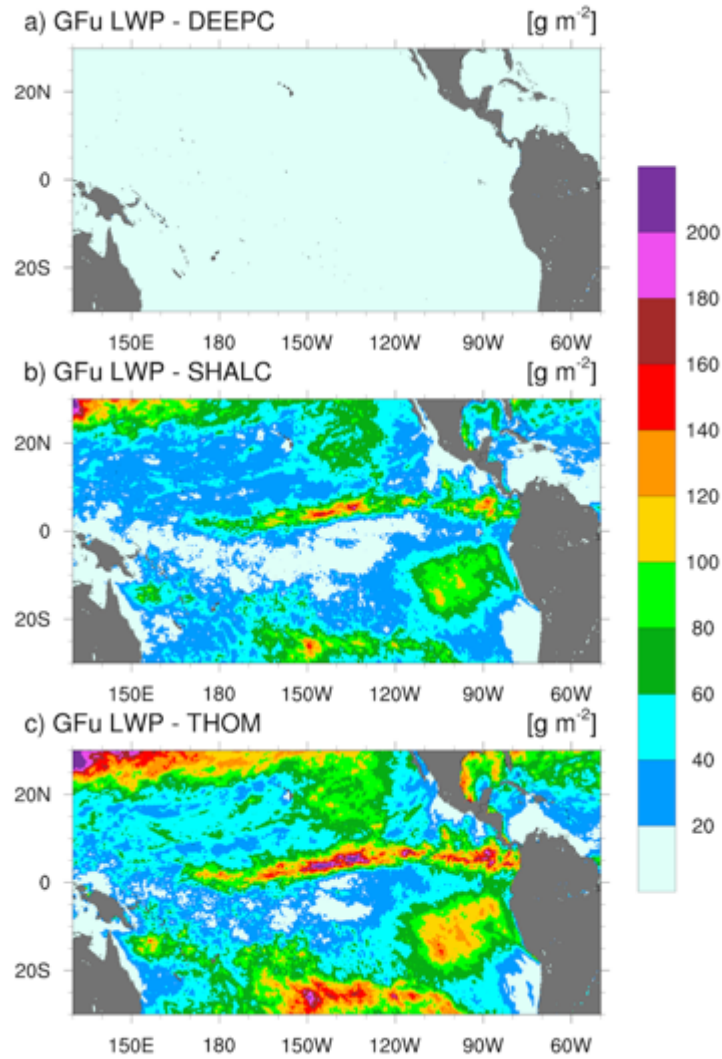


**Figure 15:** Monthly-mean of cloud liquid water path of corresponding to a) deep convection only (DEEPC); b) shallow convection only (SHALC); and c) no convection (THOM) simulated with GFu over the Tropical Pacific Ocean for December 2015.

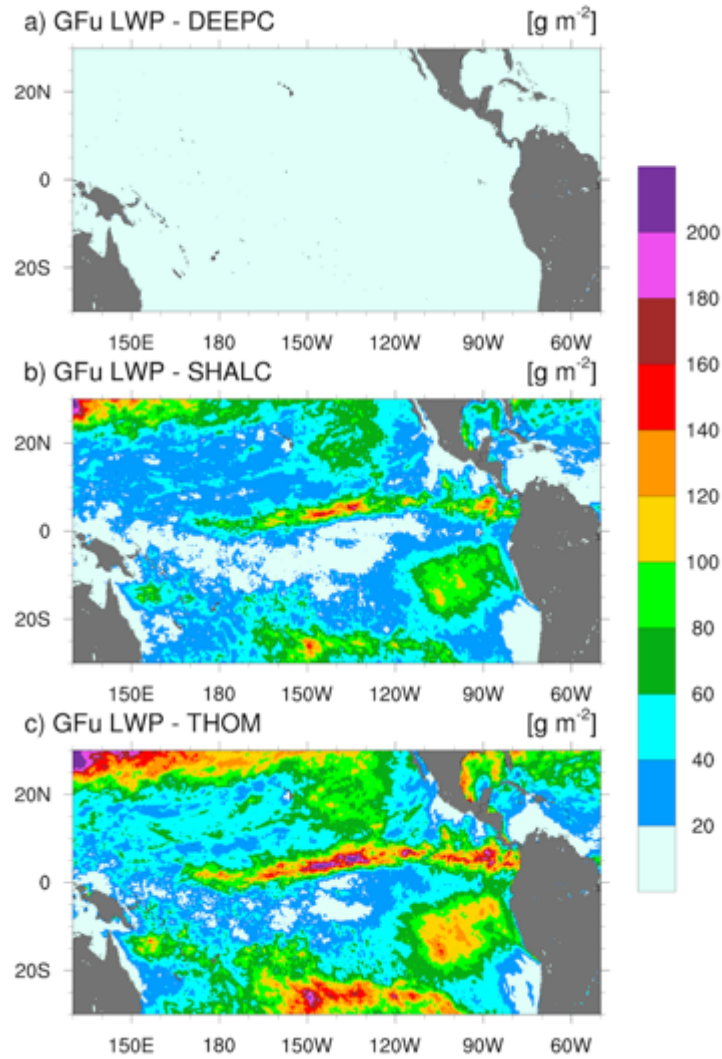


**Figure 15:** Monthly-mean of cloud liquid water path of corresponding to a) deep convection only (DEEPC); b) shallow convection only (SHALC); and c) no convection (THOM) simulated with GFu over the Tropical Pacific Ocean for December 2015.

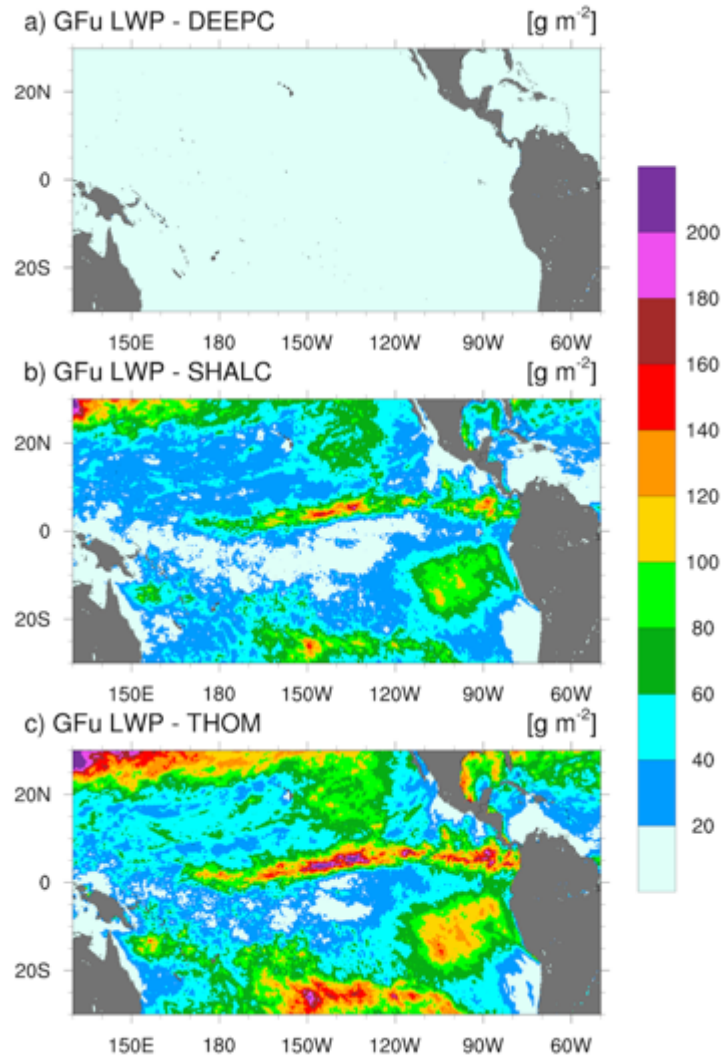


**Figure 15:** Monthly-mean of cloud liquid water path of corresponding to a) deep convection only (DEEPC); b) shallow convection only (SHALC); and c) no convection (THOM) simulated with GFu over the Tropical Pacific Ocean for December 2015.

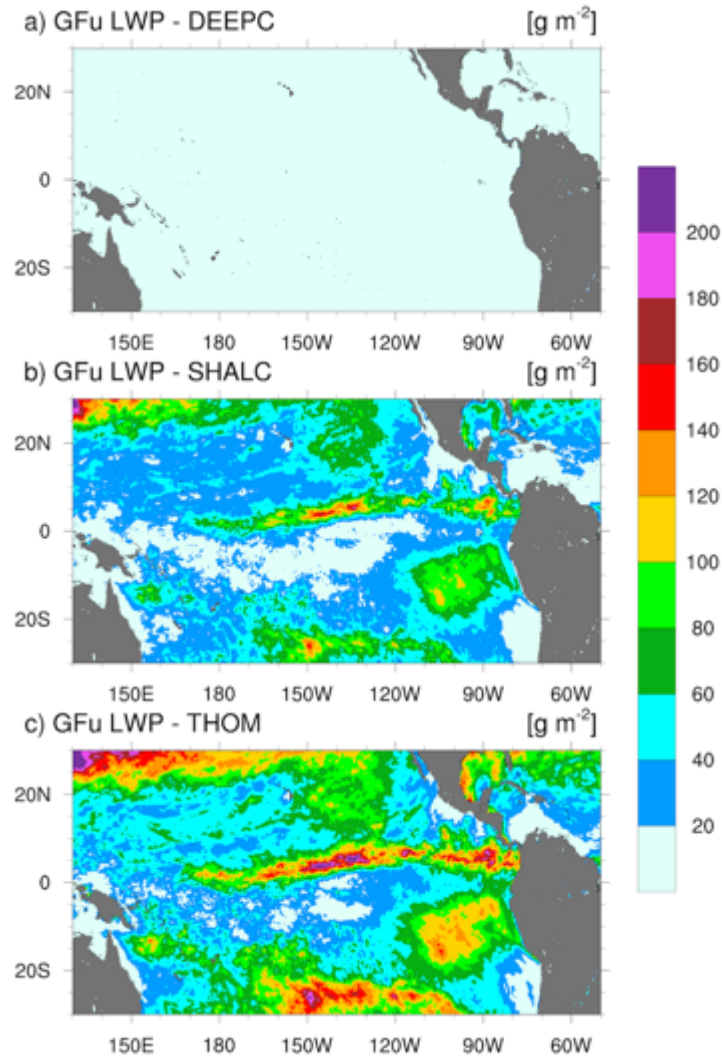


**Figure 15:** Monthly-mean of cloud liquid water path of corresponding to a) deep convection only (DEEPC); b) shallow convection only (SHALC); and c) no convection (THOM) simulated with GFu over the Tropical Pacific Ocean for December 2015.

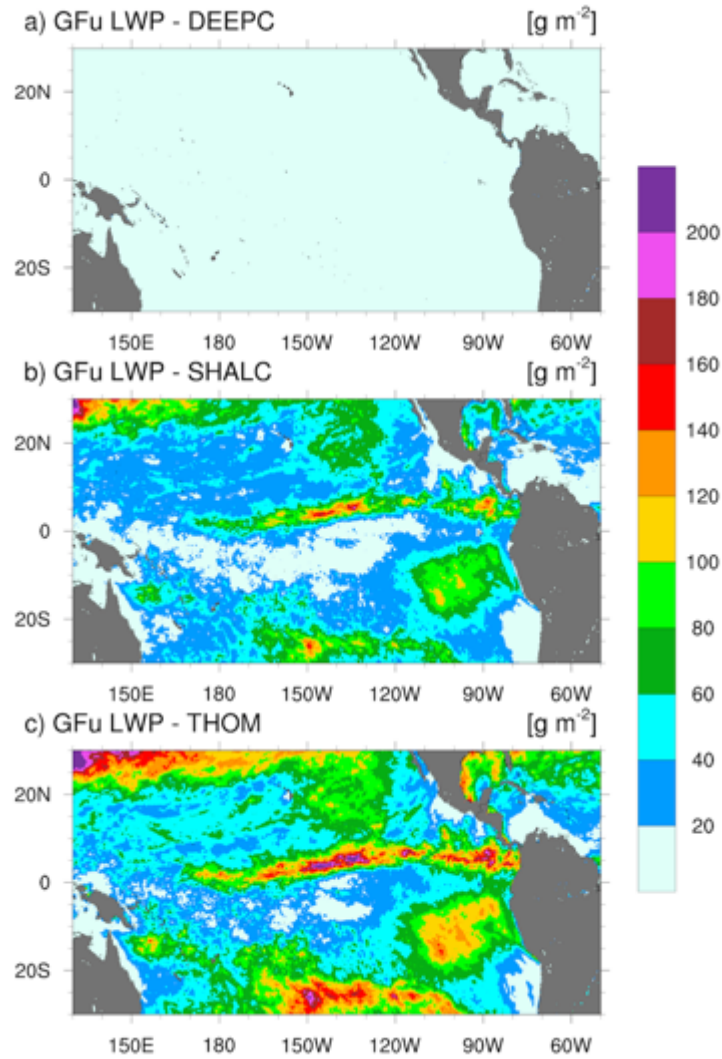


**Figure 15:** Monthly-mean of cloud liquid water path of corresponding to a) deep convection only (DEEPC); b) shallow convection only (SHALC); and c) no convection (THOM) simulated with GFu over the Tropical Pacific Ocean for December 2015.



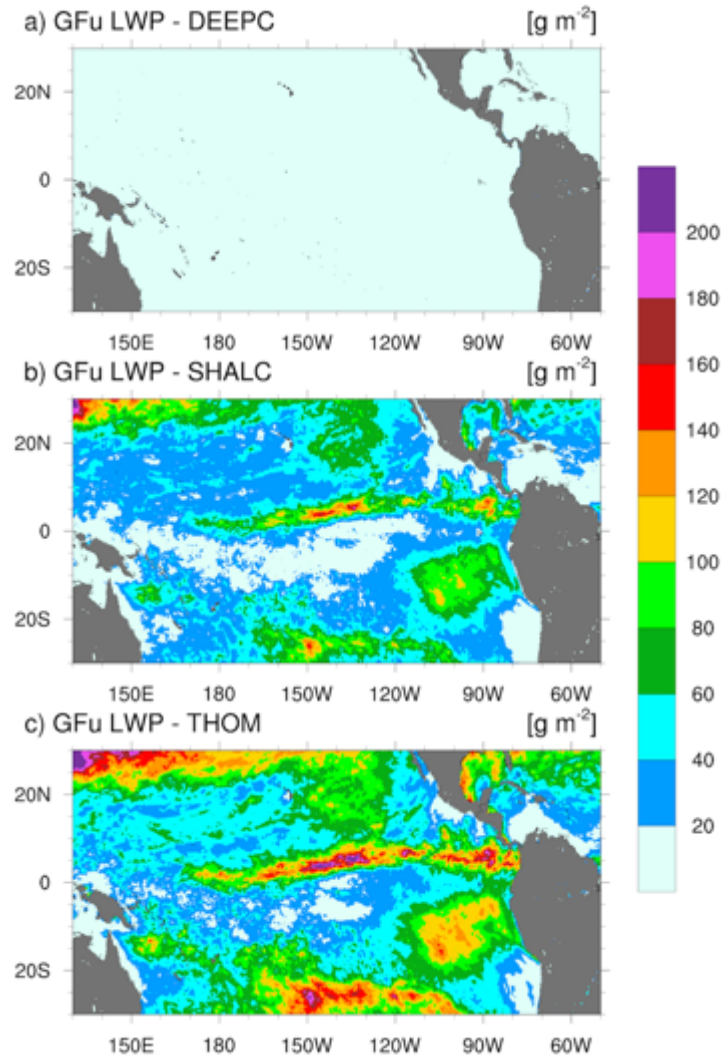


**Figure 15:** Monthly-mean of cloud liquid water path of corresponding to a) deep convection only (DEEPC); b) shallow convection only (SHALC); and c) no convection (THOM) simulated with GFu over the Tropical Pacific Ocean for December 2015.

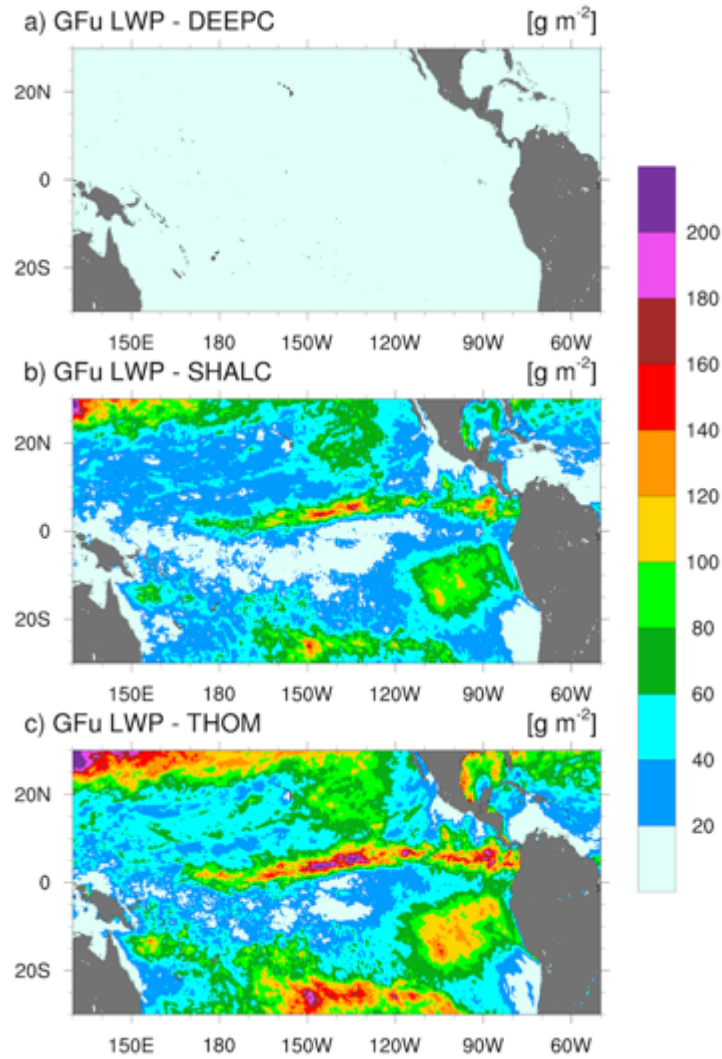


**Figure 15:** Monthly-mean of cloud liquid water path of corresponding to a) deep convection only (DEEPC); b) shallow convection only (SHALC); and c) no convection (THOM) simulated with GFu over the Tropical Pacific Ocean for December 2015.

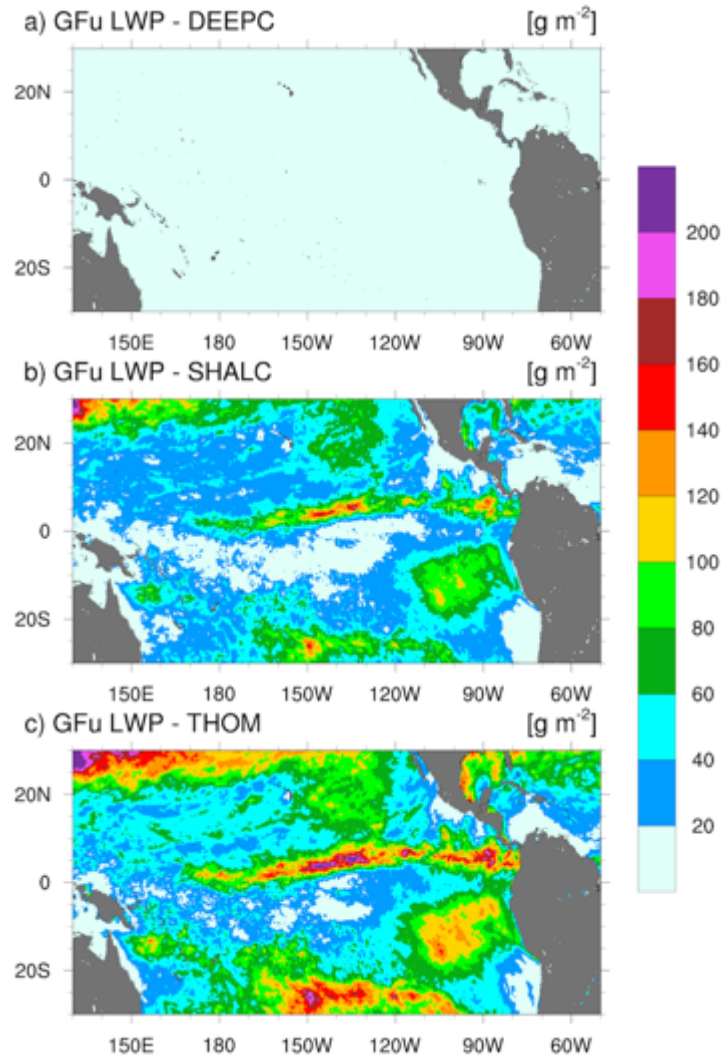


**Figure 15:** Monthly-mean of cloud liquid water path of corresponding to a) deep convection only (DEEPC); b) shallow convection only (SHALC); and c) no convection (THOM) simulated with GFu over the Tropical Pacific Ocean for December 2015.

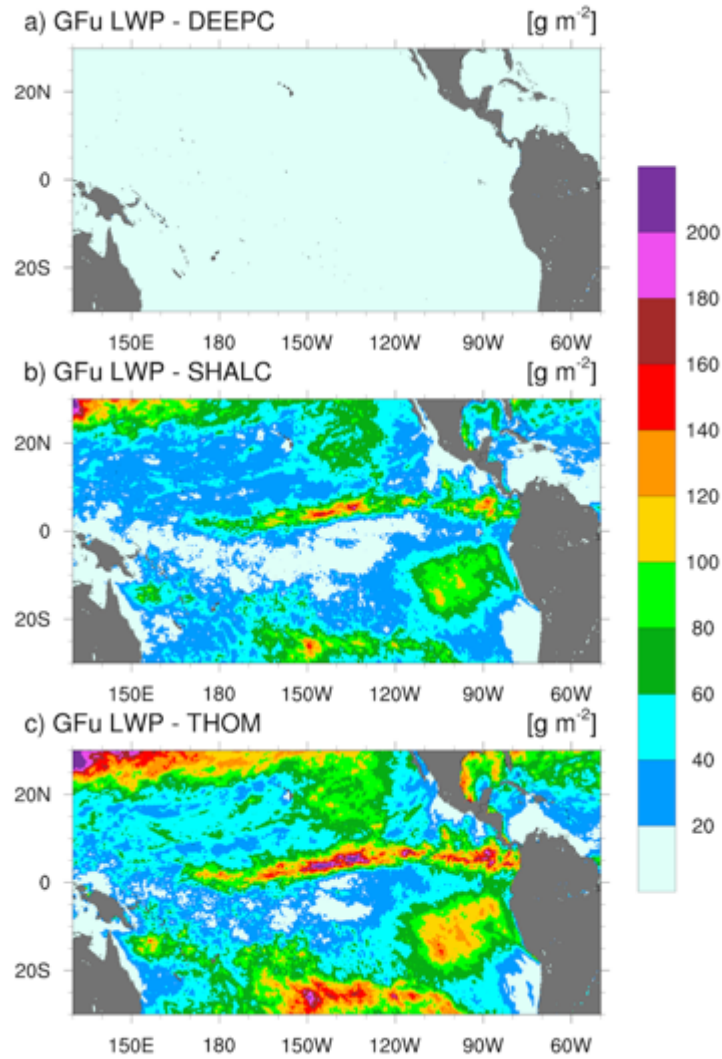


**Figure 15:** Monthly-mean of cloud liquid water path of corresponding to a) deep convection only (DEEPC); b) shallow convection only (SHALC); and c) no convection (THOM) simulated with GFu over the Tropical Pacific Ocean for December 2015.

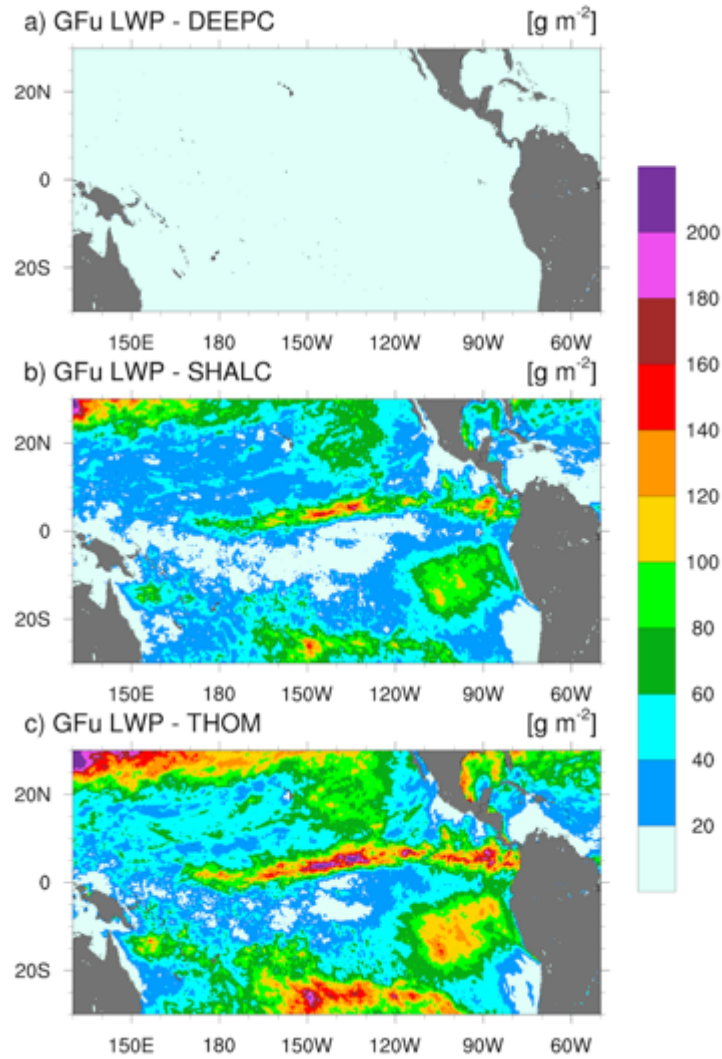


**Figure 15:** Monthly-mean of cloud liquid water path of corresponding to a) deep convection only (DEEPC); b) shallow convection only (SHALC); and c) no convection (THOM) simulated with GFu over the Tropical Pacific Ocean for December 2015.

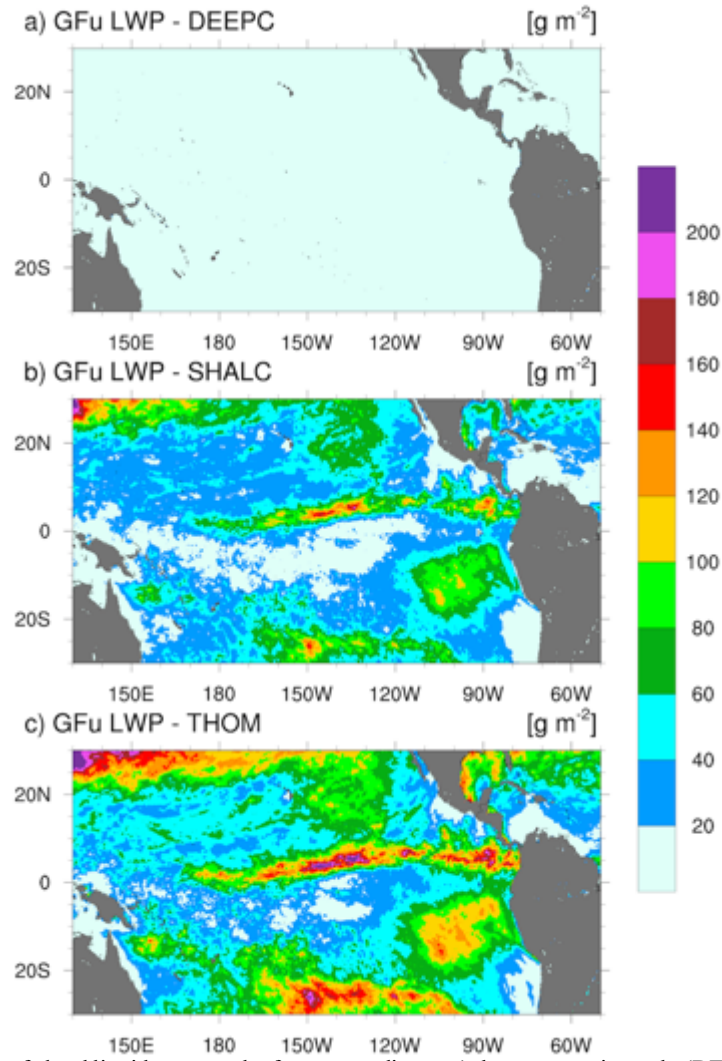


**Figure 15:** Monthly-mean of cloud liquid water path of corresponding to a) deep convection only (DEEPC); b) shallow convection only (SHALC); and c) no convection (THOM) simulated with GFu over the Tropical Pacific Ocean for December 2015.

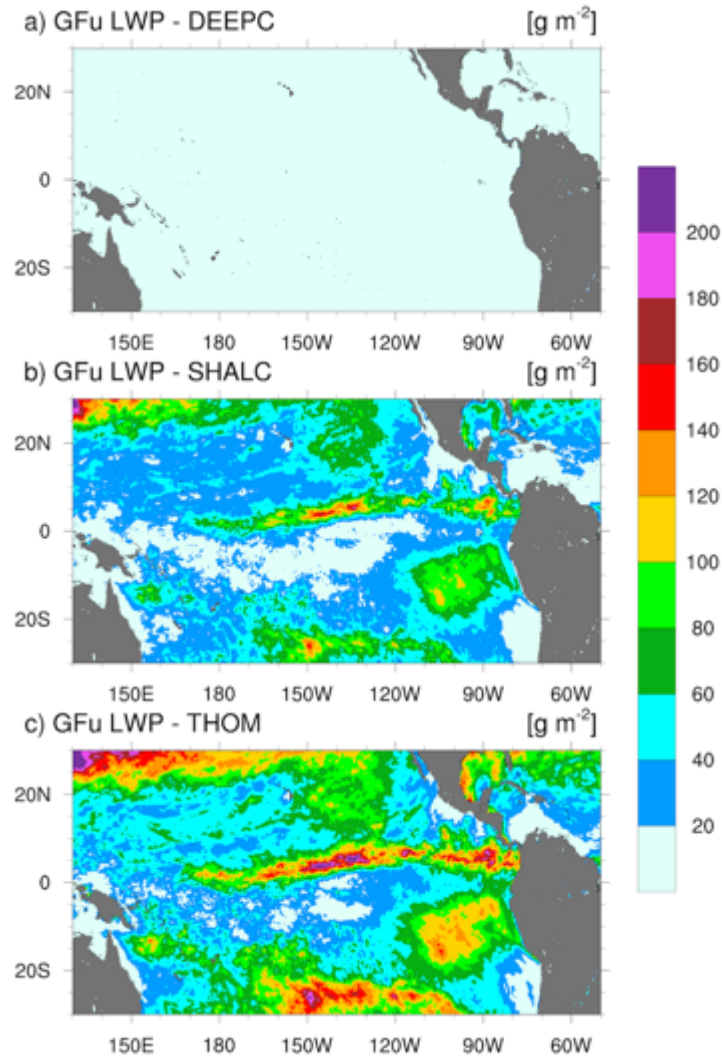


**Figure 15:** Monthly-mean of cloud liquid water path of corresponding to a) deep convection only (DEEPC); b) shallow convection only (SHALC); and c) no convection (THOM) simulated with GFu over the Tropical Pacific Ocean for December 2015.

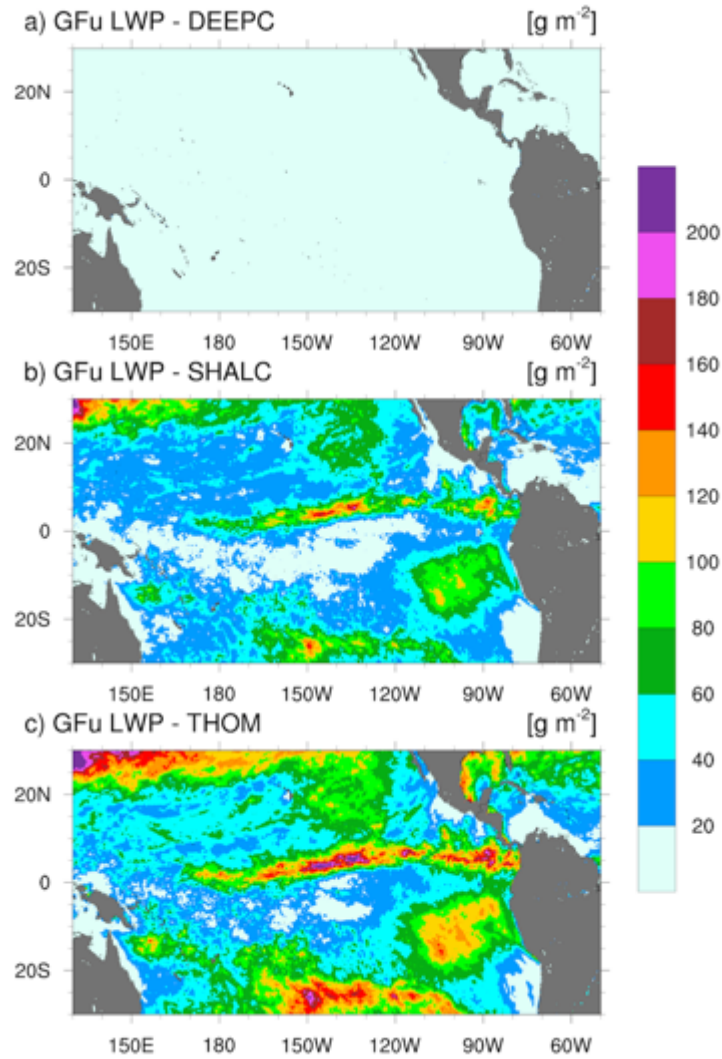


**Figure 15:** Monthly-mean of cloud liquid water path of corresponding to a) deep convection only (DEEPC); b) shallow convection only (SHALC); and c) no convection (THOM) simulated with GFu over the Tropical Pacific Ocean for December 2015.

**Page 31: [8] Deleted** **Laura Fowler** **3/6/20 10:45:00 AM**  
and shallow

**Page 31: [8] Deleted** **Laura Fowler** **3/6/20 10:45:00 AM**  
and shallow

**Page 31: [8] Deleted** **Laura Fowler** **3/6/20 10:45:00 AM**  
and shallow

**Page 31: [8] Deleted** **Laura Fowler** **3/6/20 10:45:00 AM**  
and shallow

**Page 31: [8] Deleted** **Laura Fowler** **3/6/20 10:45:00 AM**  
and shallow

**Page 31: [9] Deleted** **Laura Fowler** **3/6/20 10:45:00 AM**



Precipitation

<b>Page 31: [9] Deleted</b>	<b>Laura Fowler</b>	<b>3/6/20 10:45:00 AM</b>
-----------------------------	---------------------	---------------------------

Precipitation

<b>Page 31: [9] Deleted</b>	<b>Laura Fowler</b>	<b>3/6/20 10:45:00 AM</b>
-----------------------------	---------------------	---------------------------

Precipitation

<b>Page 31: [9] Deleted</b>	<b>Laura Fowler</b>	<b>3/6/20 10:45:00 AM</b>
-----------------------------	---------------------	---------------------------

Precipitation

<b>Page 31: [9] Deleted</b>	<b>Laura Fowler</b>	<b>3/6/20 10:45:00 AM</b>
-----------------------------	---------------------	---------------------------

Precipitation

<b>Page 31: [9] Deleted</b>	<b>Laura Fowler</b>	<b>3/6/20 10:45:00 AM</b>
-----------------------------	---------------------	---------------------------

Precipitation

<b>Page 31: [9] Deleted</b>	<b>Laura Fowler</b>	<b>3/6/20 10:45:00 AM</b>
-----------------------------	---------------------	---------------------------

Precipitation

<b>Page 31: [9] Deleted</b>	<b>Laura Fowler</b>	<b>3/6/20 10:45:00 AM</b>
-----------------------------	---------------------	---------------------------

Precipitation

<b>Page 31: [9] Deleted</b>	<b>Laura Fowler</b>	<b>3/6/20 10:45:00 AM</b>
-----------------------------	---------------------	---------------------------

Precipitation

<b>Page 31: [9] Deleted</b>	<b>Laura Fowler</b>	<b>3/6/20 10:45:00 AM</b>
-----------------------------	---------------------	---------------------------

Precipitation

<b>Page 31: [9] Deleted</b>	<b>Laura Fowler</b>	<b>3/6/20 10:45:00 AM</b>
-----------------------------	---------------------	---------------------------

Precipitation

<b>Page 31: [9] Deleted</b>	<b>Laura Fowler</b>	<b>3/6/20 10:45:00 AM</b>
-----------------------------	---------------------	---------------------------

Precipitation

<b>Page 31: [9] Deleted</b>	<b>Laura Fowler</b>	<b>3/6/20 10:45:00 AM</b>
-----------------------------	---------------------	---------------------------

Precipitation

<b>Page 31: [9] Deleted</b>	<b>Laura Fowler</b>	<b>3/6/20 10:45:00 AM</b>
-----------------------------	---------------------	---------------------------

Precipitation

<b>Page 31: [9] Deleted</b>	<b>Laura Fowler</b>	<b>3/6/20 10:45:00 AM</b>
-----------------------------	---------------------	---------------------------

Precipitation

<b>Page 31: [9] Deleted</b>	<b>Laura Fowler</b>	<b>3/6/20 10:45:00 AM</b>
-----------------------------	---------------------	---------------------------

Precipitation

<b>Page 31: [9] Deleted</b>	<b>Laura Fowler</b>	<b>3/6/20 10:45:00 AM</b>
-----------------------------	---------------------	---------------------------

Precipitation

**Page 31: [9] Deleted** Laura Fowler 3/6/20 10:45:00 AM

Precipitation

**Page 31: [9] Deleted** Laura Fowler 3/6/20 10:45:00 AM

Precipitation

**Page 31: [10] Deleted** Laura Fowler 3/6/20 10:45:00 AM

convection

**Page 31: [10] Deleted** Laura Fowler 3/6/20 10:45:00 AM

convection

**Page 31: [10] Deleted** Laura Fowler 3/6/20 10:45:00 AM

convection

**Page 31: [10] Deleted** Laura Fowler 3/6/20 10:45:00 AM

convection

**Page 31: [10] Deleted** Laura Fowler 3/6/20 10:45:00 AM

convection

**Page 31: [10] Deleted** Laura Fowler 3/6/20 10:45:00 AM

convection

**Page 31: [10] Deleted** Laura Fowler 3/6/20 10:45:00 AM

convection

**Page 31: [10] Deleted** Laura Fowler 3/6/20 10:45:00 AM

convection

**Page 31: [10] Deleted** Laura Fowler 3/6/20 10:45:00 AM

convection

**Page 31: [10] Deleted** Laura Fowler 3/6/20 10:45:00 AM

convection

**Page 31: [10] Deleted** Laura Fowler 3/6/20 10:45:00 AM

convection

**Page 31: [10] Deleted** Laura Fowler 3/6/20 10:45:00 AM

convection

**Page 31: [10] Deleted** Laura Fowler 3/6/20 10:45:00 AM

convection

**Page 31: [10] Deleted** Laura Fowler 3/6/20 10:45:00 AM

convection

<b>Page 31: [10] Deleted</b>	<b>Laura Fowler</b>	<b>3/6/20 10:45:00 AM</b>
------------------------------	---------------------	---------------------------

convection

<b>Page 31: [10] Deleted</b>	<b>Laura Fowler</b>	<b>3/6/20 10:45:00 AM</b>
------------------------------	---------------------	---------------------------

convection

<b>Page 31: [10] Deleted</b>	<b>Laura Fowler</b>	<b>3/6/20 10:45:00 AM</b>
------------------------------	---------------------	---------------------------

convection

<b>Page 31: [10] Deleted</b>	<b>Laura Fowler</b>	<b>3/6/20 10:45:00 AM</b>
------------------------------	---------------------	---------------------------

convection

<b>Page 31: [10] Deleted</b>	<b>Laura Fowler</b>	<b>3/6/20 10:45:00 AM</b>
------------------------------	---------------------	---------------------------

convection

<b>Page 31: [10] Deleted</b>	<b>Laura Fowler</b>	<b>3/6/20 10:45:00 AM</b>
------------------------------	---------------------	---------------------------

convection

<b>Page 31: [10] Deleted</b>	<b>Laura Fowler</b>	<b>3/6/20 10:45:00 AM</b>
------------------------------	---------------------	---------------------------

convection